AN INTRODUCTION TO THE INTERIM DIGITAL SAR PROCESSOR AND THE CHARACTERISTICS OF THE ASSOCIATED SEASAT SAR IMAGERY

JET PROPULSION LAB.
PASADENA, CA

01 APR 1981

JPL PUBLICATION 81-26

An Introduction to the Interim Digital SAR Processor and the Characteristics of the Associated SEASAT SAR Imagery

C. Wu
B. Barkan
B. Huneycutt
C. Leang
S. Pang

April 1, 1981

National Aeronautics and
Space Administration

Jet Propulsion Laboratory
California Institute of Technology
Pasadena, California

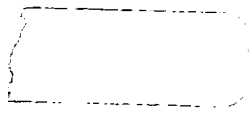

The research described in this publication was carried out by the Jet Propulsion Laboratory, California Institute of Technology, under contract with the National Aeronautics and Space Administration.

TECHNICAL REPORT STANDARD TITLE PAGE

1. Report No. JPL Pub. 81-26	2. Government Accession No.	3. Recipient's Catalog No.
4. Title and Subtitle An Introduction to the Interim Digital SAR Processor and the Characteristics of the Associated SEASAT SAR Imagery		5. Report Date April 1, 1981 6. Performing Organization Code
7. Author(s) C. Wu, B. Barkan, B. Huneycutt, C. Leang, S. Pang		8. Performing Organization Report No.
9. Performing Organization Name and Address JET PROPULSION LABORATORY California Institute of Technology 4800 Oak Grove Drive Pasadena, California 91103		10. Work Unit No. 11. Contract or Grant No. NAS 7-100 13. Type of Report and Period Covered JPL Publication
12. Sponsoring Agency Name and Address NATIONAL AERONAUTICS AND SPACE ADMINISTRATION Washington, D.C. 20546		14. Sponsoring Agency Code RD151-J-656-62-01-01-00

15. Supplementary Notes

16. Abstract

An Interim Digital SAR Processor (IDP) was developed in 1979 to produce a limited amount of digital SEASAT SAR (Synthetic Aperture Radar) data to assist utility studies in microwave remote sensing of earth resources and environment. The purpose of this report is to provide basic engineering data regarding the Interim Digital SAR Processor and the associated digitally correlated SEASAT SAR Imagery. Materials covered in this report include: 1) SEASAT SAR processing functions, 2) An introduction to the Interim Digital SAR Processor, 3) IDP performance summary, and 4) Characteristics of SEASAT SAR imagery. The first three subjects describe the correlation function, IDP hardware/software configuration, and a preliminary performance assessment. The last subject treats both the geometric and radiometric characteristics of SAR imagery with emphasis on those that are peculiar to the IDP produced SEASAT SAR imagery.

17. Key Words (Selected by Author(s))	18. Distribution Statement
Electronics and Electrical Engineering Geosciences and Oceanography (General) Earth Resources Computer Programming and Software	Unclassified - Unlimited

19. Security Classif. (of this report)	20. Security Classif. (of this page)	21. No. of Pages	22. Price
Unclassified	Unclassified		

ACKNOWLEDGEMENT

The authors wish to thank R. G. Piereson for his thoughtful planning of this development, J. C. Gilstrap for the design and implementation of the digital tape-recorded computer interface, Dr. A. R. Johnston for the fiber-optic data link, and Dr. A. E. Di Cenzo and Dr. D. N. Held for discussions and their suggestion of an autofocus approach.

ABSTRACT

An Interim Digital SAR Processor (IDP) was developed in 1979 to produce a limited amount of digital SEASAT SAR (Synthetic Aperture Radar) data to assist utility studies in microwave remote sensing of earth resources and environment. The purpose of this report is to provide basic engineering data regarding the Interim Digital SAR Processor and the associated digitally correlated SEASAT SAR Imagery. Materials covered in this report include: 1) SEASAT SAR processing functions, 2) An introduction to the Interim Digital SAR Processor, 3) IDP performance summary, and 4) Characteristics of SEASAT SAR imagery. The first three subjects describe the correlation function, IDP hardware/software configuration, and a preliminary performance assessment. The last subject treats both the geometric and radiometric characteristics of SAR imagery with emphasis on those that are peculiar to the IDP produced SEASAT SAR imagery.

TABLE OF CONTENTS

FIGURES

FIGURES (cont'd)

TABLES

1. INTRODUCTION

The launch of the SEASAT satellite in June 1978 marked the advance of SAR (Synthetic Aperture Radar) remote sensing technology from a conventional airborne environment into an earth orbiting spaceborne environment. A spaceborne SAR can provide wider width and much faster coverage capability than can be provided by an airborne SAR. Thus a spaceborne SAR offers a great potential for an operational global environmental monitoring system. During the 105 days of SEASAT operation, approximately 50 hours of SAR data were collected. The task of data reduction and utilization for SAR technology assessment remains an ongoing challenge.

While the bulk of the SEASAT SAR imagery was produced by an optical correlator, an Interim Digital SAR Processor (IDP) was developed to produce a limited amount of digital SEASAT SAR imagery. The detailed design and implementation phase began in April 1978. By March 1980, more than 150 SEASAT SAR frames had been digitally correlated and delivered to various users. Current performance of the IDP meets the original design goals regarding its image resolution capability and throughput rate. We are also conducting an IDP Upgrade Task to enhance the IDP throughput rate and image quality performance.

The purpose of this report is to provide basic technical information regarding the IDP correlated SEASAT SAR imagery. Areas covered in this report include: 1) SEASAT SAR processing functions, 2) An introduction to the Interim Digital SAR processor, 3) IDP performance summary, and 4) Characteristics of SEASAT SAR imagery.

2. SEASAT SAR PROCESSING FUNCTIONS

2.1 Introduction to the SAR Sensor Characteristics

A summary of the SEASAT SAR system parameters and the performance requirements is given in Table 1 and reference [1]. Figure 1 illustrates a SEASAT orbit track (Revolution Number 1291) and the associated SAR imaging swath (represented by the shaded area). Positions of SEASAT ground receiving stations and their coverage are also plotted on the figure. Figure 2 shows the SEASAT satellite configuration. One of the most prominent features is the 2m x 10m SAR antenna which is mounted on the spacecraft with its boresight oriented at a 20° angle from vertical direction. The received radar echoes were telemetered to the STDN ground receiver station over an analog data link. This signal was digitized and recorded on a 120 M bits/s High Data Rate Recorder (HDRR). The radar antenna was pointed to the right of the flight plath. The SAR viewing geometry is illustrated in Figure 3. The antenna beam measured approximately 6 degrees in elevation and 1 degree in azimuth. The radar footprint on the Earth's surface (within the 3 dB beam contour) measured approximately 100 km by 15 km.

A SAR normally utilizes an antenna pointing direction normal to the flight path. Radar imaging in the cross-track (range) direction is accomplished from the target echo delay, which is proportional to the distance from the sensor to the target. Range resolution, which corresponds to the pulse width of a point target response, is inversely proportional to the bandwidth of the radar transmitted pulses. Radar scanning in the along-track (azimuth) direction is accomplished by the satellite motion. The radar antenna beamwidth in azimuth results in a footprint which is much wider than the range resolution

Table 1. SEASAT SAR Sensor Characteristics and the Interim Digital SAR Processor Performance Requirements

SAR System Parameters (SEASAT-A SAR)	
SAR Orbit	Polar (108° inclination)
Nominal Altitude	794 km
Nominal Speed	7450 m/sec
Transmitter Frequency	1275 MHz
Pulse Repetition Frequency	1463, 1537, 1645 Hz
Pulse Duration	33.8 μsec
Pulse Bandwidth	19 MHz
A/D Sampling Rate	45.53 MHz
(Range Offset Signal)	
A/D Sampling Window Duration	288 μsec
Antenna Dimensions	2 m x 10.5 m
Antenna Look Angle	20° elevation, 90° azimuth
Attitude (roll, pitch, yaw) Accuracy	$\pm$ 0.5°
Interim Digital Processor Performance Requirements	
Image Frame Size	100 km x 100 km
Image Resolution	25 m
Number of Looks	4
Data Processing Speed	$\leq$ 12 hours/frame

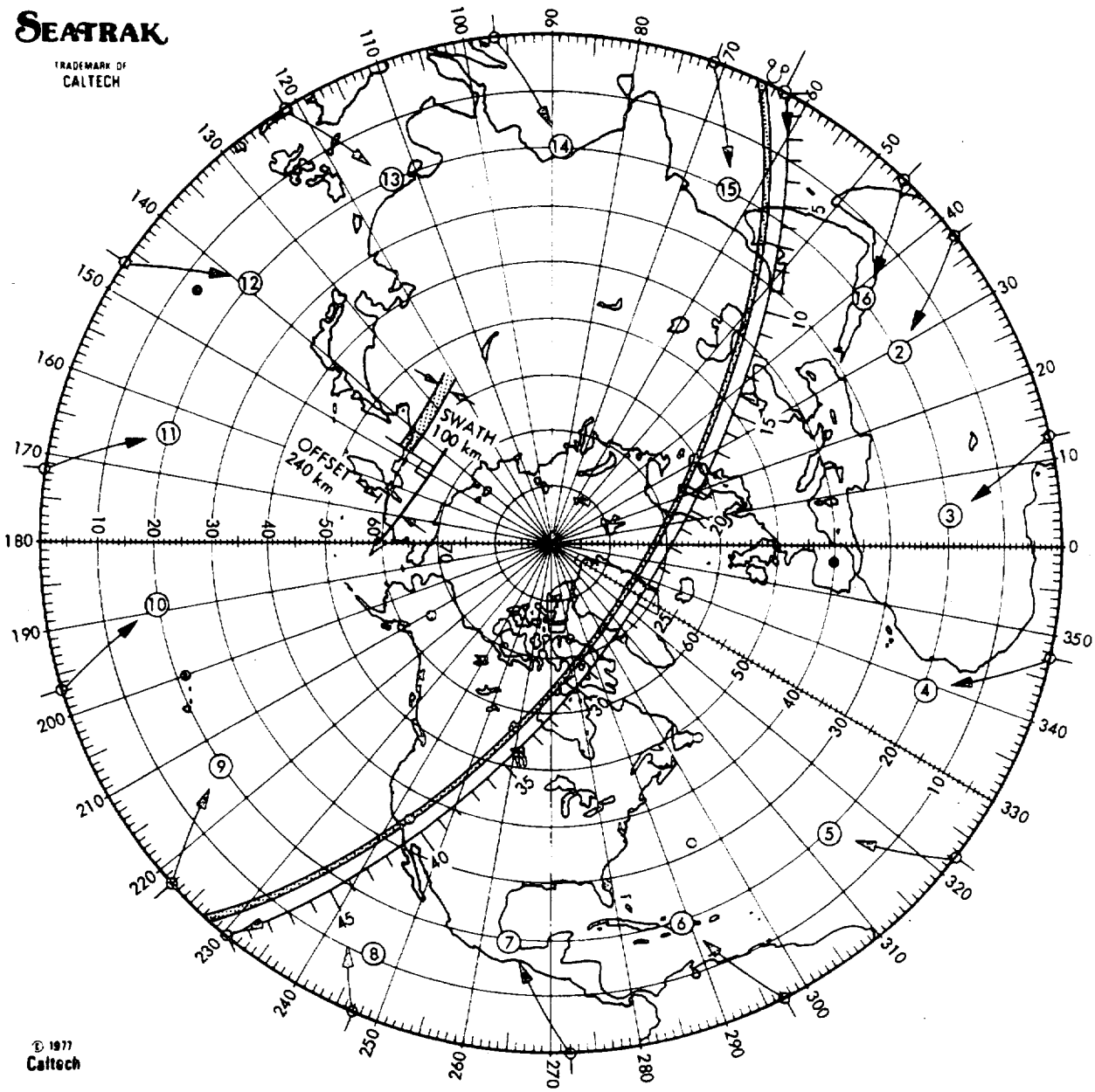

Figure 1. A SEASAT SAR Ground Track (Rev. 1291) in the Northern Hemisphere and SEASAT SAR Ground Receiving Stations

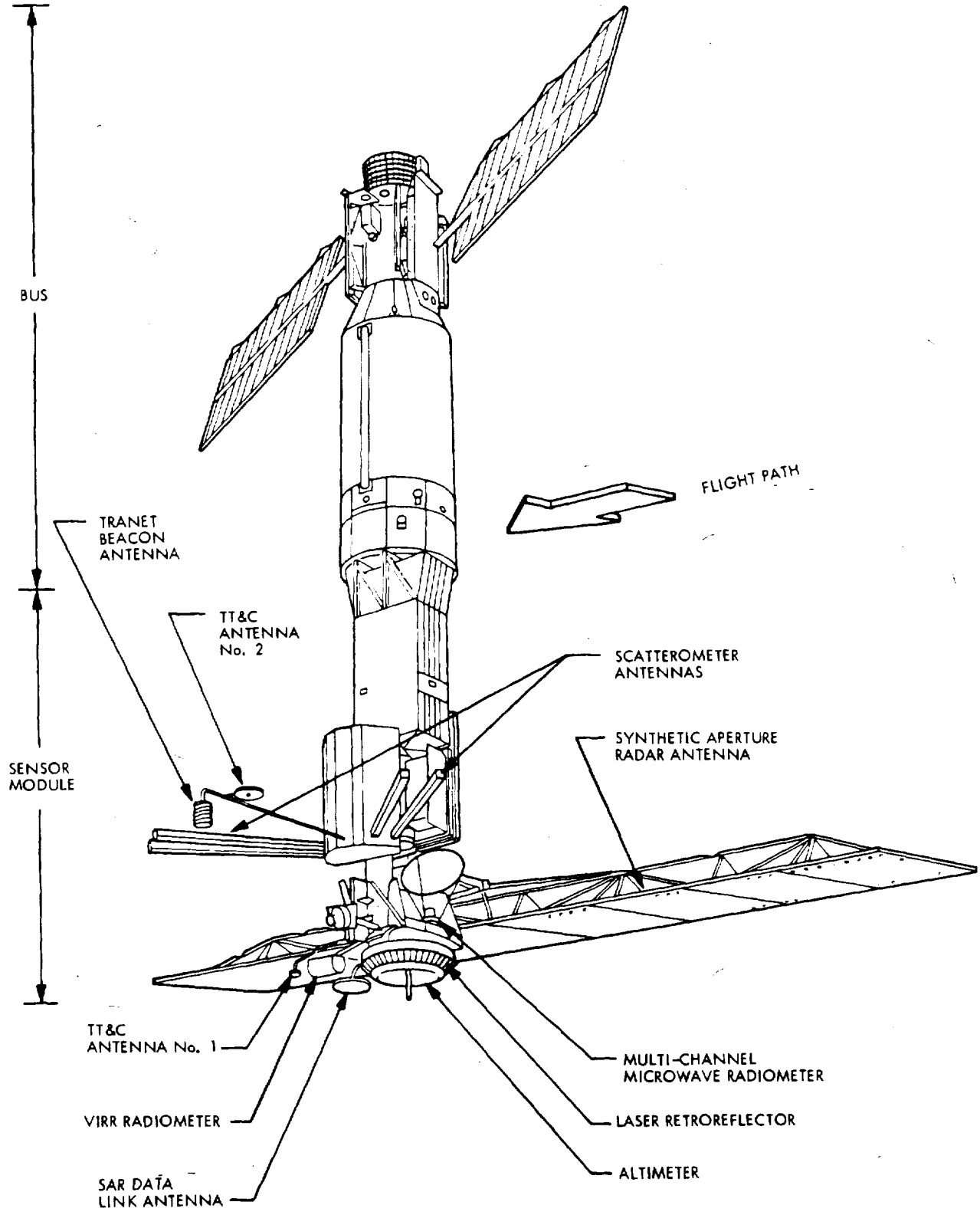

Figure 2. SEASAT On-Orbit Configuration

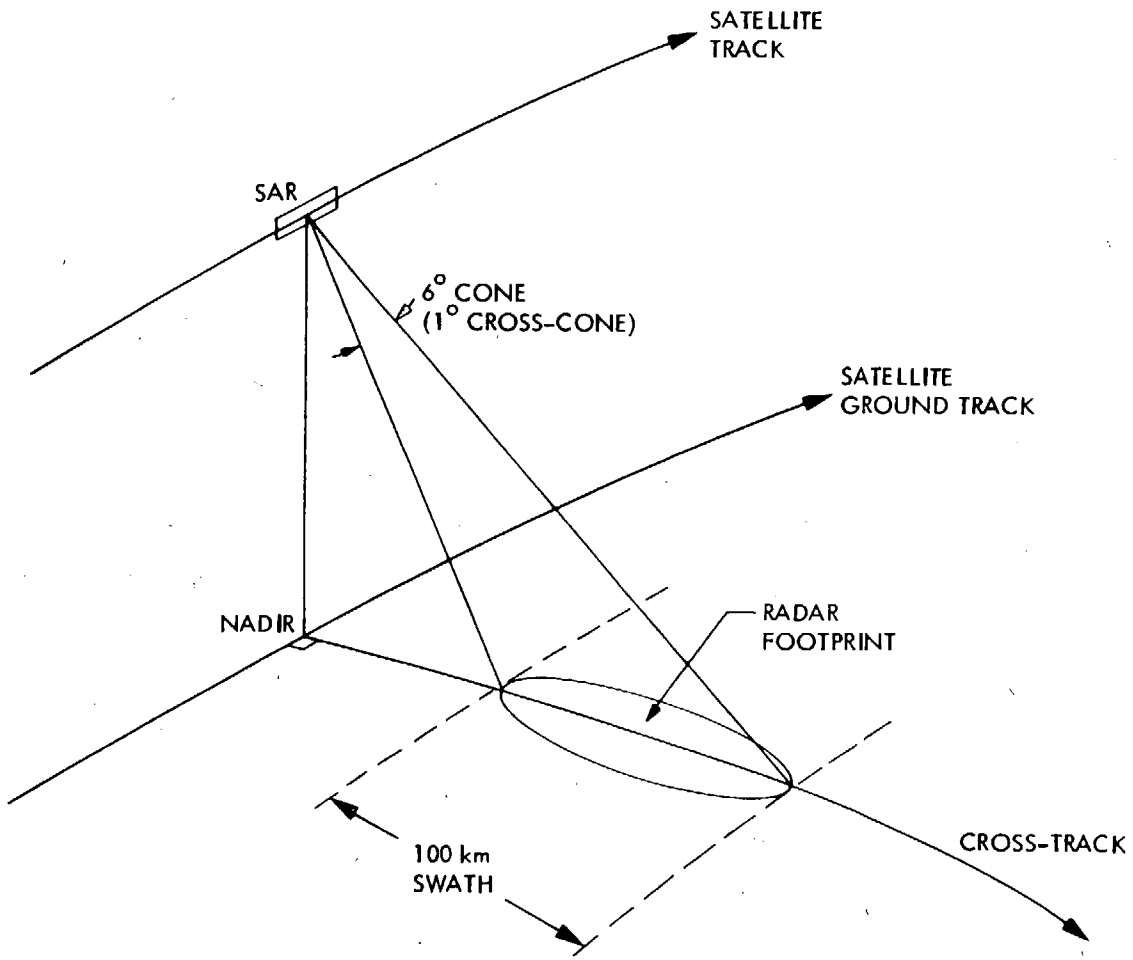

Figure 3. SEASAT SAR Imaging Geometry

element. To achieve a comparable imaging resolution in azimuth, a correlation process must be performed on the radar echo data to form a large synthetic aperture along track, which produces a much narrower effective beamwidth. Tutorial explanations on the SAR principles are given in References [2-4].

2.2 SEASAT-A Processing Functions

The major SEASAT-A SAR processing steps to produce high resolution imagery include 1) Range pulse compression, 2) Doppler parameter estimation, 3) Azimuth correlation, and 4) Multiple-look overlay. These functions must incorporate several SEASAT SAR unique procedures to accommodate peculiarities in the SEASAT SAR data (see para. 2.2.5).

2.2.1 Range Correlation

The purpose of the range correlation is to compress the time dispersed (33.8 μsec) radar transmitted pulse into an impulse. The 19 MHz bandwidth of the transmitter pulse encoding enables a 6.6 meter resolution in the slant range direction. This corresponds to approximately 17 meters to 23 meters range resolution on the Earth's surface. The variation on the ground range resolution is due to the different radar incidence angles over the swath.

2.2.2 Doppler Parameter Estimation

Synthetic aperture correlation is critically dependent on obtaining an accurate estimate of the target phase delay history during the period of time that a target is illuminated by the radar. The phase delay history of a target can be accurately represented by a quadratic function with the instantaneous Doppler frequency and Doppler frequency rate at the center of the antenna illumination being two sufficient parameters to characterize this phase

history. Once these two parameters are obtained, a correlation reference function can be derived. Therefore, the objective of the Doppler parameter estimation function is to obtain accurate estimates of these two parameters.

2.2.3 Azimuth Correlation

The azimuth correlation operation is performed to obtain a very narrow effective radar beamwidth in the azimuth dimension. To perform this operation, the range correlated data lines are first accumulated to facilitate data access in the azimuth direction. The result of azimuth correlation consists of four independently correlated single-look images exhibiting approximately 25m resolution in azimuth.

2.2.4 Multiple-Look Overlay

The multiple-look overlay function must accomplish accurate registration and incoherent averaging of the intensity measures of the four single-look images. The resultant intensity pixel values go through a square-root operation and are linearly encoded into 8-bit data words.

2.2.5 SEASAT SAR Processing Peculiarities

SEASAT SAR processing differs from typical aircraft SAR processing in many ways. Besides the unusually large pulse compression factors, three major peculiarities are the severe range migration effect, the degree of uncertainty in the SAR attitude, and the continuing change of target echo response function during each data collection pass.

In SEASAT SAR data the range delay history of a point target traverses many range resolution elements as the target passes through the radar antenna beam. The migration history can be treated as a sum of two components: One is directly proportional to the elapsed time or distance along the radar flight path and is usually referred to as range walk. The other is proportional to the square of the elapsed time and is called the range curvature component. The parameters for these two components are generally referred to as the Doppler frequency and frequency rate, respectively. For SEASAT SAR, the range curvature part of the delay history traverses approximately 8 range samples from center to either edge of the radar beam. This implies that the SEASAT azimuth correlation must be a two dimensional process. The computational complexity is greatly increased by this amount of range curvature.

The uncertainty in radar attitude corresponds to residual error in the attitude control angles. This error is approximately 0.5 degree in pitch and yaw which is large compared to the 1 degree azimuth beamwidth. To achieve a good signal to noise ratio in a SAR image, substantial data preprocessing is needed to derive an accurate estimate of the instantaneous Doppler frequency at the center of the beam. These estimates need to be periodically updated to account for doppler variations.

The variation of the radar response parameters as a function of the sensor orbit position is due to the fact that the surface speed due to earth rotation changes with latitude. This results in a change of the sensor-target relative speed and the associated Doppler frequency response. A plot of the center-of-beam Doppler frequency and frequency rate as a function of the orbit anomaly

angle is shown in Figure 4. The SEASAT SAR processing parameters need to be periodically updated to account for these parameter variations.

The data in Figure 4 also contain information regarding the magnitude and bound of the range delay history. The functional relationship is given by

$$R(\Delta t) = \frac{\lambda}{2}\left(f\Delta t + \frac{1}{2}\dot{f}\Delta t^2\right), \quad |\Delta t| \leq 1.25 \text{ sec} \tag{1}$$

where $R(\Delta t)$ refers to the range delay relative to its center-of-beam value ($R(\Delta t = 0)$), λ is the radar wavelength, f is the center-of-beam Doppler frequency, and $\dot{f}$ is the Doppler frequency rate. The synthetic aperture integration time is approximately 2.5 seconds over the full aperture width. For a value of f near 3,000 Hz, the total range migration can be 128 range samples over the full aperture width. It follows directly from Eq. 1 that the synthetic aperture phase history for the IDP azimuth correlation is defined by Eq. 2:

$$\phi(\Delta t) = 2\pi\left(f\Delta t + \frac{1}{2}\dot{f}\Delta t^2\right), \quad |\Delta t| \leq 1.25 \text{ sec} \tag{2}$$

These equations show that accurate measures of f and $\dot{f}$ are sufficient to control range migration compensation and to generate the azimuth reference functions within the SAR processor.

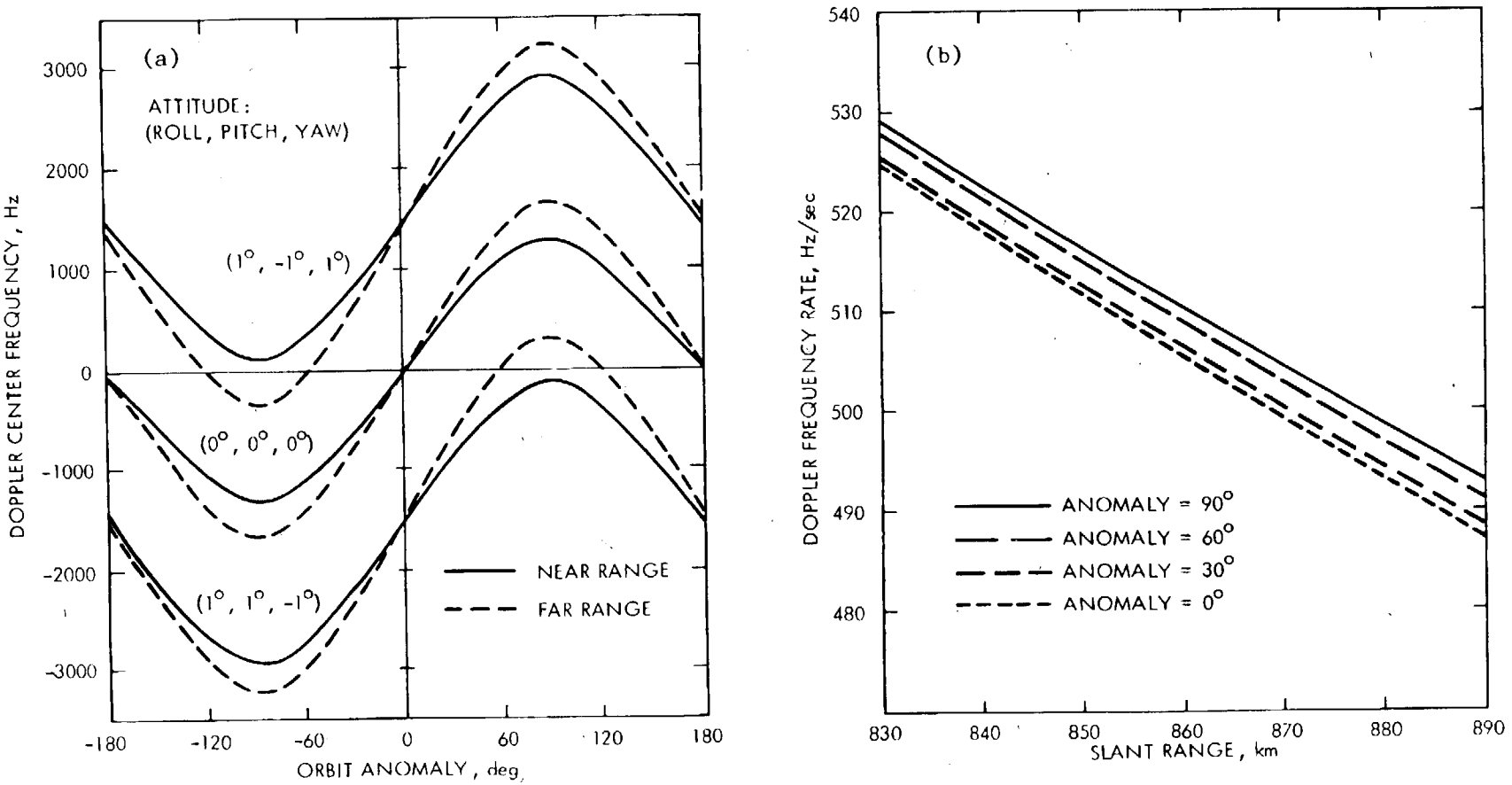

Figure 4. SEASAT SAR Doppler Characteristics
(a) Doppler Center Frequency vs. Orbit Angle
(b) Doppler Frequency Rate vs. Slant Range

3. CHARACTERISTICS OF THE INTERIM DIGITAL SAR PROCESSOR (IDP)

The Interim Digital SAR Processor (IDP) is a software based SAR processor developed to produce digital SEASAT SAR imagery to support SAR application studies. The throughput of the system is moderate, approximately one SEASAT SAR frame (100 km x 100 km coverage, 25 m resolution, 4 looks) per ten hours of processing time. The hardware component of the system is a general purpose mini-computer based data processing facility. The software package was developed specifically for the IDP. A frequency domain fast correlation algorithm was implemented to perform the SAR range and azimuth correlation functions.

3.1 Hardware Structure

A block diagram of the IDP facility is shown in Figure 5. The hardware consists of the following elements.

3.1.1 Fiber-Optics Data Link

This fiber-optics data link provides the data transmission path between the SEASAT-A HDDR (High Density Digital Recorder) and the IDP facility which is located in a separate building at JPL.

3.1.2 HDDR Data Interface

This interface hardware receives the bit-serial data stream from the HDDR (through the optical data link), decodes the timing and interframe signals, buffers each frame (one echo pulse), truncates the least significant bit of each 5-bit data sample, and packs the resultant 4-bit data samples into 32-bit words suitable for storage on the computer disk memory.

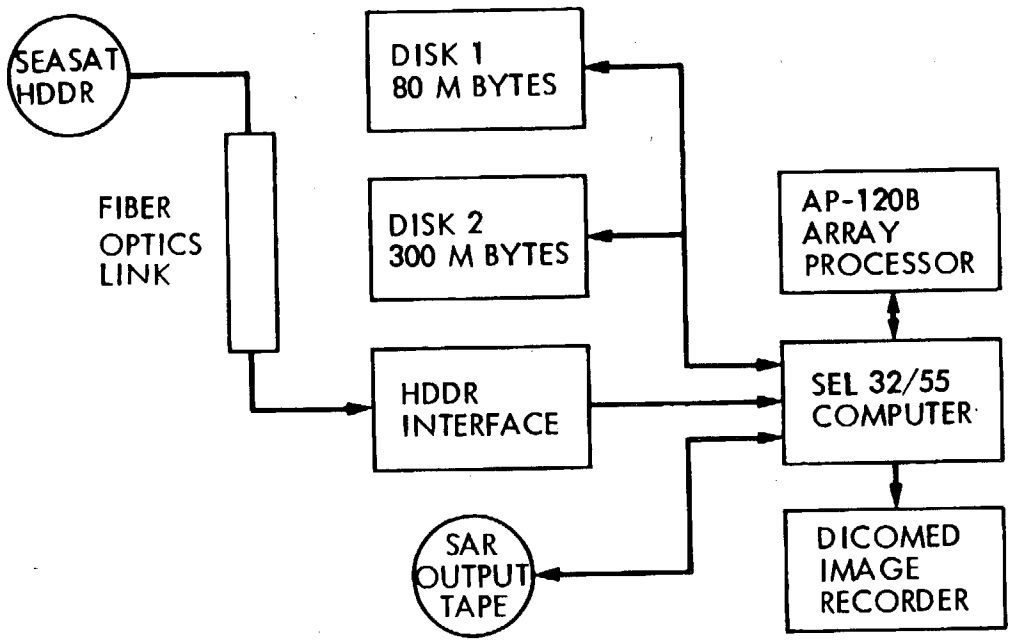

Figure 5. Interim Digital SAR Processor (IDP) Facility Block Diagram

3.1.3 SEL 32/55 Computer

This computer is a 32 bit minicomputer equipped with 96 thousand words of core memory. It performs system level control functions for the software execution and also performs a variety of data handling tasks.

3.1.4 AP-120B Floating-Point Array Processor

This array processor is equipped with parallel pipeline arithmetic adder and multiplier and 16K words of high speed data memory. Its main function is to perform vector arithmetic computations.

3.1.5 Disk Storage Devices

Two disk drives are involved. One has a storage capacity of 80 M bytes, which is used for program storage and scratch-pad storage. The other disk has a storage capacity of 300 M bytes. This disk is used for raw data storage (220 M bytes space) and storage of intermediate computational results.

3.1.6 Other Computer Peripherals

Other IDP computer elements include a Dichomed image recorder and typical peripheral devices such as tape drives, line printer, and CRT control terminals.

3.2 IDP Software Modules

A frequency domain fast correlation algorithm was implemented in the IDP to reduce SESAT SAR data into imagery. The basic processing algorithm concept was originally reported in [5], which is also attached in Appendix A. An updated algorithm description was reported in [6]. Major software modules and their functional relationship are shown in a block diagram in Figure 6.

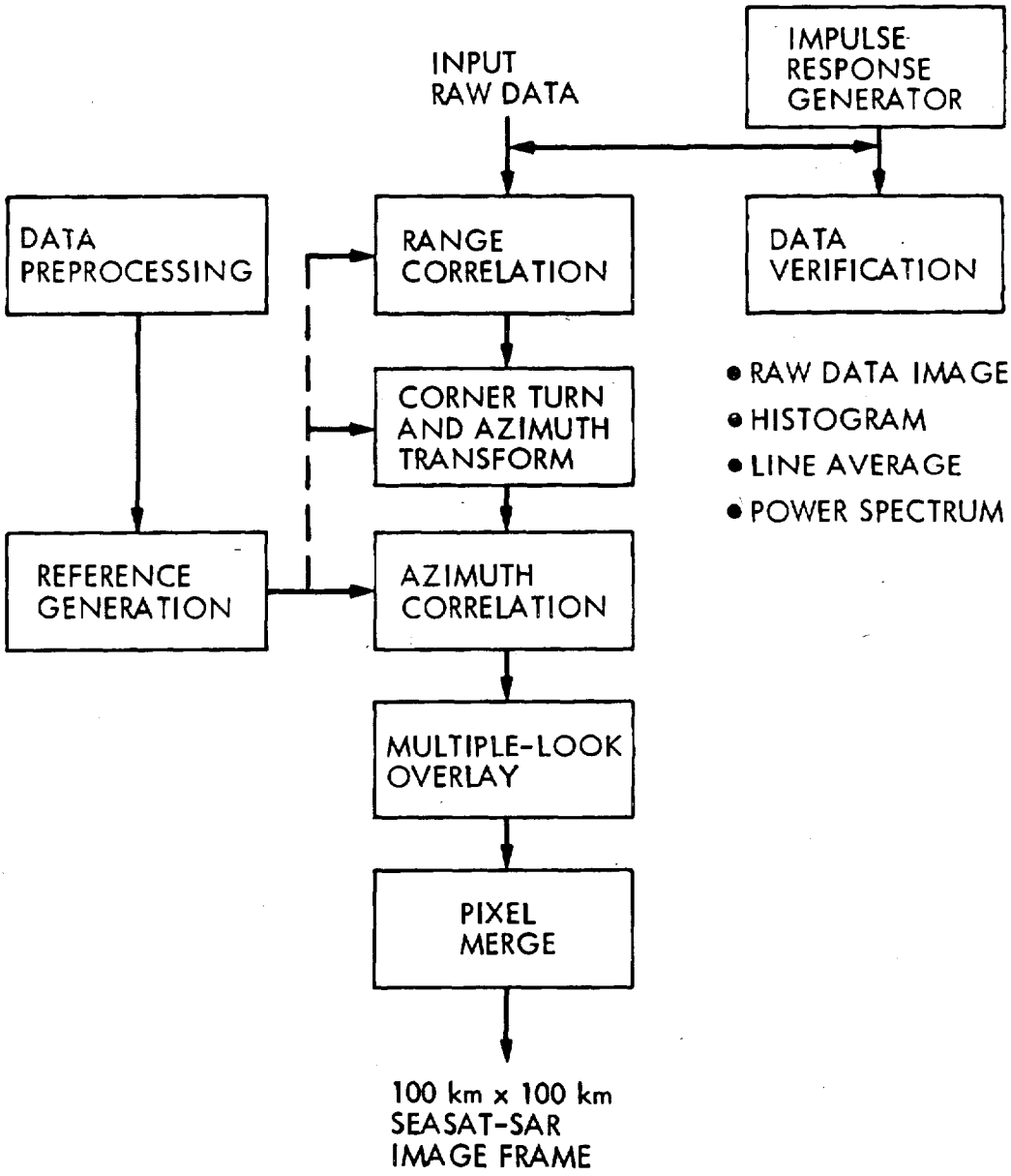

Figure 6. Interim Digital SAR Processor (IDP) Software Block Diagram

A brief summary of the function of each program module is provided in the following subsections.

3.2.1 SAR Raw Data Input Program

This program accepts the packed 4 bit raw data samples and loads them onto the 300M byte storage disk. A photographic representation of a typical raw data set is shown in Figure 7.

3.2.2 Point Target Response Simulation Program

This program simulates the point target echo response of the SEASAT-A SAR sensor. The program was used to test and verify the SAR fast correlation programs. A synthesis of a typical SEASAT SAR point-target response is shown in Figure 8.

3.2.3 Data Test and Verification Program

This program comprises a number of subprograms which include the data/image display program, the histogram program, the power spectrum program, the data averaging program, etc. This program is used to verify the data quality at each stage of SAR correlation processing.

3.2.4 Data Preprocessing Program

This preprocessing program is used to estimate the key parameters for the azimuth correlation of the SEASAT-A SAR data. Parameters to be estimated are the instantaneous Doppler frequency and Doppler frequency rate of targets near the center of the antenna illumination. Estimation of Doppler center frequency can be made on the radar raw data by first obtaining the power spectrum

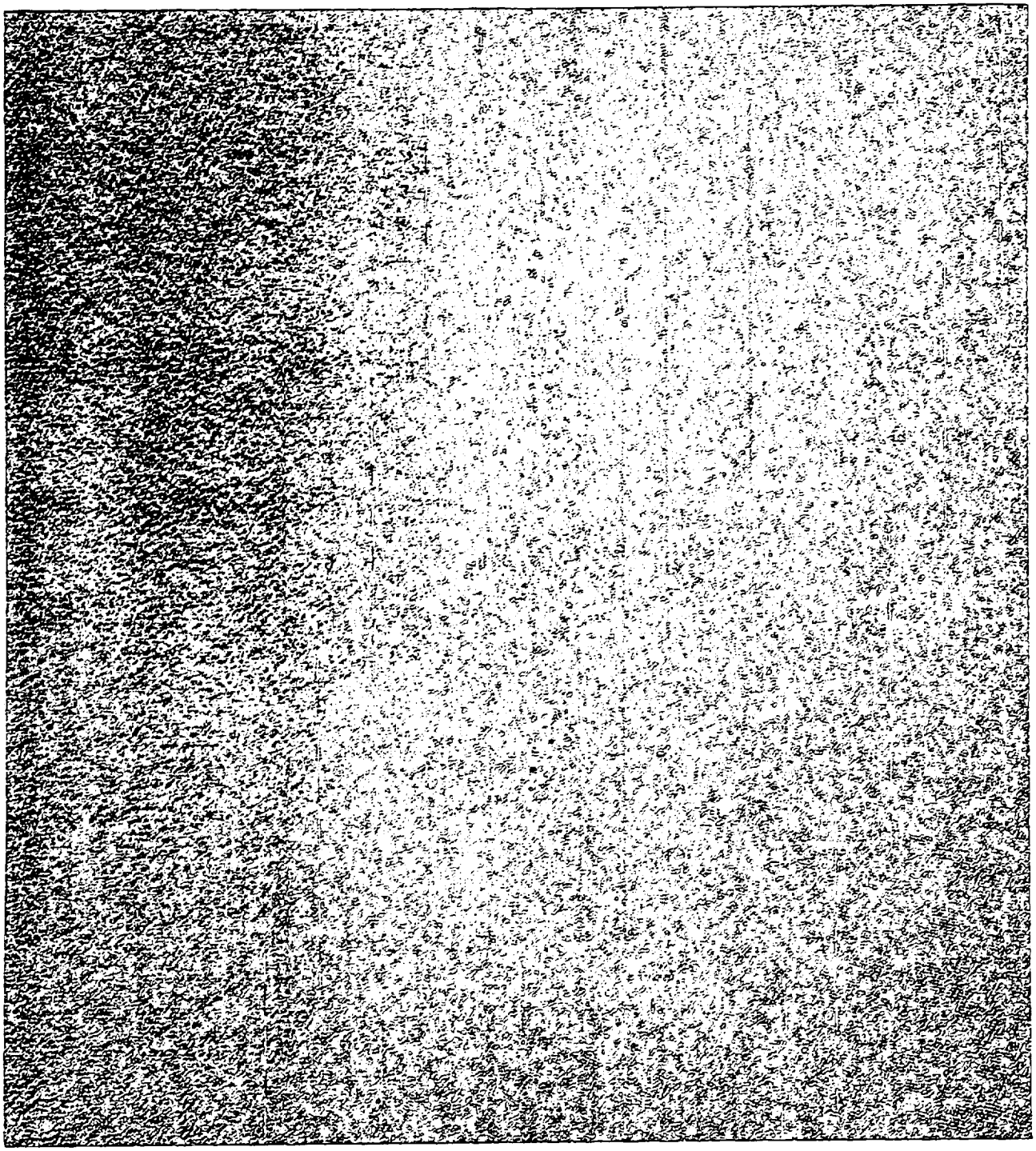

Figure 7. Display of a Section (2048 x 2048 Samples) of SEASAT SAR Raw Data

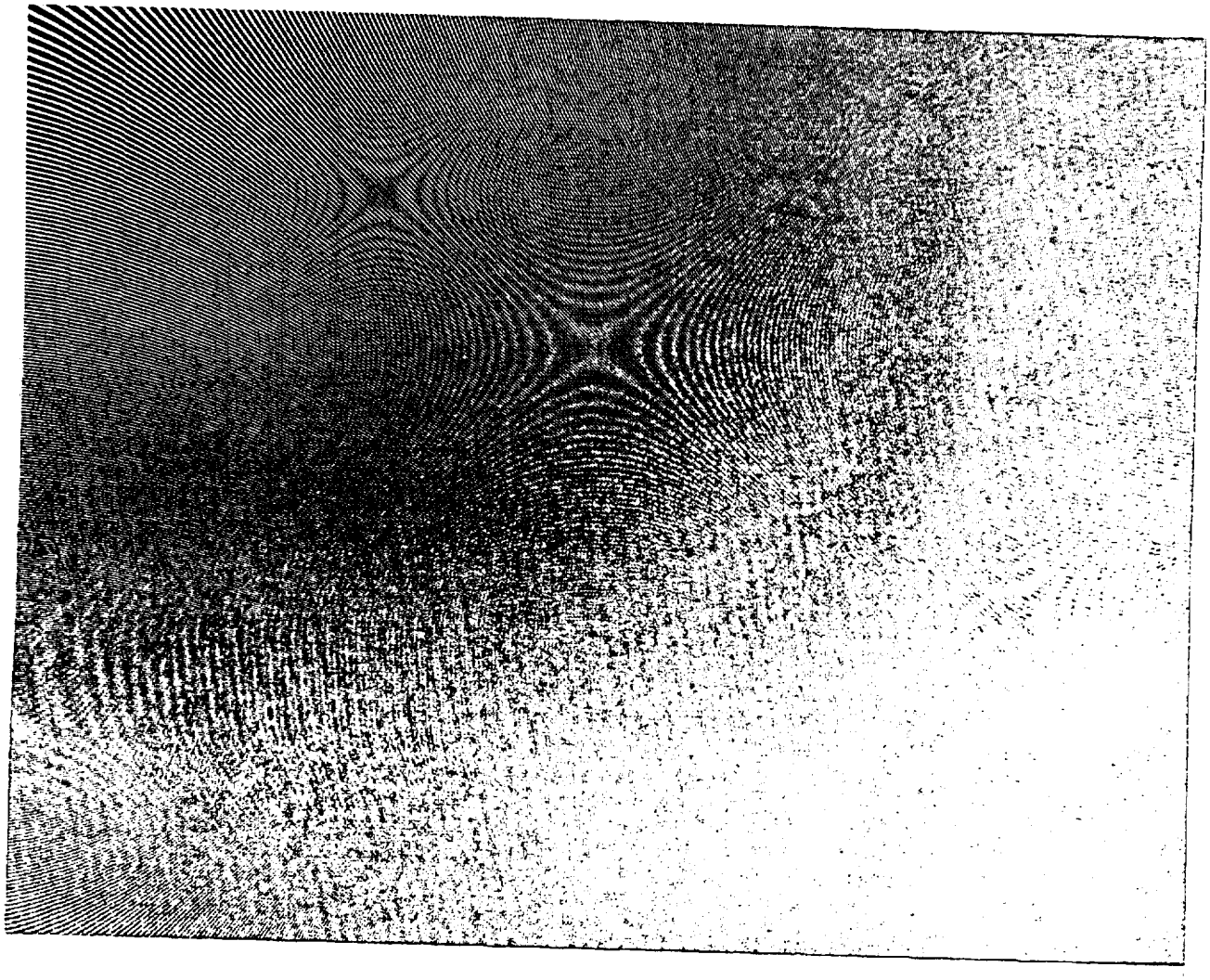

Figure 8. A Simulated SEASAT SAR Point Target Response Pattern (2048 x 2048 Samples, Approximately One-Half of SEASAT SAR Response)

along the azimuth dimension. A more accurate method is used here which analyzes the intensity of corresponding pixels over the four azimuth looks. An error in the Doppler frequency rate affects the synthetic aperture focusing and therefore the registration accuracy of the four-look processing. The auto-focusing method adapted in the IDP to refine the Doppler frequency rate estimates is based on the auto-correlation of segments of one-look pictures and cross-correlation between the four single-look images of the same area.

3.2.5 Reference Function Generation Program

This program generates the reference functions for azimuth correlation, based on the estimated Doppler parameters provided from the data preprocessing program.

3.2.6 Range Correlation Program

This program performs the SEASAT-A SAR data range offset to I, Q (inphase and quadrature) conversion, the range correlation, preliminary range walk correction, and the first-stage corner-turn functions. The fast correlation is performed on a block of 4096 4-bit real raw data samples. Range offset to I, Q conversion is performed in the frequency domain by a translation of the offset spectrum to baseband. The range reference function has a length of 768-complex samples. The result of the correlation for each 4096 point input data block is 1280 complex data points. The real and imaginary parts of each complex word are truncated and packed into a 16-bit word, i.e. 8-bit for real and 8-bit for imaginary. During the course of range correlation the starting sample of the 4096 real data block is systematically adjusted to achieve first order range walk correction. The range reference function is also adjusted to provide a finer step size in the range walk correction. A total of four range

reference functions over a real range offset data bin are used to provide a range walk interpolation to 1/8 of the size of a complex range bin. The range correlated data are first stored in a 32-line buffer storage. They are regrouped into 40 each 32 x 32 point blocks and then output to the disk storage. This blocking facilitates the subsequent corner turn operation.

3.2.7. Corner Turn and Azimuth Forward Transform Program

This program calls selected blocks of data as described above, stores them in a buffer, and accesses the data in the azimuth dimension. This accomplishes the data corner turn operation. A Fourier transform then is performed on these azimuth data vectors. The resultant spectra, which are packed into 16 bits per complex word, are output to another disk storage file. The dimension of the data vector to perform the Fourier transform is 2048 complex samples in azimuth.

3.2.8 Azimuth Correlation Program

This program calls the azimuth spectral data, performs a range migration compensation in the azimuth spectral domain, multiplies the spectral data by the azimuth reference transfer function, and then applies an inverse Fourier transform to the product. These filtered complex data go through a power detection process. The results correspond to a single-look imagery. The range migration compensated spectrum is a vector containing 2048 complex terms. The length of the azimuth reference function for each look spans 1024 complex samples in azimuth. Because each single-look image is produced by processing one quarter of the total synthetic aperture (or one quarter of the azimuth spectrum as is defined by the antenna radiation pattern), the inverse Fourier transform of the fast correlation is performed on a 512 term vector.

256 samples are retained after the inverse transform, and are detected to form 256 one-look pixels. A total of four 512-vector inverse transforms are performed to obtain four sets of single-look pixels. The correlation vector size (2048) and the reference function length (1024) are such that these four single-look line segments (256 pixels each) register side by side to form a 1024 point one-look image line. An example of a single look image (1024 lines and 1024 azimuth picture samples per line) is shown in Figure 9. Each of the four vertical sections is of one particular single look. The effect of subdivision of the azimuth spectrum, which results in a stronger response in the center two looks and a weaker response in the two side looks, is clearly evident in this picture. A graphical illustration of the four single look spectral bands over the azimuth spectrum is shown in Figure 10.

3.2.9 Multi-Look Overlay Program

This program performs the four look overlay of the single-look images produced by the azimuth correlation program. The pixel intensity values are averaged to produce the four-look imagery. A square root operation is applied to the intensity value of the final four-look pixel. The resultant value is encoded linearly by a 8-bit pixel word. The 8-bit amplitude representation is capable of providing an output dynamic range of approximately 48 dB.

3.2.10 Pixel Merge Program

This program merges the multiple-look overlayed image blocks, each of which is 256 (azimuth) by approximately 1100 pixels, into an image of approximately 5800 lines and 6144 pixels per line. The resultant image corresponds to a SEASAT-A SAR frame covering a 100 km x 100 km area on the ground surface, and

(a)

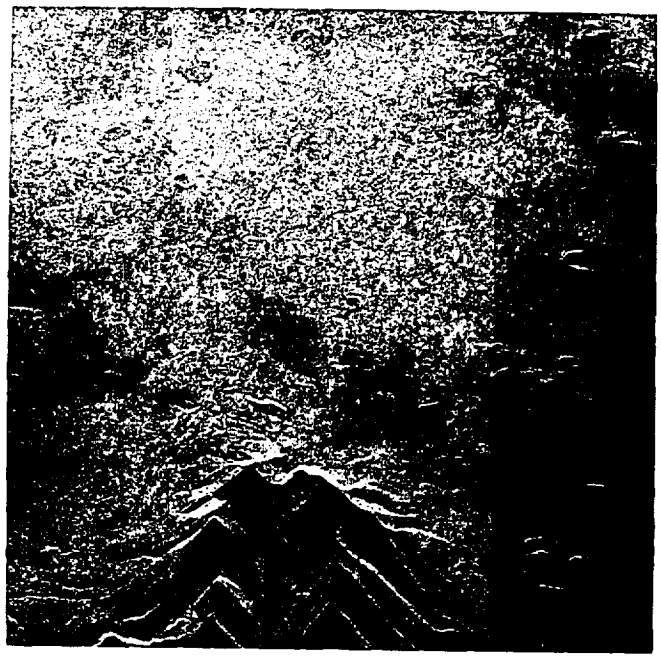

(b)

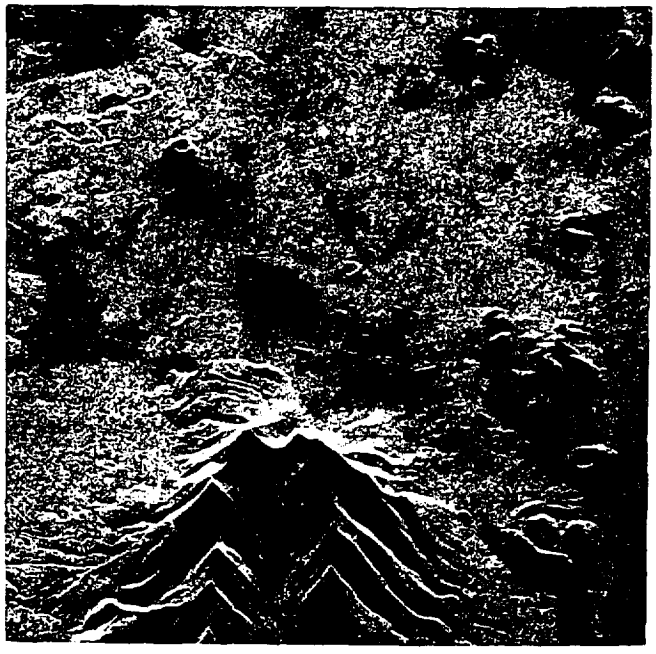

Figure 9. Single-Look and Four-Look SEASAT SAR Imagery (1024 x 1024 Pixels)
(a) Single-Look Image
(b) Four-Look Image

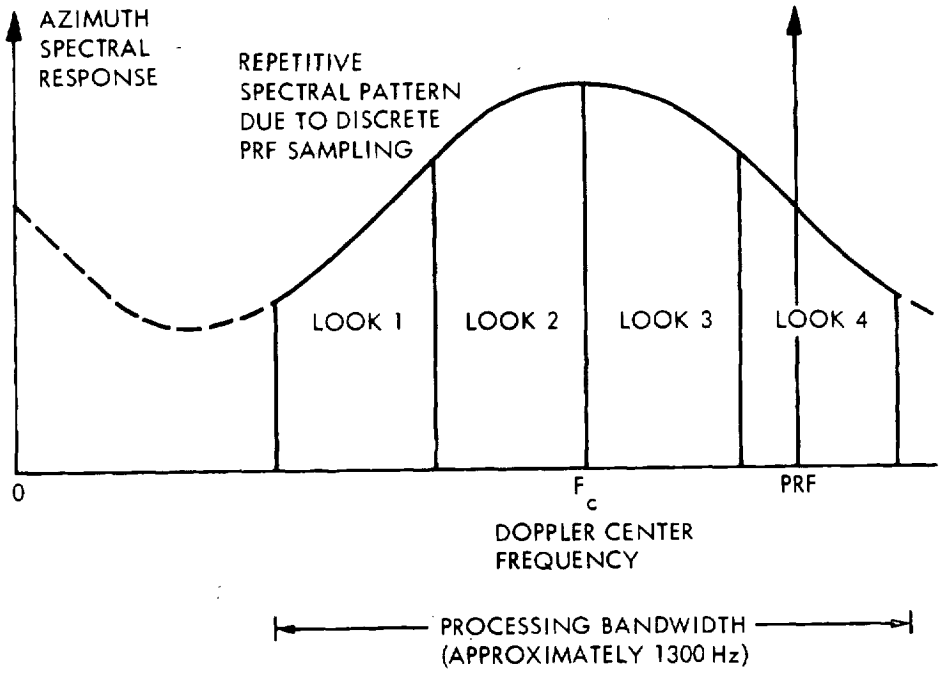

Figure 10. Partitioning of Azimuth Spectrum for Multiple-Look SAR Processing

has 25m resolution, 4 looks. An example of such a merged 100 km x 100 km SEASAT SAR imagery is shown in Figure 11. This image covers a section of the California Coast, south of Los Angeles. The data were obtained on September 25, 1978, SEASAT revolution number 1291.

3.2.11 Executive Program

This program serves as the executive controller for the sequential execution of the correlation processing programs defined in 3.2.5 to 3.2.10. The set of parameters entered into this executive program to initiate the IDP processing are listed and explained in Table 2.

Table 2. List of Input Parameters for IDP SEASAT SAR Processing

LBIAS	Starting Line Number of raw data stored on disk
NBIAS	Starting sample number of each record
ISTEP*	Amount of range walk compensation over 1024 lines
RINC*	Sign of sample increment for range walk compensation
RCHG*	Period for increment (= 1024/ISTEP)
LAZI	Number of azimuth lines to process in each look
FD	Doppler center frequency
FDD*	Center frequency offset for range delay calculation associated with range walk compensation
FRATE	Doppler frequency rate over synthetic aperture at near swath
FRCON	Decrement of Doppler frequency rate every 64 pixels in range
PD	Reference weighting coefficient for sidelobe suppression

*Parameter whose value dependent on ISTEP and can be eliminated.

Figure 11. An Example of a 100 km x 100 km IDP Processed SEASAT SAR Imagery

3.3 IDP Operation Procedure

To produce a 100 km by 100 km SEASAT-A SAR imagery on the IDP, the standard procedure comprises the following steps:

1) Obtain the earth coordinates, the SEASAT SAR experiment site, and any additional constraints regarding the time or conditions of the radar observation. Select a SEASAT orbit revolution containing data from the experiment site.

2) Obtain the starting time of that revolution from the Catalog of the SEASAT SAR Experiment Sites [7]. Next, calculate the time at which the satellite began to collect data from the experiment site.

3) Play the HDRR tape corresponding to the selected orbit revolution and execute the SAR raw data input program (3.2.1) to store a prescribed set of SEASAT-A radar data on the 300 M byte computer disk memory. The data begin at the time determined in Step 2 and include an amount that corresponds to a data acquisition period of approximately 18 seconds.

4) Execute the data preprocessing program (3.2.4) to obtain accurate estimates of SEASAT-A SAR azimuth correlation parameters.

5) Enter the parameters from Step 4 into the IDP executive program and initiate its execution. The current system incorporates 15 loops of the correlation programs -- 3.2.6 to 3.2.10. The result of each loop is a block of four-look imagery of approximately 1200 by 2048 pixels. These image data are output to an intermediate computer tape.

6) Initiate a second state of the merge program which merges the 15 sub-blocks of the processed imagery into the final image format which has approximately 5800 azimuth records and 6144 samples per record. This merged 100 km x 100 km SEASAT-A SAR image frame is stored on a 1600 BPI (bits per inch), 9-track computer compatible tape (CCT).

3.4 IDP Output CCT Format

The format of the IDP output tape which contains a 100 km x 100 km SEASAT-A SAR image frame is provided in Table 3.

Table 3A. Seasat Image CCT Format

(File 1)	
HEADER	Record
DATA LINE 1	Record
DATA LINE 2	Record
DATA LINE 3	
.	
.	
.	
.	
LAST DATA LINE	Record
TM	
(File 2)	
HEADER	Record
DATA LINE 1	Record
.	
.	
.	
.	
TM	
.	
.	
.	
.	
(Last File on Tape)	
HEADER	Record
DATA LINE 1	Record
.	
.	
.	
TM	
TM	

TABLE 3B

HEADER RECORD FORMAT

Item	Description	Bytes	Location	Remark
1	Title: 'JPL DIGITALLY PROCESSED SEASAT RADAR IMAGE'	44	1-44	
2	Data Tape ID Code: xxxxyyyy	8	45-52	xxxx = orbit number (REV) yyyy = tape number
3	Frame Starting Time: DDD:HH:MM:SS	12	53-64	actual time of data taken
4	Receiving Station Identification: SSS	4	65-68	Where sss is three character of station ID: ULA = Alaska GDS = Goldstone MIL = Merrit Island UKO = Oak Hangar SNF = Shoe Cove
5	Processing Date: DA-MON-YR	12	69-80	
6	Processing Run: rrrr	4	81-84	rrrr = processing run number (begin with 1)
7	Latitude of Target Area: xxx:yy:N(or S)	8	85-92	xxx degree yy second N = North S = South

TABLE 3B

HEADER RECORD FORMAT (Continued)

Item	Description	Bytes	Location	Remark
8	Longitude on Target Area: xxx:yy:w(or E)	8	93-100	xxx degree yy second W = West E = East
9	Site: (name of target area)	24	101-124	
10	Number of Sample/Line N_S	2	125-126	$N_S \leq 6144$
11	Total Number of Lines N_L	2	127-128	$N_L \leq 6144$
12	Pixel Spacing in Azimuth M_A	2	129-130	Typically $\sim$ 16 meter
13	Pixel Spacing in Range M_R	2	131-132	Typically $\sim$ 18 meter
14	Resolution in Azimuth R_A	2	133-134	Typically 25 m
15	Resolution in Range R_R	2	135-136	Typically 25 m
16	Blanks	6008	137-6144	

4. IDP PERFORMANCE SUMMARY

The nominal performance of the IDP system in producing SEASAT SAR imagery is summarized in Table 4. Several key issues in the performance evaluation are discussed here.

Table 4. Summary of Image Parameters of Nominal IDP Produced SEASAT SAR Imagery

Input Raw Data	4 bits/sample
Range Resolution	25 m
Azimuth Resolution	Approximately 25 m
Range Peak Sidelobe ratio	-15 dB
Azimuth Peak Sidelobe ratio	-6 to -9 dB
Number of Looks	4
Pixel Dynamic Range	Selectable 48 dB (over 70 dB total) in 8 bits amplitude
Pixel Radiometric Accuracy	TBD[1]
Pixel Geometric Accuracy	TBD[2]

1. Processor gain over swath depends slightly on the input Doppler center frequency value of its closeness to the Doppler centroid. Uncertainty is mainly associated with gains in radar sensor and SAR data communication link.

2. Knowledge of pixel relative position is likely within $\pm$ 100 m over a flat area. Absolute accuracy can be much poorer due to uncertainties in the platform position and data timing which remains to be calibrated.

4.1 Resolution Performance

The IDP processing algorithm as described in Appendix A is capable of achieving a SEASAT SAR image resolution of 25 meters in both range and azimuth. A routinely produced image may have a resolution slightly worse than 25m due to error in estimating SAR processing (focusing) parameters. The IDP processed corner reflector array scene near Goldstone Tracking Station is shown in Figure 12a. The corner reflectors, each of which has a dimension of 3m or less, appear as distinctive points in the image. Interpolation of pixels near the peak responses of the reflectors indicated a 3 dB resolution of approximately 25m in range and 35m in azimuth. A refined preprocessing procedure installed in June 1980 yields consistently highly accurate estimates of processing parameters. Resolution broadening due to residue error in the estimated parameters obtained by the refined process is expected to be within 5m.

4.2 Sidelobe and Dynamic Range Performance

Detailed performance evaluation on intergrated sidelobes, dynamic range, contrast ratio, and image modulation transfer function is being conducted at the present time. By using a step-function to approximate the range curvature as described in Appendix A, the integrated side-lobe ratio is of approximately -6 to -9 dB. For truely distributed targets, e.g. ocean, this integrated-side-lobe ratio implies an image contrast of approximately 6 to 9 dB. The IDP produced pixels are represented in amplitude format. The contrast or side-lobe ratio observed in the amplitude domain is half of the dB values discussed above. The maximum possible dynamic range for an eight-bit pixel in amplitude representation is of 48 dB which is derived from the ratio of the biggest value 255 and the minimum discriminatory interval, i.e. 1.

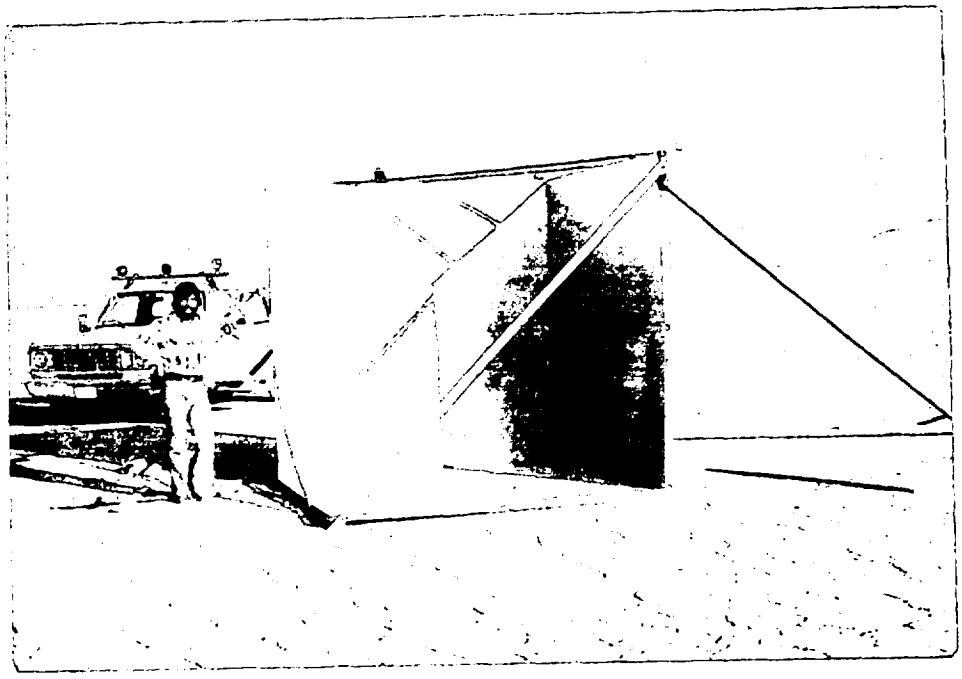

Figure 12a. Picture of a 2.6m Cubic Corner Reflector

Figure 12b. Corner Reflector Array in a SEASAT SAR Image

4.3 Radiometric Calibration

SAR data input to the IDP are quantized to a 4 bit integer with a range frequency offset as described in the previous section. Each four bit integer assumes a value from 0 to 15. These positive integers can also be treated as bipolar signals of mean value 7.5, and a data value ranging between $\pm$ 7.5. The theoretical gain of the SEASAT SAR processing is the product of the following three factors: time-bandwidth product of the range linear FM-chirp waveform, time-bandwidth product of the azimuth chirp waveform per look, and the square root of the number of looks. The numerical values of these three factors are of approximately 642, 200, and 2, respectively. The intensity gain of a pixel response from its strength in SAR echo signal to that on the processed imagery is therefore 54 dB. The corresponding gain in amplitude strength is 27 dB.

The amplitude gain of IDP is calibrated using synthesized SAR echo signals of distributed and point targets. For distributed targets, Gaussian random noise of the same mean value of the SAR raw data but various standard deviations were generated and quantized into a 4-bit integer format compatible to the IDP input. Saturation was applied to data values outside of the limits of 0 or 15. These synthesized data were processed through the IDP. The square root of the mean intensity of output pixels (mean of the squared 4-look pixel values) produced from the synthesized input versus the standard deviation of the unsaturated noise is plotted in Figure 13. The SAR processor performs linearly to a level of approximately 17 dB (square root of the mean pixel intensity). Saturation of the mean output level is definitely due to the limited range of the 4-bit quantized input data. The difference between the output level and the standard deviation of the input over the linear range is the calibrated amplification of the IDP system, which is observed to be

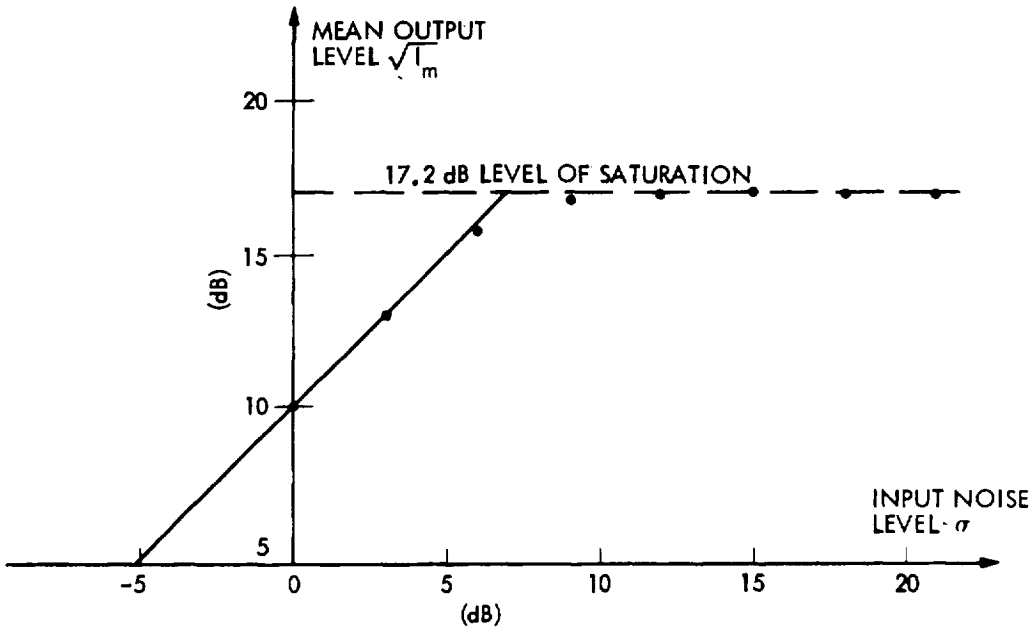

Figure 13. Measured IDP Gain Characteristics for Synthesized Distributed Targets

approximately 10 dB. For distributed targets, this measured 10 dB gain implies that the mean echo response (in quantized input domain) is approximately 10 dB below the observed square root of the mean pixel intensity. The expected gain is 12 dB due to a 16-fold controlled increase in data value in range correlation. The difference could mostly be attributed to the finite processing bandwidth in both range and azimuth, and data saturation due to limited number of quantization bits.

The quantized echo data are superposition of returns from targets over the entire radar footprint. The SAR echo response of a single point target of amplitude much weaker than the minimum quantization level 1 (over the input range 0 to 15) can not be synthesized (due to this initial raw data quantization) without readjustment of the IDP processing gain. The synthesized point target responses of various magnitudes were generated and superimposed by noise ($\sigma = 2$). The resultant pixel values (square root of the four-look summed intensity) versus the original point target amplitudes are plotted in Figure 14. The two dashed lines in the figure are the expected background level due to the finite additive noise, and the maximum output level which corresponds to 255 in amplitude value respectively. The upper line at a 45° angle to the axis indicates the expected gain performance 27 dB + 10 dB for point targets exhibit specular reflection. The dotted 45° line indicates the expected gain of a speckly target, which is 1.5 dB below the ideal point target gain due to expected speckle noise variation. The measured points suggest near linear gain performance below the 8-bit saturation level. A 2 dB loss in the measured target response in the linear region relative to the expected gain performance (solid line) is unclear and is being analyzed.

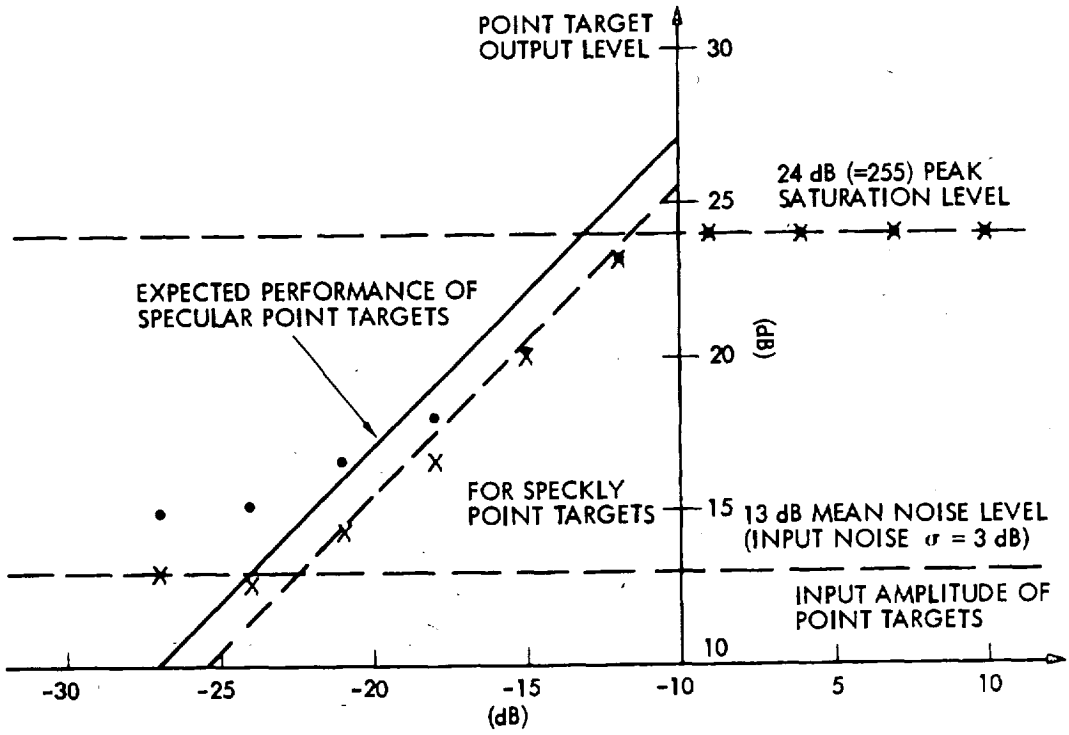

Figure 14. Measured IDP Gain Characteristics for Synthesized Point Targets (• : f_D = 0 Hz, x: f_D = 1000 Hz)

Possible sources of this difference include: course quantization in input which affects the mean input and the detected energy, and interference effect due to noise. This figure nevertheless indicates the relationship between an individual pixel value and the expected echo signal strength of that pixel in the SAR raw data.

The SAR processor is one element of the entire SAR system. Accurate radiometric calibration of the resultant imagery requires knowledge of the gain function of the radar transmitter/receiver sensor and the SAR communication link system. Discussions on such gain functions made by B. Huneycutt are included in Appendix C.

Radiometric accuracy is also affected by the resolution performance of the IDP. The effect is significant for point targets because a degraded resolution also results in a loss of target intensity response. The loss of gain of a point target due to a degraded resolution corresponds roughly to the ratio of broadening to the ideal resolution.

4.4 Pixel Location Calibration

The absolute location determination of all pixels based on SAR processing parameters and orbit determination data on the Sensor Data Record (SDR) is observed to contain $\pm$ 2 km uncertainty. The current source of error is speculated to be in interpretating the satellite ephemeris data. A study is being conducted to resolve this error. The pixel location procedure for absolute location determination can be used for each individual pixel on the image. Using this absolute location procedure, the relative pixel locations

within a 100 km x 100 km SEASAT SAR frame can be determined to within $\pm$ 25 m accuracy for targets located in a very flat area.

4.5 Throughput Performance

The current IDP processing time to produce each 100 km x 100 km, 25 m resolution 4 look SEASAT SAR image frame is approximately 10 hours. The processing is done over night shift hours. The average throughput rate is approximately 3.5 SEASAT SAR frames per week.

5. CHARACTERISTICS OF SAR IMAGERY

Radar imagery superficially resembles conventional aerial photography but differs from it in many respects. This section provides a brief summary of the basic characteristics of SAR imagery. The emphasis is on those particularly related to SEASAT SAR image interpretation. The geometric and radiometric aspects of SAR image characteristics will be treated separately in the following discussion.

5.1 Geometric Characteristics

SAR imagery is generally represented in a two dimensional format representing the along-track and cross-track directions. Geometric distortion refers to change of location of a target as it appears in a SAR image with respect to its location in a scaled geographic map. The most predominant factor which causes the geometric distortion in a typical SAR image is that the cross-track distance to a target in radar imagery usually corresponds to the slant-range distance between the target and the sensor. Because the radar sensor is placed at a position much above the ground surface, the slant-range distance measurements to individual targets do not relate linearly to the corresponding distance measurements on the planet surface. Effects due to such range distance mapping may include: ground range nonlinearity, range foreshortening, radar layover, and radar shadow. These effects are discussed respectively in subsections 5.1.1 to 5.1.4. SEASAT-A SAR imagery also exhibits a geometric distortion due to earth rotation. This effect will be discussed in section 5.1.5.

5.1.1 Slant Range/Ground Range Nonlinearity

Figure 15 illustrates the difference between a ground range (distance measured on the ground surface) and a slant range (distance measured from the sensor to a target) image. A and B, represent two features of equal size under radar illumination. Radar raw data samples are typically equally spaced in slant range distance. In this slant range display of radar imagery, those two features, A and B, will be compressed with a factor which depends on the position of the feature in the beam. Objectives in the near range are more compressed than those in the far range. The difference in appearance of a square grid containing linear and circular features in these two representations is also shown in Figure 15.

For spaceborne SAR imaging over a curved (spherical) earth surface, the relationship between a small increment in surface range, dx, to its corresponding increment in slant range, dr, (see Figure 16) can be expressed as follows:*

$$dr = dx \sin\phi = \frac{(H + R_e)\sin\theta}{R_e} dx \tag{3}$$

with

$$\theta = \cos^{-1} \frac{r^2 + (H + R_e)^2 - R_e^2}{2r(H + R_e)} \tag{4}$$

where ϕ is the radar angle of incidence, θ is the elevation look angle, H is the radar altitude, R_e is the radius of earth, and r is the slant range.

*In the following analysis, second order effects due to earth rotation and atmospheric refraction are neglected.

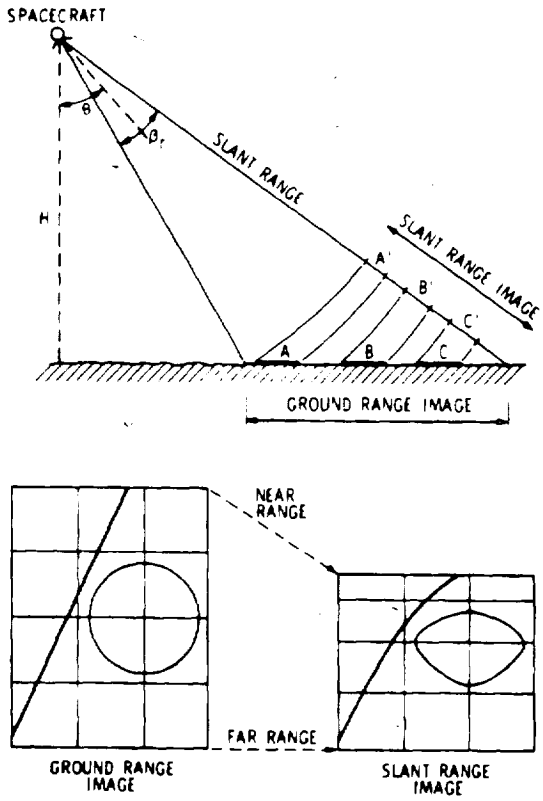

Figure 15. Geometrical Distortion in the Slant Range Imagery. Near Range Features are Compressed Relative to Far Range Features. Corrections During Ground Data Processing can be Applied to Generate Ground Range Images

Since the local value of R_e and the value of H can be determined from the satellite orbit data, and the slant range distance can be accurately determined from the delay timing of the echo, the value of dr/dx is readily determined. Ths factor also indicates the relationship of radar resolution in slant range to the resolution in ground range. The slant range resolution, Δr , is a constant as derived by the 19 MHz SEASAT pulse bandwidth, i.e.

$$\Delta r = 0.88 \frac{C}{2B} = 6.95 \text{ m} \tag{5}$$

where C is the speed of light. The ground range distance X as a function of the slant range r (see Figure 16) can be expressed as:

$$X = R_e \delta = R_e \sin^{-1}\left(\frac{r}{R_e} \sin\theta\right) \tag{6}$$

where angle δ is the one spanned by ground range distance to the center of the earth, and θ is the beam elevation look angle defined in Eq. 4. The following inverse relationship can be derived by trigonometric means:

$$r = \left\{R_e^2 + (R_e + H)^2 - 2R_e(R_e + H) \cos\frac{X}{R_e}\right\}^{1/2} \tag{7}$$

Eq. 7 is particularly useful in converting slant range representation to ground range.

Assuming a nominal SEASAT altitude of 794 km, and a radial distance from the surface to the earth's center of 6369 km near 40° latitude, the beam incidence and elevation angles versus slant range distance are plotted in Figure 17. Figure 18 contains curves which describe the relationship between slant range resolution and ground range resolution for selected cases. Figure 16 contains

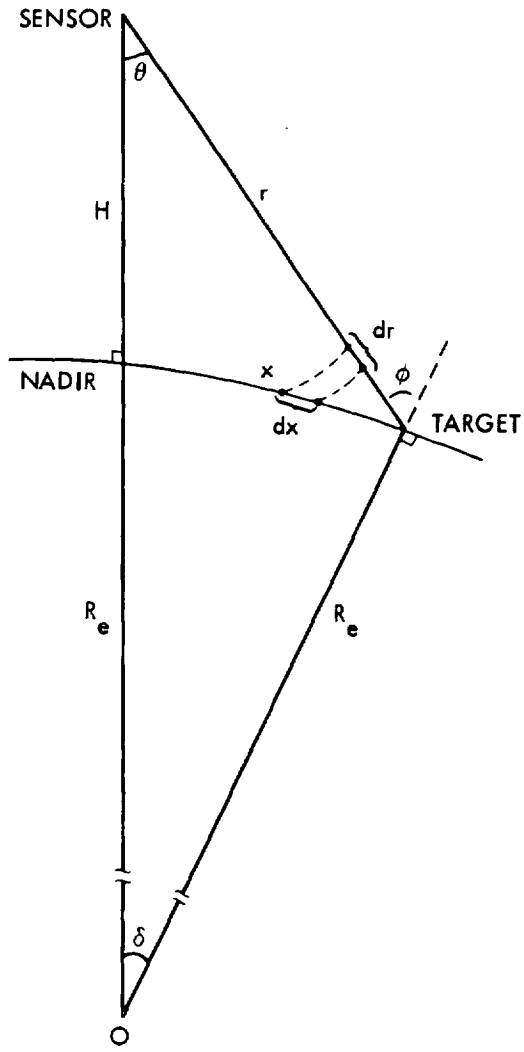

Figure 16. Slant Range and Ground Range Relationship for a Spaceborne SAR

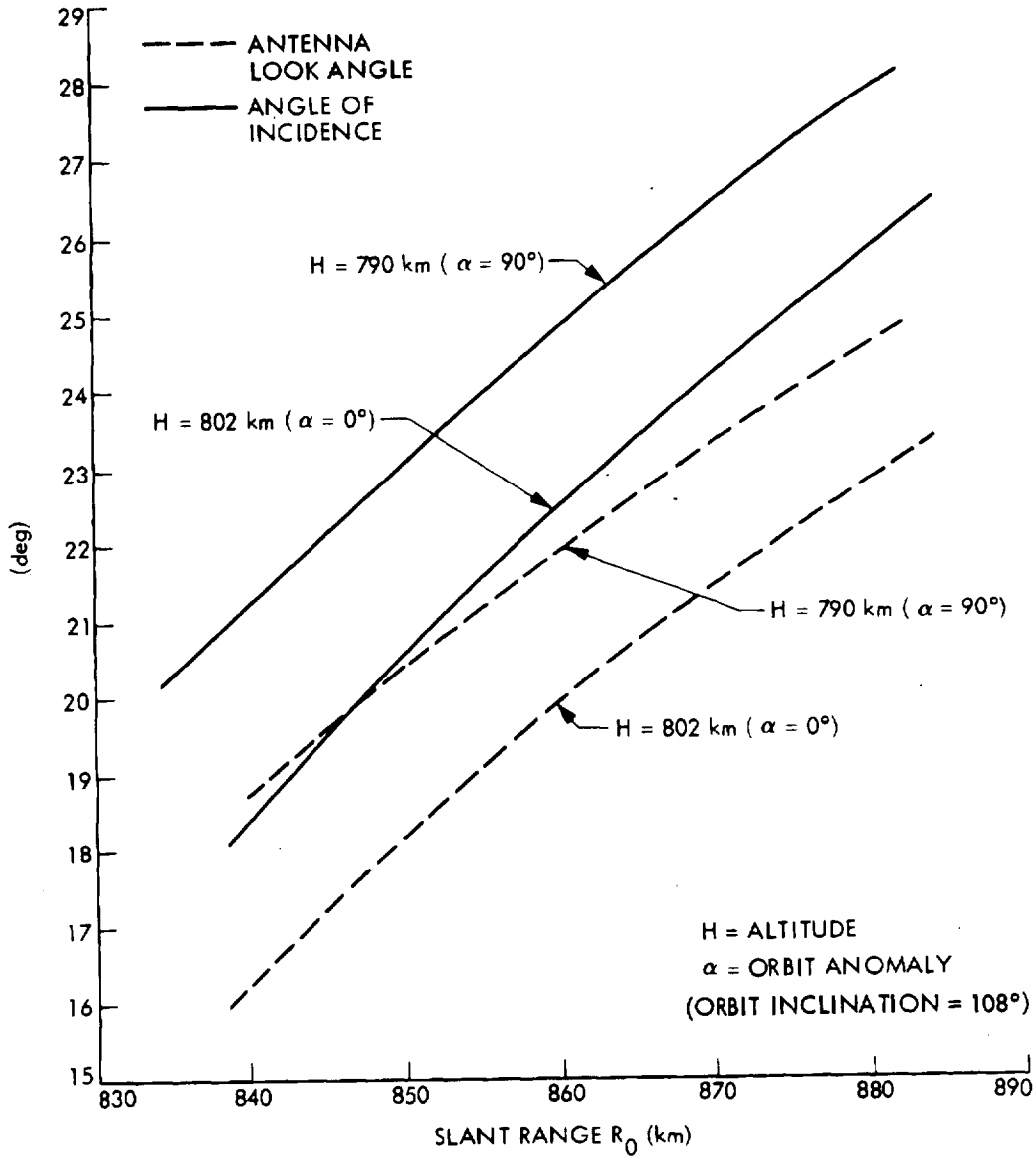

Figure 17. SAR Antenna Beam Cone Angle and Surface Incidence Angle versus Slant Range for Two Sensor Positions

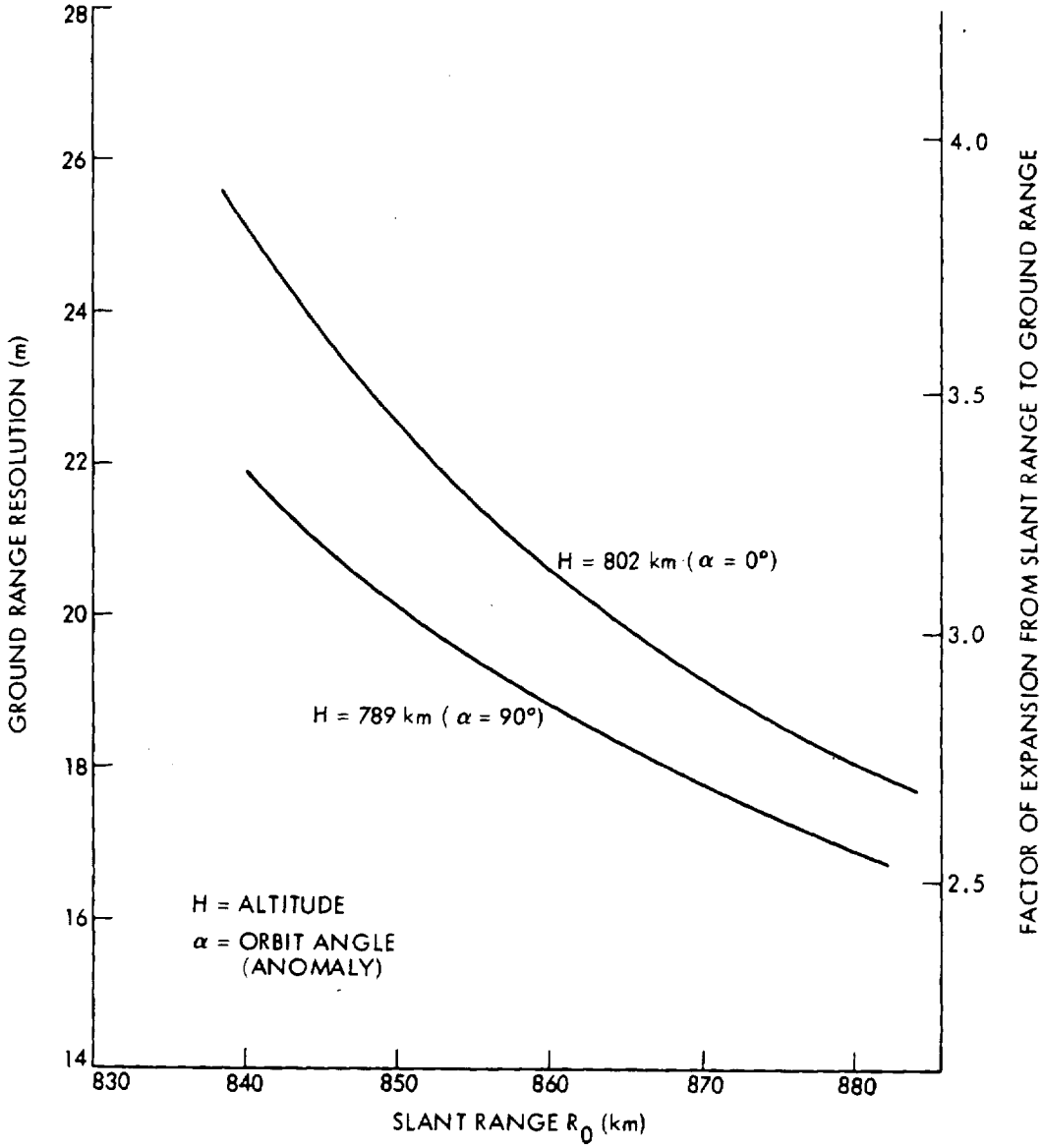

Figure 18. SEASAT SAR Ground Range Resolution and Factor of Conversion Expansion versus Slant Range (Pixel Spacing on Surface Equals 6.6m Times the Conversion Expansion Factor)

curves which describe the relationship between the slant range and the distance from the nadir point for selected cases. These three figures provide some information regarding the geometric aspects of SEASAT SAR imagery in slant range representation. The basic pixel spacing in slant range is a constant of 6.59 meters. Figure 18 indicates that range pixel spacing on the surface varies approximately from 20m to 15m from near swath to far swath. The ground range distance versus slant range can be determined from an integral of the rate of expansion function described in Figure 18. The slant range to ground range relationship exhibits a small amount of nonlinearity as shown in Figure 19.

Conversion of slant range format to ground range can be achieved through a resampling process. Calculation of the positions of new samples in slant range that correspond to equally spaced data samples on ground range makes use of the formulas given in Eq. 7. Methods of resampling were suggested in Ref. [8].

5.1.2 Radar Foreshortening [9]

Radar foreshortening, a distortion inherent to all radar imaging of irregularly shaped terrain surfaces, is the variation in the apparent length of equal terrain slopes when the slope measurements are taken at different incident angles.

Figure 20 illustrates the time intervals between equally spaced radar energy pulses which intercept the terrain at a certain range from the spacecraft. On radar imagery, the distances between terrain features are recorded as a function of the time interval required for the RF energy to tranverse the

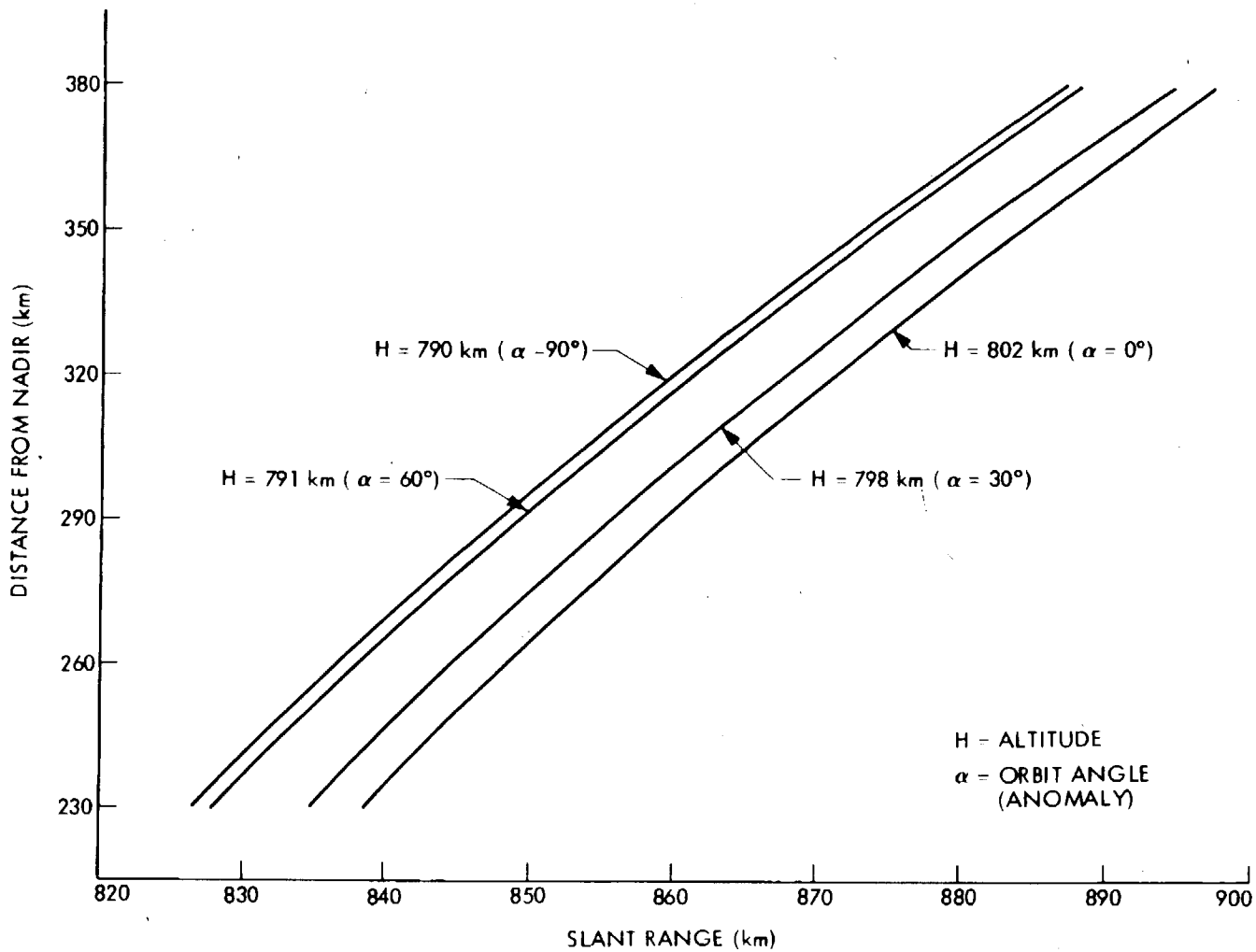

Figure 19. SEASAT SAR Target Ground Range Distance (From Nadir) versus Slant Range (From Sensor) for Four Sensor Positions.

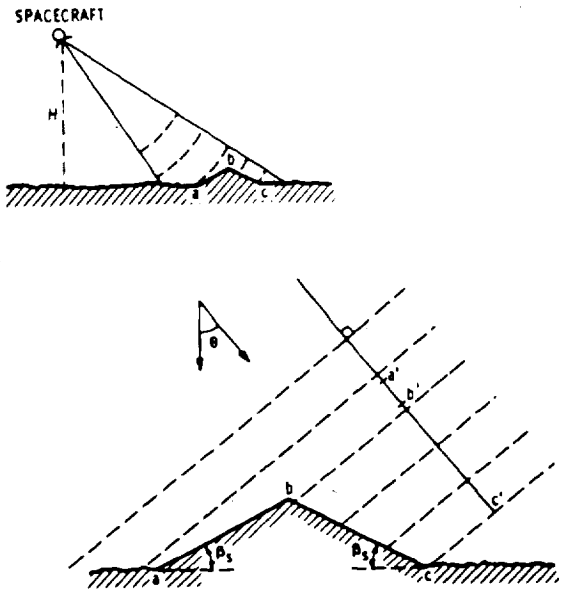

Figure 20. Shortening Effect. Slopes Inclined Toward the Radar Look Shorter Than the Slopes Inclined Away From the Radar

corresponding separation distance. The actual lengths of terrain slopes ab and bc are equal; however, in the radar imagery, the length of slope ab would appear considerably shorter than bc (a'b' < b'c'). The dimension transformation is given by

$$a'b' = ab \sin(\theta - \beta_s) \tag{8a}$$

$$b'c' = bc \sin(\theta + \beta_s) \tag{8b}$$

thus, terrain surfaces sloping toward the radar will appear shortened relative to those sloping away from the radar.

The radar foreshortening effect is minimal at large incidence angles ($\phi = 90$) and maximal at small incidence angles ($\phi = 0$). Before reaching these limits, however, large radar layover and shadowing effects appear.

5.1.3 Radar Layover [9]

Radar layover is caused by the radar signal intercepting the top of a feature before it intercepts the bottom or, more precisely, when the terrain slope is greater than the incidence angle ϕ. As a result, the objects imaged appear to "lean" toward the nadir of the spacecraft. This effect is more likely to occur when imaging terrain features with appreciable relief (such as mountainous areas), and especially if these features occur in the near range.

As illustrated in Figure 21 the tops of terrain features 1 and 2 are recorded on the imagery before the bases because the slant range distance from the radar to the top of the features R_t is less than the slant range distance R_b

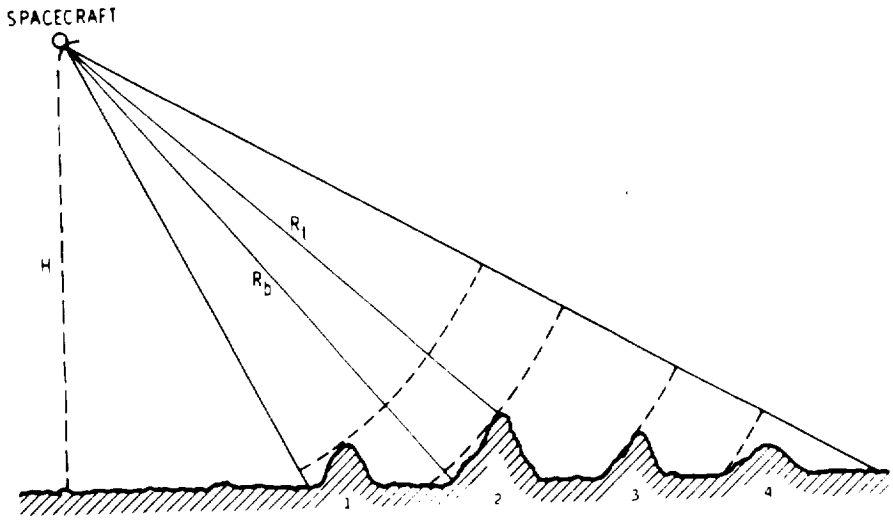

Figure 21. If the Surface Feature Slope is Larger than the Radar Look Angle, Layover Occurs. In This Case the Signal Scattered From the Top of the Feature is Received Before the Signal Received From its Bottom ($R_t < R_b$).

to the bottom. With terrain feature 3, the slant range distance R_t and R_b are approximately equal and therefore the slope is imaged nearly as a single point, or a line if the feature is elongated in the along-track direction. Terrain feature 4 is imaged normally; however, radar foreshortening now affects the apparent length of terrain slopes as discussed previously.

5.1.4 Radar Shadow [9]

Shadows which are usually present in aerial photographs are a function of the position of both camera and sun. Since radar provides its own "illumination," radar shadows appear at the side of a terrain feature most distant from the spacecraft whenever the terrain back slope exceeds the complement of the incidence. Radar images of terrain made at comparatively large look angles form shadows on the imagery that are analogous to those shadows formed on aerial photographs taken at low sun angle. Figure 22 illustrates the shadowing effect.

5.1.5 Geometric Distortion Due to Earth Rotation

This subsection treats a geometric distortion caused by various factors which affected the Doppler shift associated with individual targets as they passed through the SEASAT antenna beam. Two main factors in the distortion are earth rotation effects and the fact that the effective beamwidth of the synthetic aperture does not align with the satellite cross-track direction. The rotation effect is common to satellite scanning systems where the scan lines are gathered serially in time while the earth surface moves continuously during the imaging period. The location and orientation of the SAR image lines are strongly affected by the Doppler parameter value used in the synthetic aperture processing. The steering of the synthetic beam is subject to

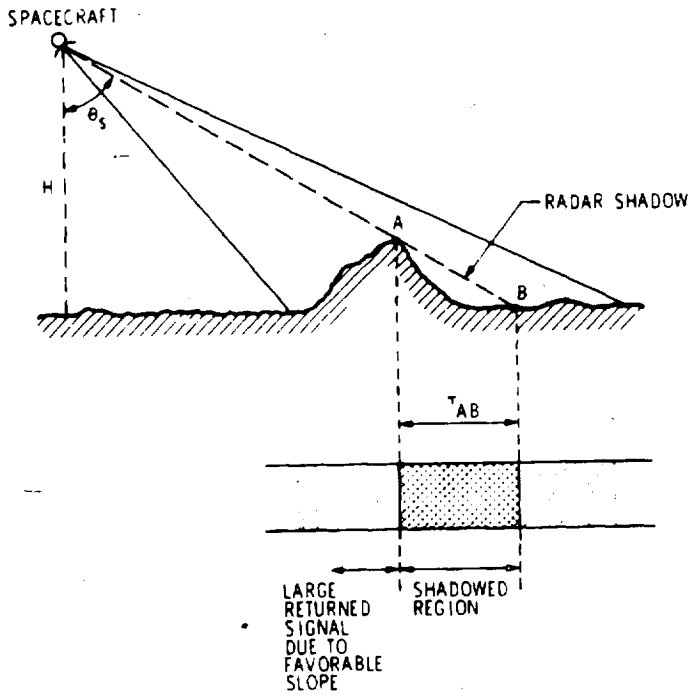

Figure 22. Side Looking Imaging Radar Geometry Showing the Shadowing Effect. This Effect can be Used for the Determination of the Feature Height.

two practical constraints: One is that the synthetic beam must be very close to the center of the physical antenna beam in order to attain an adequate signal-to-noise ratio in the imagery. However, the footprint of the physical antenna beam is often not aligned with the cross-track direction due to an error in the antenna pointing relative to the nominal azimuth angle of 90°. The other constraint pertains to the complex Doppler response of targets in the antenna footprint. Because of the effect of earth rotation in conjunction with the curvature of the earth's surface, the Doppler frequency response depends not only on the target latitude but also on the location of the target in the 100 km SEASAT SAR swath. An illustration of the Doppler frequency response as a function of the orbit angle and the spacecraft attitude was given in Figure 4. The Doppler frequency characteristics as a function of target swath position and latitude (assuming perfect antenna pointing) are plotted in Figure 23. By adjusting the SAR processing to reflect the Doppler frequency change over the swath width, it is possible to align the SAR image lines to the center of the physical antenna footprint. However, it is extremely difficult to implement a digital SAR processor which adapts to this change of target center frequency over a swath without introducing undesirable artifacts or excessive complexity. The accuracy of multilook registration or the image resolution can be adversely affected. Further, without knowing the motion of the sensor to a high degree of accuracy, there always remains a residual error.

An example illustrating the dependence of target Dopper frequency on the target location (relative to the satellite track) is described in Figure 24. A plot of the SAR antenna footprint locations corresponding to several different combinations of roll, pitch, and yaw pointing errors is presented in

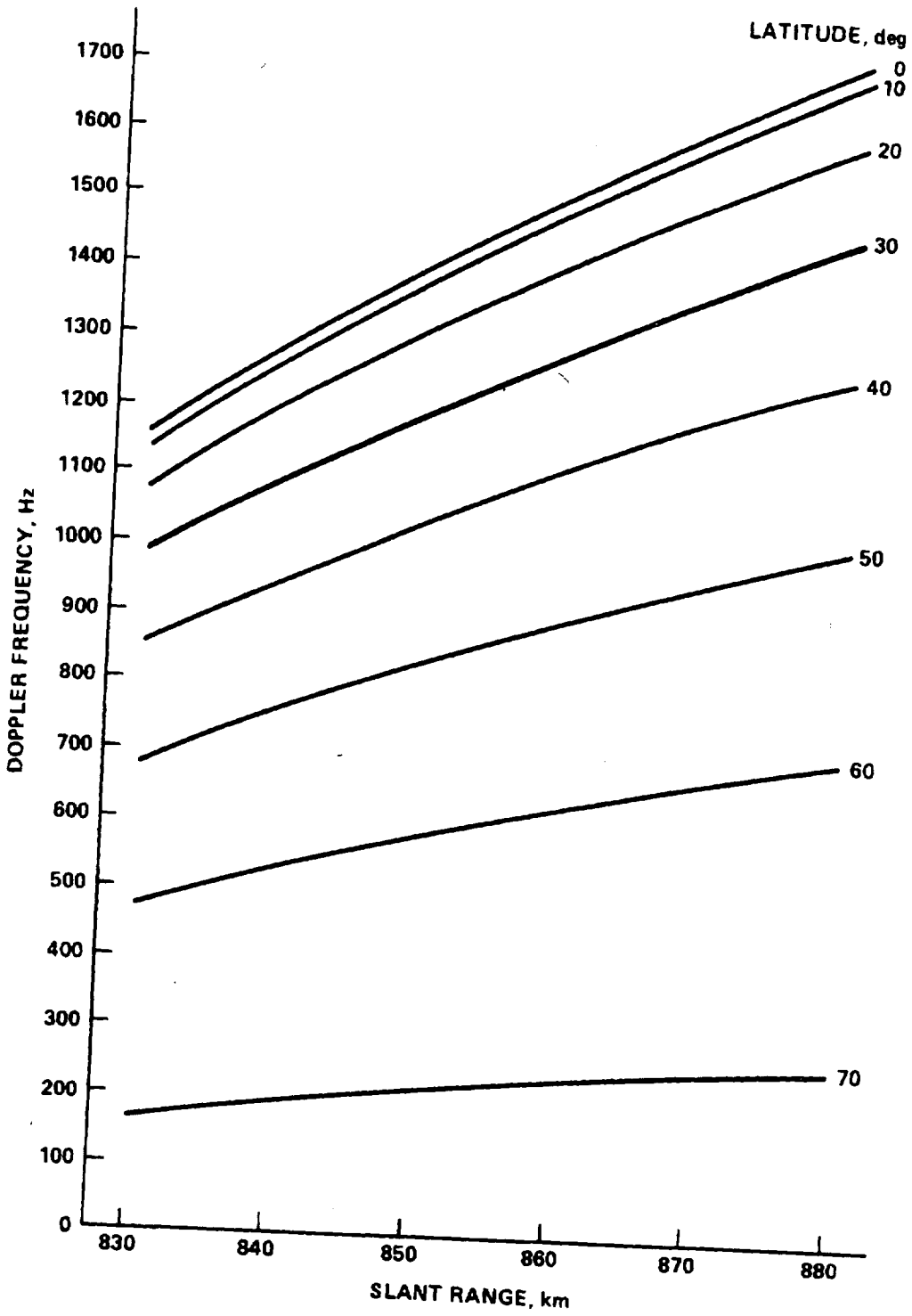

Figure 23. SEASAT SAR Doppler Center Frequency at Nominal Attitude versus Target Slant Range at Four Sensor Positions (Descending Node)

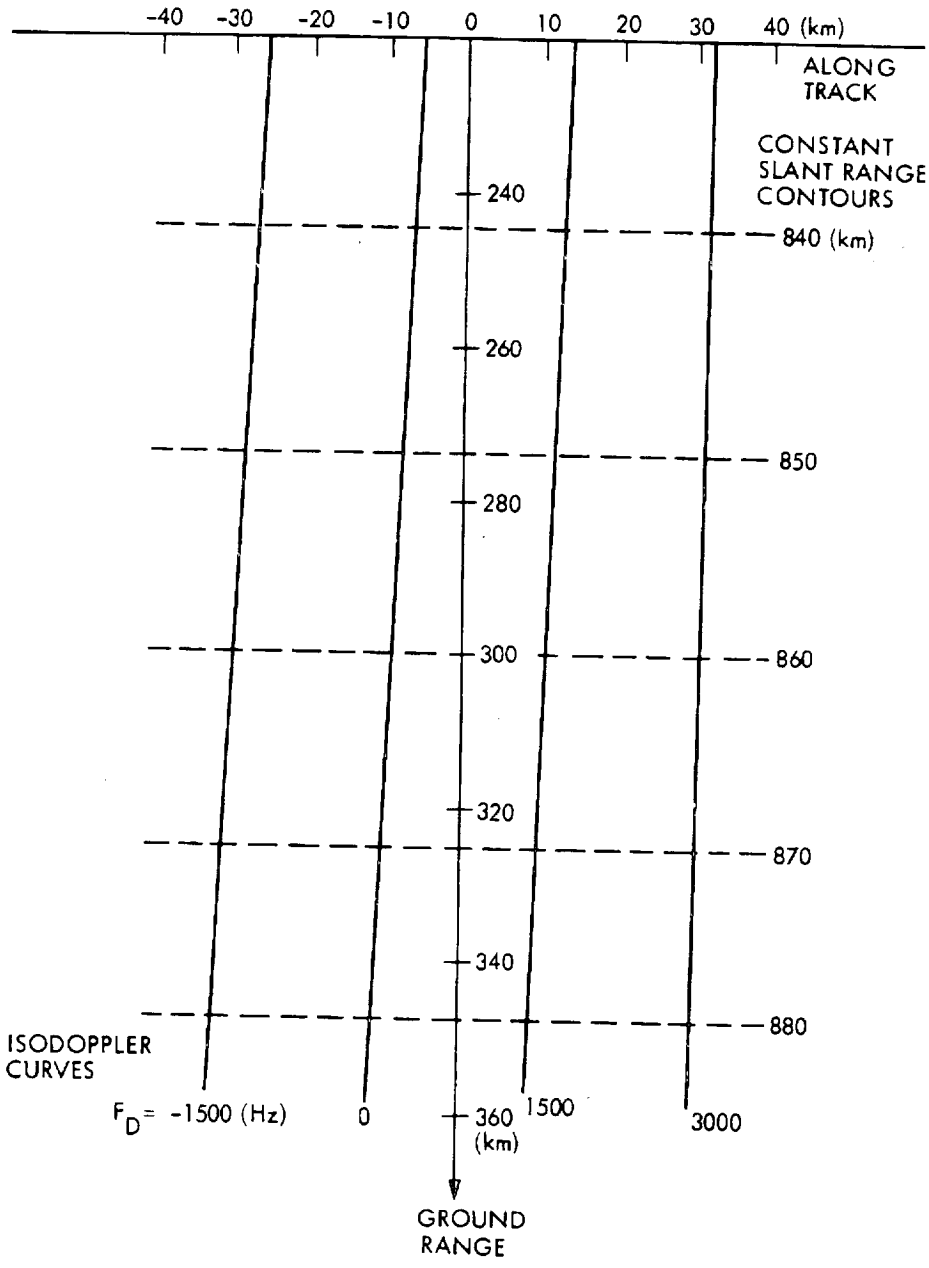

Figure 24. SEASAT SAR Instantaneous Doppler Frequency Response Over Target Surface for a Sensor Position at 30° Orbit Anomaly and Descending Node

Figure 25. It is obvious from this figure that compensation must be provided in a SEASAT SAR processor if the pitch and yaw pointing errors exceed 0.1 to 0.2 degrees. The specifications on the SEASAT attitude control system permitted pointing errors of 0.5 degrees in each axis.

For perfect antenna pointing, the SAR footprint aligns to the cross track direction. The composite effects of the earth's rotation and the azimuth displacement due to Doppler differential are now discussed for the case where antenna pointing is perfect. Square ABCD on Figure 26 (a) is assumed as a pattern in an image acquired by a high resolution real aperture radar system. Because AB and CD are acquired at two different points in time, the motion of the target field, with its direction marked by V_e, maps ABCD to an area shaped by A'B'CD on the ground surface. This form of distortion is inherent in a line-scan sensor, viewing a laterally moving subject. It is, for example, observed in imagery obtained by the multi-spectral scanner carried on the LANDSAT satellites. The angle δ produced by this effect (see Figure 26) can be approximated by the following expression:

$$\delta = \frac{V_e \cos\ell \sin S}{V_s}$$

with

$$S = \frac{\cos\alpha}{(\cos^2\alpha \sin^2\phi + \cos^2\phi)^{1/2}}$$

$$\phi = \sin^{-1} \frac{\sin\ell}{\sin\alpha}$$

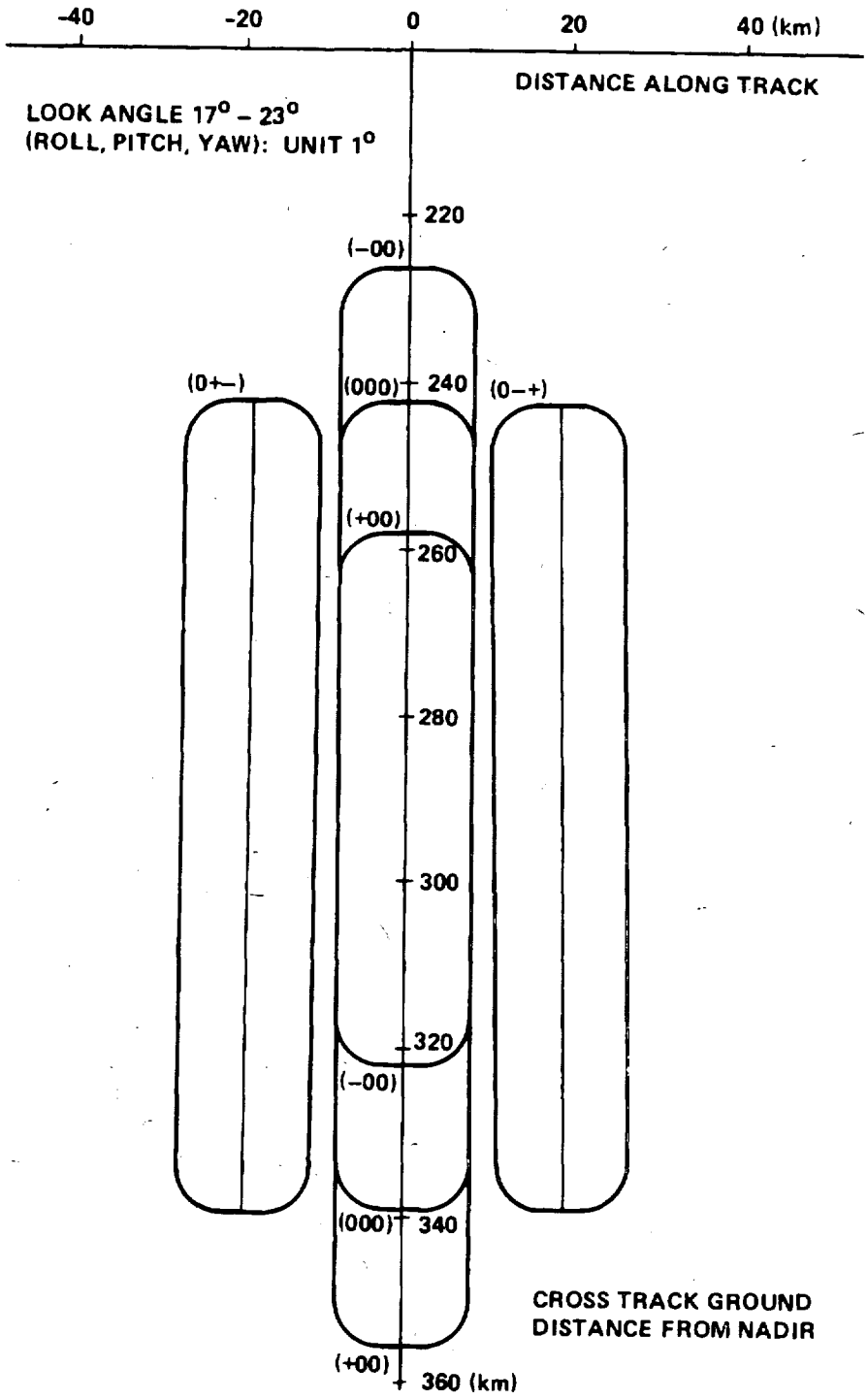

Figure 25. Location of SEASAT SAR Footprint as a Function of Attitude

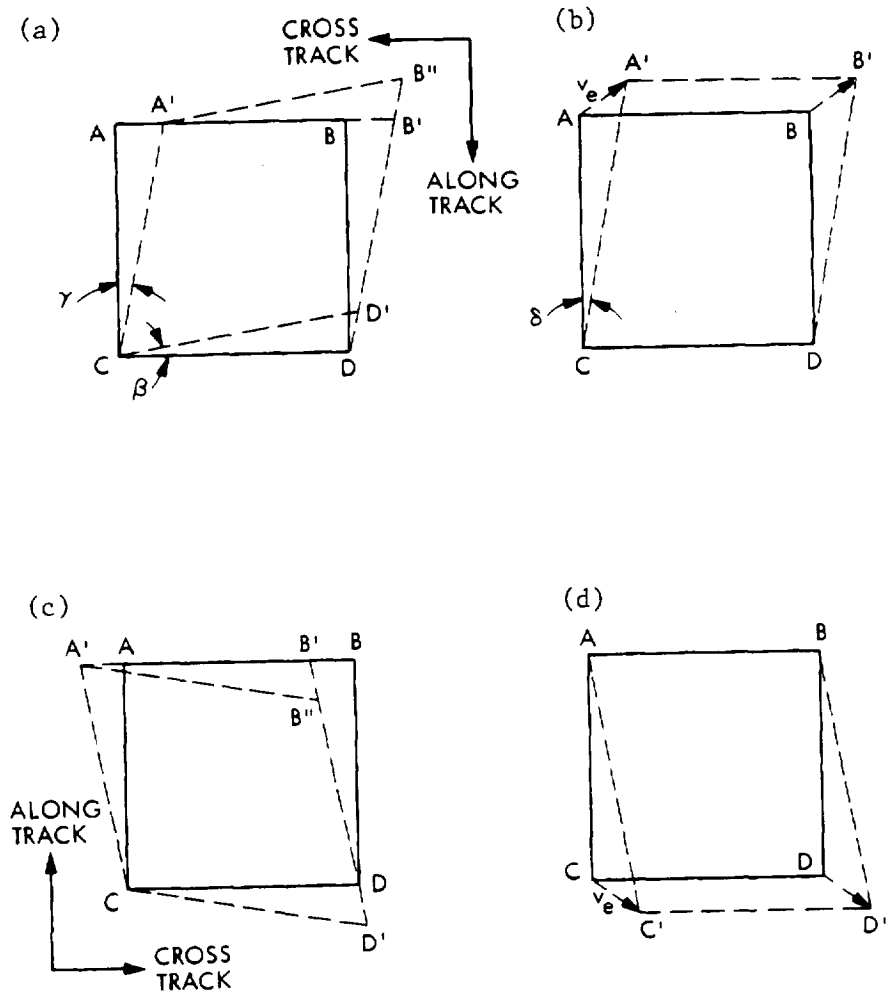

Figure 26. Geometric Distortion of IDP Processed SEASAT SAR Imaging and Distortion Due to Earth Rotation in a Line Scan Imaging System

where

V_e is the surface speed of earth rotation at equator

V_s is the surface speed of the subsatellite point

ℓ is the target latitude

S is the angle between the satellite velocity vector and the earth's rotation velocity vector at the subsatellite point

α is the angle of orbit inclination (= 108°)

and ϕ is the latitude of the subsatellite point

For a target at a latitude of 40° north, the angle α_1 is approximately 2.8 degrees.

In the SEASAT SAR system, the radar echo data must go through synthetic aperture processing to form high resolution imagery. The range walk compensation implemented in the IDP skews the echo data block to partially offset range walk present in the data. The skewed echo data block is indicated by A'B'CD on Figure 26 (b). The range walk compensation is implemented in discrete angular steps. Typical values of this skew compensation angle γ are approximately 0.9, 1.8, and 3.6 degrees. They correspond, respectively, to adjustments of 16, 32, and 64 output pixels per every 1024 pixels in azimuth. The adjustments compensate for Doppler center frequency offsets of 360, 720, and 1440 Hz, respectively. This method of data block skewing to compensate for range walk produces stepped edges in the processed imagery. An example of such an edge is depicted in Figure 27. This figure illustrates the boundary of the 100 km x 100 km SEASAT SAR image shown in Figure 11.

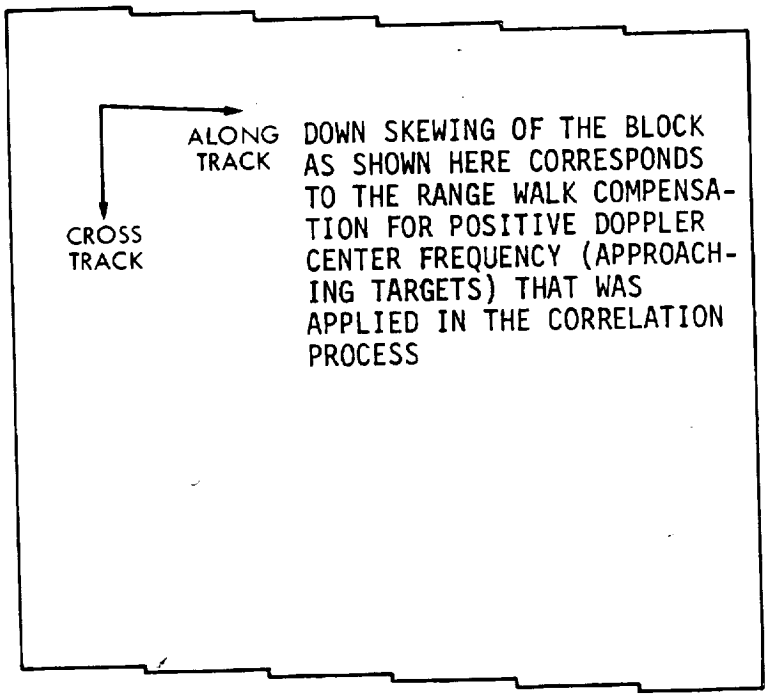

Figure 27. Image Data Block Skewing as a Result of Range Walk Compensation

The IDP azimuth processing uses a single Doppler frequency value for the entire 100 km swath width SEASAT SAR processing. The nature of the processing is such that it enhances a target which has a response that accurately matches the reference function. When a single Doppler frequency value is used over the entire swath width, the resultant image lines are aligned with corresponding "isodoppler" curves of that frequency on the ground surface. The motion of the earth together with the surface curvature causes the Doppler frequency response to vary along the cross-track direction. The result is that isodoppler curves are in general at a tilted angle relative to the cross-track direction as shown in Figure 24. To avoid complexity in the image recording process, the output image lines are given a cross-track orientation. Consequently, a geometric skew distortion is introduced into the images. This effect is described by angle β and the further skewed parallelogram A'B'CD' in Figure 26 (b).

The angle β can be approximately evaluated in the following manner. The difference between the assumed Doppler frequency and its true value is called the Doppler mismatch and denoted by the symbol Δf. The associated position displacement in azimuth, Δx, can be approximated using the following formula:

$$\Delta x = \frac{\Delta f}{\dot{f}} V_s$$

where $\dot{f}$ is the instantaneous rate of Doppler frequency change at the center of beam, and V_s is the speed of the subsatellite point. This expression is derived from the correlation of two linear FM chirp pulses of the same chirp rate $\dot{f}$, but differing in their center frequency by Δf. Another simpler way to analyze the problem is based on the familiar aircraft SAR equations [3], i.e.

phase delay $\phi = \frac{2\pi x^2}{\lambda R} = \frac{2\pi V^2 t^2}{\lambda R}$

Doppler frequency $f = \frac{2vx}{\lambda R} = \frac{2V^2 t}{\lambda R}$

frequency rate $\dot{\Delta f} = \frac{2V^2}{\lambda R}$, from $\Delta f = \frac{2V\Delta x}{\lambda R} = \frac{2V^2 \Delta t}{\lambda R}$

A simple manipulation of the last two expressions also leads to the formula given previously.

At a latitude of 40° north, a typical value of Δf which measures Doppler differential between near and far swath positions is 200 Hz. (Compared to the Doppler bandwidth of approximately 1300 Hz, a mismatch of $\pm$ 100 Hz produces a very slight degradation in the image SNR.) The values of $\dot{f}$ and V_s are approximately 520 Hz/sec and 6600 m/sec, respectively. The relative displacement in azimuth, ΔX, is roughly 2.5 km from near to far ends over the swath width.

The azimuth skewing angle β is expressed as

$$\beta = \frac{\Delta X}{W}$$

where W is the 100 km swath width. With ΔX being 2.5 km, the β angle is approximately 1.5 degrees.

The true composite skew angle is roughly the sum of the range walk compensation angle γ and doppler mismatch skew β. The distortion of a SEASAT SAR imagery acquired during an ascending node is opposite to that acquired in a

descending node as described in Figure 26 (a) and 26 (b). Figure 26 (c) and 26 (d) illustrate such effect corresponding to SAR imagery obtained in an ascending node. Note that the discussion given here does not include the effects associated with extraneous yaw and pitch deviations. It is also noted that angle γ can be chosen such that the sum γ and β is about equal to the inherent earth rotation effect δ. In this case the processed imagery is relatively free from the distortion due to the natural earth rotation effect. A subsequent slant range to ground range conversion can be performed to provide a good geometric representation for SEASAT SAR imagery. Such a first order geometric compensation scheme is intended to be investigated in the near future.

5.1.6 Other SEASAT SAR Sensor Related Geometric Distortions

A change in the apparent geometric location of a target can occur if the SAR sensor changes its parameters during its data acquisition period. Changes in the radar PRF or the position of the echo sampling window affect the geometric distortion most. A common result is that one part of the image is totally displaced in range from another part. Such distortion was observed in a few of the processed images. However, the transition region does not exhibit a sharp discontinuity in the scene associated with the PRF change. Observation of this distortion was made based on noticing dislocation of known target patterns on the ground surface.

5.2 Radiometric Characteristics

The apparent brightness of a target in SAR imagery exhibits certain characteristics which are very much different from that of an optically sensed

image. The first two characteristics treated in the following discussion, namely the Rayleigh speckle and random noise, are inherent to SAR imaging and appear in almost all the SAR image scenes. The later three characteristics, namely the pulse compression sidelobes, the ambiguity responses, and the weak signal suppression, are dependent upon the design of the radar system. They are not apparent in most of the SEASAT SAR imagery. They are observed only in images which contain extremely bright targets. The purpose of including such unusual responses into this discussion is to provide the basic information and typical examples to enable proper discrimination between them and other natural causes in the SEASAT-A SAR imagery. It is also observed that target response depends greatly on the SAR viewing geometry, especially for a structured target pattern such as that of city blocks. An example is shown in the two images in Figure 33.

5.2.1 Rayleigh Speckle Effect

The Rayleigh speckle effect [10, 11] is particularly apparent in coherent imaging of an objective having a surface roughness comparable to the wavelength of the light source. The effect is caused by interference of light scattering from those scatterers located more or less uniformly but randomly over the target surface. For a large number of scatterers, the resultant amplitude received by the sensor is random, and the resultant amplitude response is best characterized by the Rayleigh distribution. The two orthogonal - I,Q, - signal components prior to the amplitude detection exhibit a normal distribution as a result of the central limit theorem which applies to the sum of the large number of random inputs. The corresponding intensity response, which is a square of the amplitude, follows the exponential distribution. That is, for an expected intensity response $\overline{I}$, the detected

strength I after synthetic aperture processing has the following probability density function:

$$P(I) = \exp(-I/\bar{I})$$

Note that the standard deviation of this distribution equals the mean value I. Other characteristics of these distribution functions can be found in many mathematical statistics references. The interference pattern may vary as a function of the perspective viewing angle along-track and the radar carrier frequency. Independent measurements can be made by changing such parameters. The idea of multiple-look processing of SAR data is to obtain such independent measurements of each pixel and to average them to reduce the random variations. Another approach is to assume that the surface reflectivity varies rather slowly relative to the dimension of a pixel. It is therefore possible to reduce the speckle variation by averaging adjacent image pixels.

The IDP produced SEASAT-A SAR imagery incorporates a 25m resolution, 4 looks processing. Each look is produced from one quarter of the available azimuth spectral band (coherent processing using full spectral band results in a single-look image with an azimuth resolution of 6 meters.) In normal IDP processing the azimuth resolution of each look is 25m meters. The multiple-look averaging is done in the intensity domain. It was determined in a previous study that intensity averaging provides a more accurate representation of the target reflectivity.

The four look averaging reduces the intensity variation by a factor of 2 (the square root of the number of looks). The remaining fluctuation is still high. An example of such "speckley" variation is shown in Figure 28 (a) where a section of the 25 m, 4 look SEASAT-A SAR imagery over agricultural fields in Imperial Valley, California, is illustrated. The speckle variation within each field is clearly visible. Figure 28 (b) shows an image of the same area obtained by averaging the pixels shown in the previous picture. The speckle variation is reduced at an expense of degrading the spatial resolution of the image. Some discussions on the effects of speckle on image spectra are given in [12]. A copy of this reference is also given in Appendix B.

Radar backscattering from sea surface may also fit the Rayleigh statistics model. This is because the short wavelength waves which typically ride on the swells represent random scatters on the ocean surface.

Rayleigh speckle is observed over targets that have a surface roughness comparable or greater than the radar wavelength. For certain targets where their surfaces are relatively smooth and are approximately perpendicular to the direction of incident wave propagation, the intensity variations over the looks are small. Such targets usually exhibit very strong reflectivity and are generally referred to as "specular" targets.

5.2.2 Thermal Noise Effect

The detected signal power in a SAR imagery has two components. They are the radar RF power reflected from the target area, and the noise power introduced by the SAR sensor, the telemetry link, and the processing system. In an intensity representation of the correlated imagery, these two components are

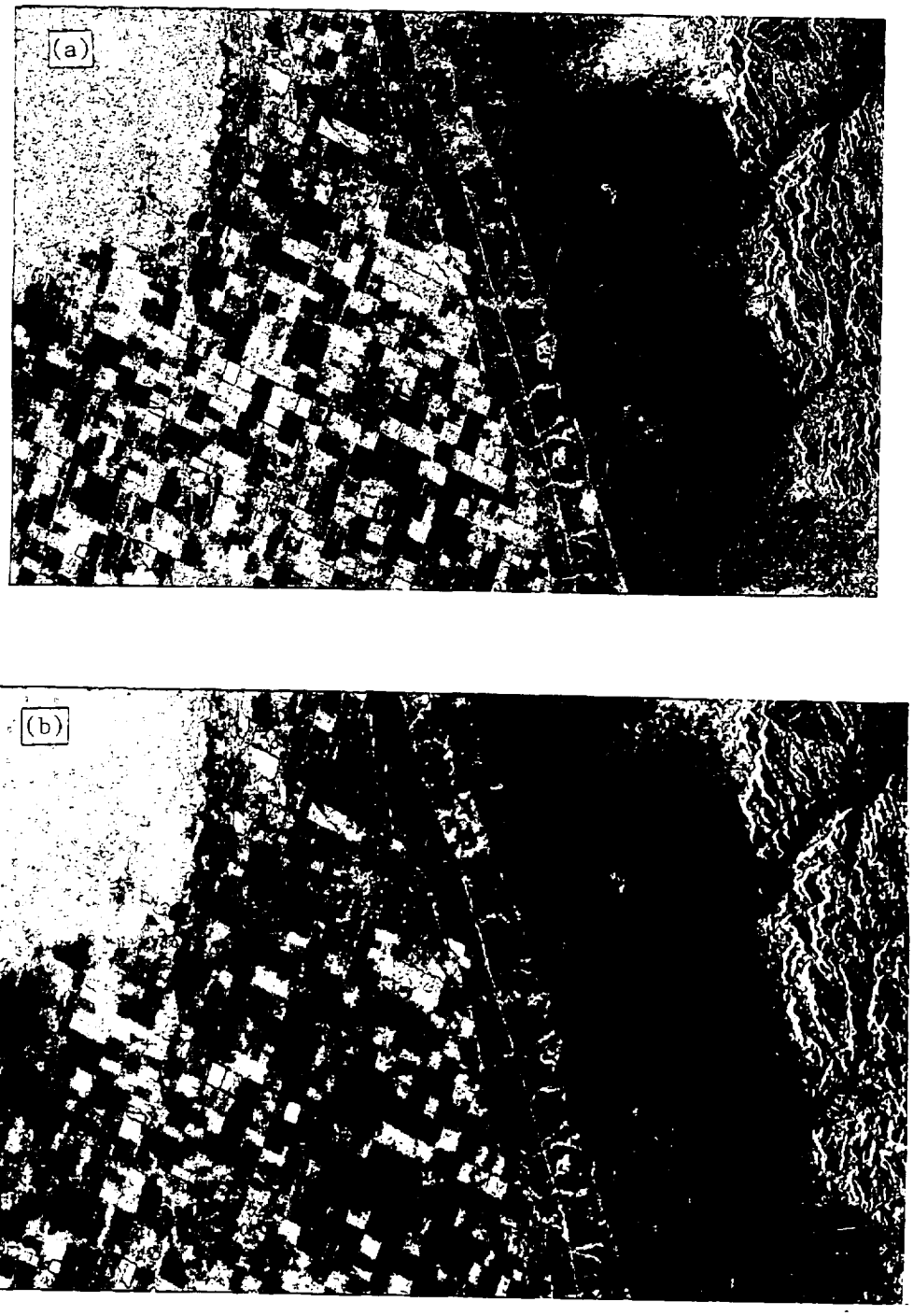

Figure 28. Speckle Reduction Through Image Smoothing
(a) A 25m Resolution Image Over Imperial Valley, California
(b) A Smoothed Lower Resolution (Approximately 60m) Rendition of the Same Area as Shown on (a)

additive. The probability density function of the pixel intensity still follows the exponential distribution as described in the previous section, except that the mean intensity, I, is now expressed as the sum of radar RF reflection and noise [13, 14].

$$I = S + N$$

The mean reflected signal power S depends greatly on the target reflectivity over a resolution element, and the mean noise power N is modeled as a constant for all the pixels.

As the number of looks increases, the noise component in a pixel approaches the constant value N. By knowing the signal-to-noise ratio (SNR) of the SAR system (SNR of SEASAT SAR is approximately 10 dB) and the system gain profile, the value of N is readily estimated. The expression which relates N to the SNR and the mean intensity P over the entire image is given below:

$$N = P/(SNR + 1)$$

where

$$P = S + N$$

For large number of looks, this value of N can be subtracted from all the pixel values to achieve a better representation of the target response. It is also meaningful to include other interferences such as sidelobe and ambiguity

level (to be discussed in next subsections) into the noise calculation, and to subtract these from the multiple look imagery.

5.2.3 Pulse Compression Sidelobes

The SEASAT-A SAR sensor adopted a linear FM (frequency modulation) chirp waveform to encode its transmitted pulses. The chirp waveform has a time duration of 33.8 microseconds and a bandwidth of 19 MHz. Compression of this FM chirp waveform results in a sinc function - sin(x)/x - form of impulse response [15] in the range dimension. The point target response in the azimuth dimension can also be closely approximated by the linear FM chirp waveform. Synthetic aperture correlation results in an impulse very similar to that of the range pulse compression. The detected impulse waveform resembles the square of sinc function. The response function outside the first nulls of the mainlobe are referred to as sidelobes. These sidelobes interfere with the target response at other pixel positions. The result is a loss of detectability for weaker targets which are located very close to a strong one. The sum of sidelobe interferences at any pixel position due to other targets in the surrounding area can be modeled by calculating the mean energy in all sidelobes. The ratio of the sidelobe response level (which may also include the ambiguities - 5.2.4) to that in the main-lobe is called the integrated-side-lobe ratio (ISLR). This ISLR is often used to quantify the level of target induced interference in a radar image dominated by distributed targets.

It is clear that a lower sidelobe response improves the image quality. For a linear FM waveform, it may be necessary to apply amplitude weighting to the correlation reference function to reduce the sidelobe level. The weighting

applied in the IDP processing is very moderate (cosine square plus 0.5 pedestal). The technique is to preserve the 25m spatial resolution of the correlated images as much as possible (amplitude weighting in the chirp waveform broadens the mainlobe of the correlated impulse). The range peak sidelobe in IDP produced 25m resolution, four-look imagery was measured to be approximately -20 dB, and the azimuth peak sidelobe was measured to be approximately -9 dB. Strong sidelobes are usually observed near very bright targets. An example is shown in Figure 29. The extremely bright point to the left of the image is the 26m antenna in the NASA Goldstone DSN (Deep Space Network) Tracking station. Range sidelobes are clearly observed. For weaker targets, such as the radar corner reflectors placed in the Goldstone dry lake, the sidelobes are less visible (also see Fig. 12).

5.2.4 Ambiguous Target Response Due To Antenna Sidelobes

The ambiguous target responses in correlated SEASAT SAR imagery are due mainly to sidelobes in the antenna radiation patttern. Such response can further be classified as the range ambiguities and azimuth ambiguities. The range ambiguity is caused by antenna sidelobes in the range direction. That is, echo responses due to sidelobes for targets at a much closer or further distance than those targets illuminated by the mainlobe can add to the mainlobe echo response (due to periodic radar pulse transmission and echo reception) and produce spurious targets in the correlated imagery.

In the azimuth dimension, the target Doppler spectrum corresponds to the antenna response in that direction. The finite radar PRF (pulse repetition frequency) sampling in azimuth results in the fold-over of the Doppler

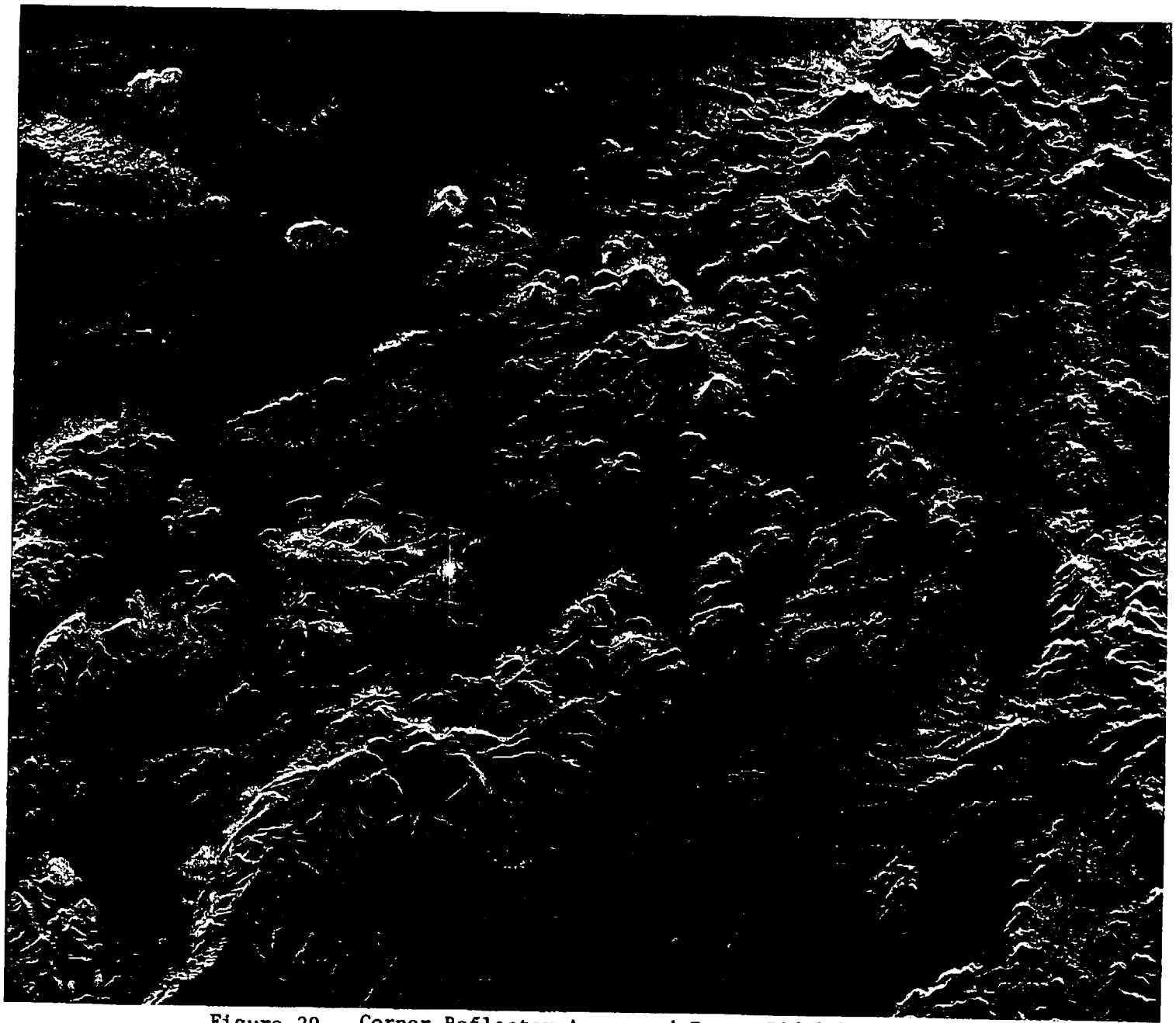

Figure 29. Corner Reflector Array and Range Sidelobes of 9m Diameter Antenna in Goldstone Tracking Station

spectral energy from the sidelobes into the mainlobe. This aliasing effect produces ambiguous target response in the azimuth dimension.

The composite ambiguity function of the SEASAT-A SAR radar system is approximately plotted in Figure 30. The upper center spot is the desired main response of a point target of the SAR system. Those points located at a further distance from the center point are ambiguous responses resulting from finite radar PRF and extended antenna radiation pattern. The spatial locations of these ambiguities can be precisely calculated according to the radar PRF value and the pulse compression parameters. The approximate locations of the range and azimuth ambiguities measured in the slant range and the along-track distances are also indicated in the figure.

The PRF ambiguities are in general very much weaker than the main response so that they do not normally produce visible effect in a processed imagery. However, exceptions due to strong targets do exist. An example of such azimuth ambiguity is shown in Figure 31. The figure contains a section of the SAR image containing New Orleans. The brighter features in the lake are caused by the ambiguous responses of the very bright area approximately six kilometers south east of the lake shore. Range ambiguities are more difficult to verify, because the targets which cause those ambiguities are located outside the imaging swath and cannot be referenced without using another image.

5.2.5 Weak Signal Suppression Effect

The effect of weak signal suppression in the detected radar signal obtained through correlation processing corresponds to that of the response of a weak

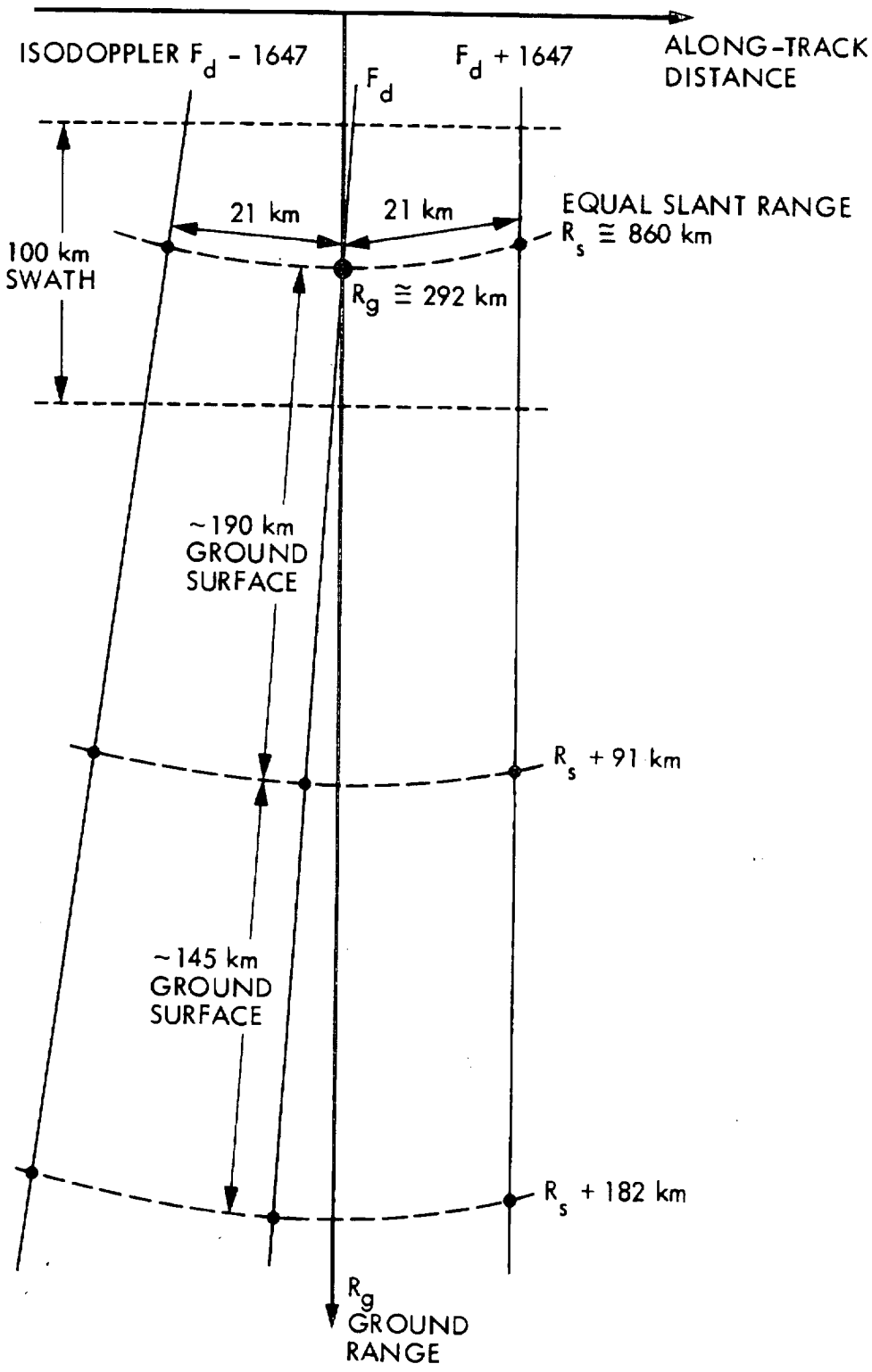

Figure 30. SEASAT SAR Range and Azimuth Ambiguity Function for the 1645 Hz Pulse Repetition Frequency

Figure 31. Azimuth Ambuiguity Induced False Features in Middle of Lake Pontchartrain, New Orleans

target which appears to be suppressed in the presence of a very bright target in its close vicinity. Further, the suppression is stonger as the distance between a weak target and the bright main target is reduced. This effect causes a nonlinear loss (more for weaker targets) in detectability due to saturation (due to limited dynamic range) in the uncorrelated radar signals. In addition to a possible saturation in the radar data acquisition system, signal saturation can also occur in IDP processing due to finite bit data quantization in two intermediate steps. One step is after the range correlation, where each of the complex data words is quantized into 16 bits with 8 bits for each real or imaginary component. The other step is after the azimuth forward Fourier transform. The spectral data of the 8,8 bits range correlated data are again quantized into the same number of integer bits. The gains of the range correlation and the azimuth forward transform (the latter is set to have a unit gain) are designed so that only a very small percentage of the data will be saturated (assuming there is no substantial saturation in the input data).

Revolution 1291 was found to have strong saturation in the digitally recorded raw data. The weak signal suppression effect is observed in the imagery processed from that revolution. An example is shown in Figure 32. This picture is an enlarged section of the image shown in Figure 11. The horizontal linear feature in the middle of the picture is the Santa Ana River. Freeways in this area are shown as major dark lines. The dark bands next to several bright features right above the Santa Ana River are oriented in the azimuth dimension, and are apparently due to the weak signal suppression effect. It is possible to conclude that this suppression is due to saturation in the input raw data, because the same area as viewed in another SEASAT revolution

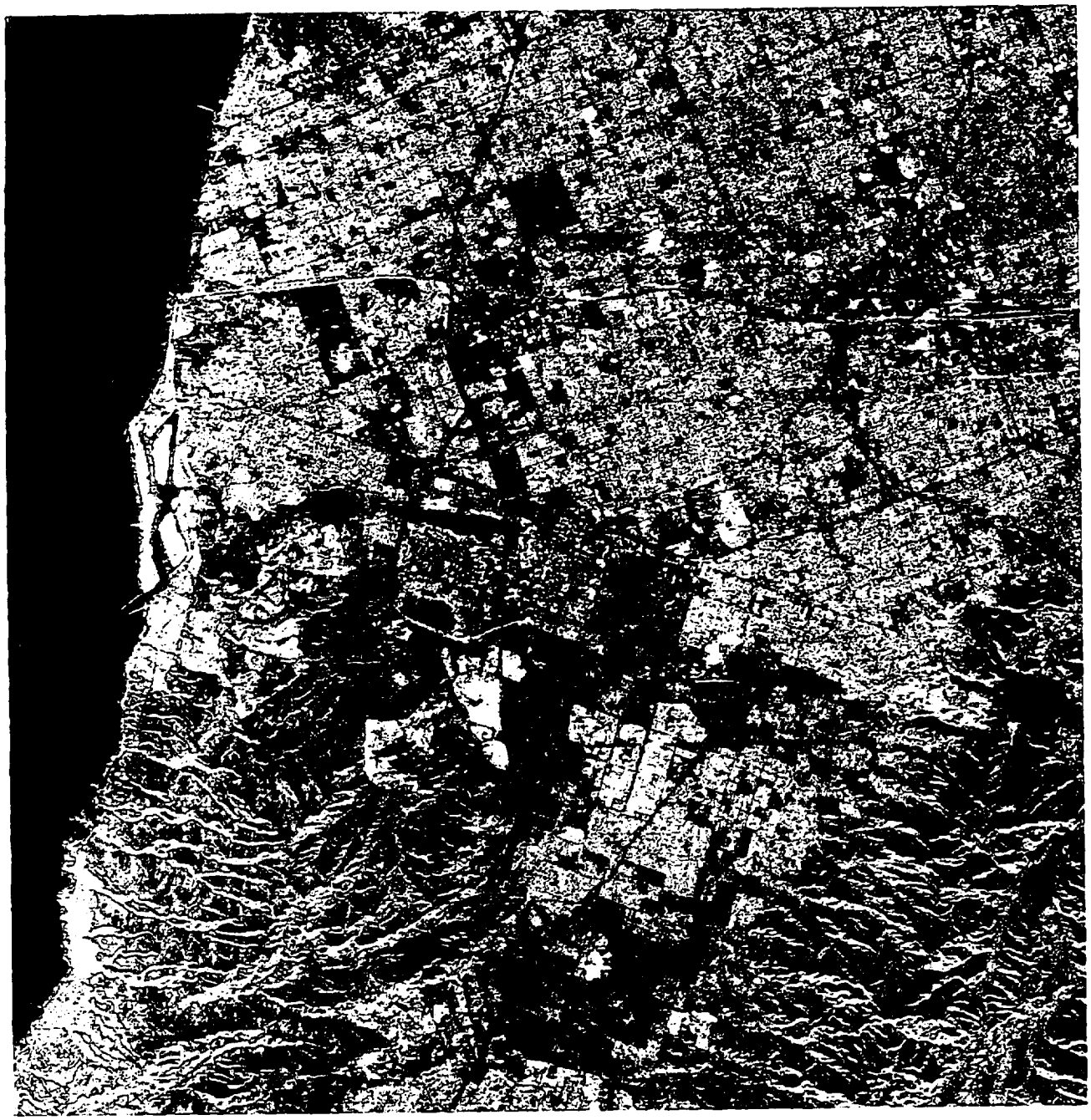

Figure 32. Azimuth Near Signal Suppression Effect Shown Near the Center of the Image

(Rev. 351) does not exhibit this weak signal suppression effect. It is also possible that a change in the SAR pass orientation (Revs. 351 and 1291 are of ascending and descending nodes, respectively) may change the apparent reflectivity of those bright target features (5.2.6), and therefore reduce the severity of the weak signal suppression effect. The IDP range and the azimuth correlation gains are 27 dB and 25 dB respectively. For the example shown in Figure 29, the suppression effect in azimuth indicates that the contrast in target reflectivity was much greater than 25 dB but was less than 52 dB. If the contrast becomes much greater than 52 dB, the suppression effect may become noticeable in both range and azimuth dimensions.

5.2.6 Target Reflectivity and Radar Aspect Angle

The apparent brightness of a target in SAR imaging depends not only on the target electromagnetic characteristics but also on the geometry of the target structure and the associated radar viewing angle. The latter factor may become very significant for an area with man-made structures where the radar targets or scatterers are geometrically oriented. An example is shown in Figure 33. A section of the image taken near the upper left corner of Figure 29 of revolution No. 1291, a descending node, is displayed in Figure 33 (a). The same area as seen in an imagery acquired during Rev. 351, an ascending node, is shown in Figure 33 (b). The change in brightness in the central area of the scene is primarily attributed to the different radar aspect angle. The satellite path of Rev. 351 was approximately parallel to the street blocks. The perpendicular faces of building structures to ground surface can induce a strong radar reflection very much similar to that which occurs over radar corner reflectors.

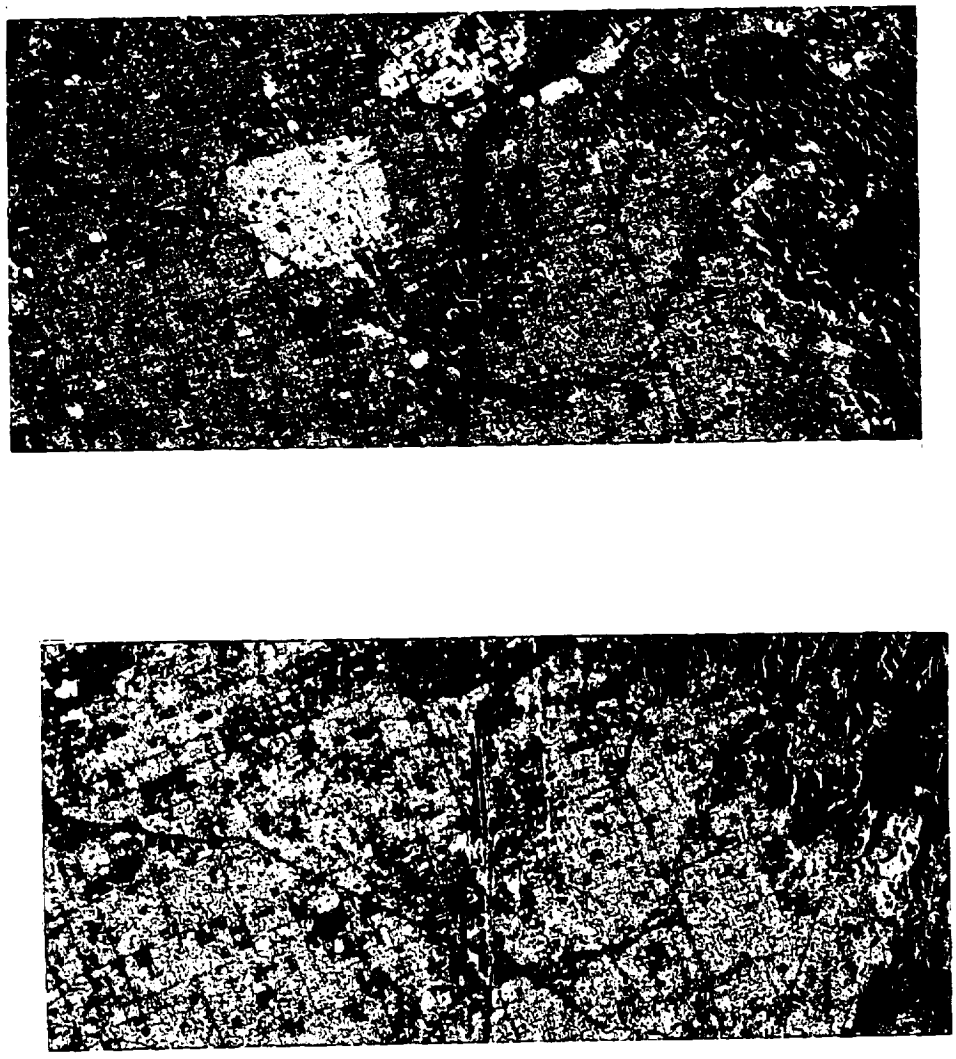

Figure 33. Effect of Radar Aspect Angle to the Apparent Target Reflectivity Over Cultural Targets

6. SUMMARY

This document provides a brief description of the Interim Digital SAR Processor and the characteristics of SEASAT SAR imagery. It is hoped that these engineering data are useful to the interpretation and analysis of the IDP produced SEASAT SAR imagery. Performance evalution of the IDP processed imagery is a continuing activity. It is also planned to modify the existing software in the near future to improve the sidelobe performance and to provide better radiometric calibration.

SEASAT SAR imagery in general demonstrates the concept and feasibility of microwave remote sensing from a spaceborne platform. The extended surface coverage, the near uniform radar angle of incidence, and the fact that the sensor operation is relatively free from perturbation, are indeed advantageous over conventional airborne SAR systems. Several phenomena which are often obscure in airborne SAR imagery are very clearly observed in SEASAT SAR images. With further efforts in the SEASAT SAR image analysis, a much better definition than that which is currently available is anticipated.

REFERENCES

1. R. Jordan, and B. Huneycutt, "SEASAT-A Synthetic Aperture Radar Performance," IEEE 1979 International Conference on Communication Record, Vol. 3, pp. 52.2.1-52.2.5, June 1979.

2. L. J. Cutrona, Synthetic Aperture Radar, Radar Handbook. M. I. Skolnik, ed. McGraw-Hill, New York, 1970, Chapter 23.

3. E. N. Leith, "Quasi-Holographic Techniques in the Microwave Region." IEEE Proc., Vol. 59, No. 9, pp. 1305-1318, Sept. 1971.

4. K. Tomiyasu, "Tutorial Review of Synthetic-Aperture Radar (SAR) with Applications to Imaging of the Ocean Surface." Proceedings of the IEEE, Vol. 66, No. 5, pp. 563-583, May 1978.

5. C. Wu, "A Digital System to Produce Imagery from SAR Data." Proceedings of the AIAA Systems Design Driven by Sensors Conference, Paper No. 76-968. Pasadena, California, October 1976.

6. C. Wu, " A Digital Fast Correlation Approach to Produce SEASAT SAR Imagery," Proceedings of the IEEE 1980 International Radar Conference, Washington, D. C., April 1980.

7. W. E. Brown, Jr., B. Holt, and M. Strommen, "Catalog of SEASAT Experiment Sites and Imaging Radar Requested (Preliminary Edition)", Jet Propulsion Laboratory, February 1979. (JPL internal document.)

8. S. S. Rifman and D. M. McKinnon, Evaluation of Digital Correction Techniques for ERTS Images, TRW Corporation Final Report, TRW 20634-6003-TU-00, NASA Goddard Space Flight Center, Greenbelt, Maryland, March 1974.

9. W. E. Brown, Jr., C. Elachi, R. L. Jordan, A. Laderman, and T. W. Thompson, Planetary Imaging Radar Study, pp. 4.15-4.23, TR701-145, Jet Propulsion Laboratory, Caltech, June, 1972 (JPL internal document).

10. R. L. Mitchell, "Models of Extended Targets and their Coherent Radar Images," IEEE Proc. Vol. 62, No. 6, pp. 754-758, June 1974.

11. N. George, "Speckle," Optics News, pp. 14-22, January 1976.

12. C. Wu, "A Derivation of the Statistical Characteristics of SAR Imagery Data," Proceedings of the Third European Space Agency SAR Image Quality Workshop, December 1980, Frascati, Italy.

13. R. G. Lipes and S. A. Butman, "Bandwidth Compression of Synthetic Aperture Radar Imagery By Quantization of Raw Radar Data," Proceedings of the SPIE, Vol. 119, pp. 107-114, August 1977.

14. C. Wu, Optimal Sampling and Quantization of Synthetic Aperture Radar Signals, JPL Publication 78-41, Jet Propulsion Laboratory, California Institute of Technology, Pasadena, California, 1978.

15. C. E. Cook and M. Bernfeld, Radar Signals, pp. 130-136, Academic Press, New York, London, 1967.

APPENDIX A

A Digital System To Produce Imagery From SAR Data

C. Wu

A DIGITAL APPROACH TO PRODUCE IMAGERY FROM SAR DATA*

C. Wu
Jet Propulsion Laboratory
California Institute of Technology
Pasadena, California, 91103

Abstract

This paper describes a digital processing algorithm and its associated system design for producing images from Synthetic Aperture Radar (SAR) data. The proposed system uses the Fast Fourier Transform (FFT) approach to perform the two-dimensional correlation process. The range migration problem, which is often a major obstacle to efficient processing, can be alleviated by approximating the locus of echoes from a point target by several linear segments. SAR data corresponding to each segment is correlated separately, and the results are coherently summed to produce full-resolution images. This processing approach exhibits greatly improved computation efficiency relative to conventional digital processing methods.

I. Introduction

It is known that for a given frequency the angular resolution capability of a radar system is directly determined by the aperture size of the radar antenna. The idea of the synthetic aperture radar (SAR)[1,2] is to use coherent phase information in an array of radar echoes to synthesize an effective antenna aperture which is much larger than the size of the physical antenna. This approach enables high spatial resolution radar images to be attained with practical size antenna.

In order to achieve the effective increase in aperture, the raw radar returns gathered go through processing to compress the dispersed response from a point target. Typically, the processing involves a correlation between the raw echo data and the response function of point target. Since the dimension of dispersion, i.e., the number of elements needed to be correlated to produce an image point, is usually large, digital SAR processing is often characterized by a requirement for a very large bulk memory to store the data to be correlated. In addition to this requirement, in most of the synthetic aperture radar applications, the data rate from the radar receiver is very high. To achieve real-time or near real-time processing, the speed of data processing in an electronic SAR processor must be very high to accommodate the high input data rate. The requirement of large bulk data storage and high data processing speed in a digital SAR processor make it important to properly design the memory management and processing system. In this paper we shall focus our attention to the methods for efficient processing of SAR data into images.

Generally speaking, in a correlation process the number of arithmetic operations is directly proportional to the number of elements in the reference function and the number of elements in the final image. It is clear that the processing efficiency (which is a factor in determining system throughput) is directly related to the number of arithmetic operations. If the computation speed of an arithmetic unit is a limiting factor, system throughput can be increased either by implementing more arithmetic logic units to allow parallel processing or by reducing the number of arithmetic operations per image element by using more efficient processing algorithms. The cost of processing associated with the former approach increases linearly with the amount of parallelism in the hardware. For the later approach, the throughput can be increased at no increase in cost. Special purpose hardware implementations may be appropriate for operational applications, and the optimum algorithm for such systems are influenced by available hardware technology. To support SAR research activities, it is more practical to accomplish processing in a general purpose computer. Thus it is important to develop efficient SAR processing algorithms for both special purpose hardware processors and for general purpose computers.

The two digital SAR processing approaches used presently to reduce raw data into images can be referred to as the time-domain correlation approach and the frequency domain FFT (fast fourier transform) approach. The idea of time-domain correlation is relatively straight forward. An image element is processed by a direct reference function multiplication and integration. The frequency domain FFT approach uses the FFT to transform echo signals into frequency spectra and then filtering is applied to these spectra. The basic assumption of FFT approach is that the impulse response function is linear and invariant over the data block to be processed. Under this assumption, the FFT approach does achieve the optimality in the number of arithmetic operations per each image element. However, there are several difficulties in applying the FFT processing approach to SAR data which exhibit excessive range curvature (wherein the locus of echoes from a point target deviates from its linear approximation by more than one range resolution element in a two-dimensional display of the SAR echo signals). This problem is serious in some planned satellite imaging radar applications, e.g., SEASAT-A. This paper reports the results of an effort to formulate a computationally efficient FFT approach which performs full synthetic aperture processing of SAR data containing significant range curvature.

In the following discussion, a brief description of the analytical background of FFT filtering

*This paper presents the results of one phase of research carried out at the Jet Propulsion Laboratory, California Institute of Technology, under Contract No. NAS7-100, sponsored by the National Aeronautics and Space Administration.

approach for SAR data processing will be given, and then the difficulty of efficiently applying the FFT approach for processing SAR data with significant range curvature will be discussed. Major emphasis is placed on rigorous description of the method for efficient SAR processing in conjuction with the correction for range curvature.

II. Digital Processing of SAR Data Using the FFT Approach

Assume a wave form $\cos(\omega t - \phi(t))$ is radiated from a synthetic aperture radar, where $\omega/2\pi$ is the frequency of the coherent carrier and $\phi(t)$ is the pulse coding form. A point target a distance r_1 from the aircraft returns the signal:

$$S(t) = \sigma \cos\left[\omega\left(t - \frac{2r_1}{c}\right) - \phi\left(t - \frac{2r_1}{c} - nT\right)\right] \quad (1)$$

where

σ is the radar cross section (reflectivity) of the target

c is the speed of light

and

T is the pulse repetition interval

Since the pulse repetition rate of an SAR is such that a point target on the surface is "interrogated" many times as it passes through the beamwidth of the radar antenna, the ensemble of returned echo signals can be assembled into a rectangular display with elapsed time (range, r) along one axis and along flight position (azimuth, x) along the other axis. The assembled returns from a point target is also two-dimensional. For a point target of unit reflectivity located at (x_o, r_o), the two-dimensional impulse response at baseband output can be written as

$$h(x - x_0, r - r_0) = \begin{cases} \exp j\left\{-\omega\frac{2r_1}{c} + \phi\left[\frac{2}{c}(r - r_0) - \frac{2}{c}(r_1 - r_0)\right]\right\} \\ \text{for } (x, r) \in R \\ 0 \\ \text{otherwise} \end{cases} \quad (2)$$

where

$$r_1 = \sqrt{r_0^2 + (x - x_0)^2} \quad (3)$$

R, the region of responsiveness, is determined by the pulse duration and the pattern of the antenna beam. Eq. 2 can also be expressed as

$$h(x, r) = h_1(x, r) \otimes h_2(x, r) \quad (4)$$

where " $\otimes$ " stands for convolution, and

$$h_1(x, r) = \begin{cases} \delta\left[r - \left(\sqrt{r_0^2 + x^2} - r_0\right)\right] \exp j\left(-\frac{2\omega}{c}\sqrt{r_0^2 + x^2}\right) \\ \text{for } (x, r) \in R_1 \\ 0 \\ \text{otherwise} \end{cases} \quad (5)$$

$$h_2(x, r) = \begin{cases} \delta(x) \exp j\,\phi\left(\frac{2r}{c}\right) & \text{for } (x, r) \in R_2 \\ 0 & \text{otherwise} \end{cases} \quad (6)$$

R_1, R_2 are the region of responsiveness for h_1 and h_2, respectively. The δ-function in h_1 and h_2 is Dirac's delta function. In terms of physical meanings, h_1 is the point target return corresponding to an "infinitesimally narrow" transmitted pulse, and h_2 has the waveform of the actual transmitted pulse.

Eqs. 2 to 6 summarized the response from an ideal point target. For an extended target, $\sigma(x, r)$, the response $f(x, r)$ can be written as:

$$f(x, r) = \sigma(x, r) \otimes h(x, r) \quad (7)$$

Substituting Eq. 4 into above, we have

$$f(x, r) = \sigma(x, r) \otimes \left[h_1(x, r) \otimes h_2(x, r)\right] \quad (8)$$

It can be shown that Eq. 8 has the following alternative form

$$f(x, r) = \left[\sigma(x, r) \otimes h_1(x, r)\right] \otimes h_2(x, r) \quad (9)$$

The above equation shows that the echo returns, $f(x, r)$, can be expressed as the original target field $\sigma(x, r)$ convolved sequentially with two impulse responses h_1 and h_2. It is therefore clear that the targets $\sigma(x, r)$ can be reconstructed by sequentially correlating the return signal $f(x, r)$ by the responses $h_2(x, r)$ and $h_1(x, r)$. Eq. 6 shows that $h_2(x, r)$ is one-dimensional (in the range direction) wave form identical to the transmitted pulses. Correlation with respect to h_2 thus is a conventional one-dimensional correlation operation with a linear fixed reference function. One can therefore use a FFT approach to perform the range correlation. The correlation with respect to $h_1(x, r)$ is generally referred to as the azimuth correlation. According to Eq. 5, the locus of $h_1(x, r)$ is a two-dimensional curve. The dispersion in the x-direction is determined by the radar antenna beam width or the size of the synthetic aperture. In the r-direction, the change is due to the varying of distance between target and sensor as defined by Eq. 5. Indeed, the locus of a point target (measured by the delta function and the range of x) represents a section of a hyperbolic curve as defined by Eq. 3.

In many imaging radar applications, the geometric factors are such that the locus can be satisfactorily approximated by a straight line. That is, the maximum deviation of the true locus from the straight line approximation does not exceed half of a range resolution element. In such cases, the correlation of $h_1(x, r)$ can be viewed as a one-dimensional correlation problem. The FFT approach can again be used if the size of the data block is selected such that the azimuth reference function $h_1(x, r)$ is approximately unchanged over the data block to be processed.

In the above discussion, we have shown that if the range curvature is insignificant, the SAR correlation process can be performed by two-sequential FFT correlation operations. A block diagram of such an approach is shown in Figure 1. The raw data are first range correlated to

compress the phase coded pulse into a much narrower pulse. The range processed data blocks are stored, and then retrieved along the direction of azimuth correlation. The transfer function of the azimuth filtering which is derived from $h_1(x, r)$ needs to be constantly updated for targets at different range r_0. This is because the wave form of the reference function $h_1(x, r)$ changes with respect to r_0. Because the azimuth reference function $h_1(x, r)$ is target range dependent, optimal processing requires range correlation be performed prior to the azimuth correlation. Otherwise the azimuth reference function is not unique for a given range r_0.

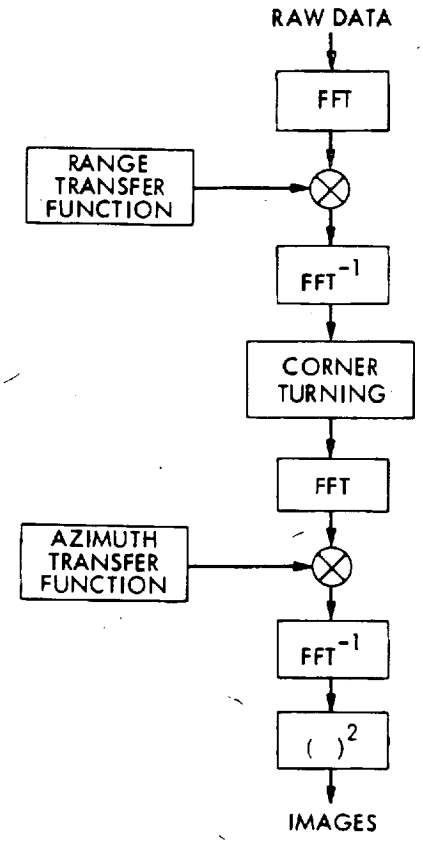

Figure 1. A System Block Diagram of the FFT SAR Data Processing Approach

Numerous SAR images have been produced from simulated and real SAR data using the FFT approach discussed in this section. Results are all very satisfactory.

III. FFT SAR Processing with Range Curvature Correction

In some SAR applications, there is a significant range curvature associated with the locus of the echoes from a point target. In such cases it is no longer adequate to use an approximate azimuth reference function which lies on a straight line. Consequently, one cannot use the one-dimensional FFT fast correlation approach for azimuth processing as discussed in the previous section. We shall now describe a more general approach to the SAR azimuth processing to accommodate the correction for range curvature. (The method previously described is a special case of this more general method.)

One approach to processing SAR data containing range curvature would be to use a two-dimensional FFT filtering, but this approach results in a high degree of computational complexity. An alternative approach proposed here involves using an ensemble of functions lying along parallel straight line segments to approximate the curved azimuth reference functions. The computational efficiency of this approach is nearly the same as that of the processing method discussed in the previous section for SAR data having an azimuth reference function which lies along a straight line. With the line segments approximation (or assuming that the azimuth response which has width in real cases is sampled along a set of parallel lines), the azimuth reference function, $h_1(x, r)$, can be represented as follows:

$$h_1(x, r) = \sum_{i=1}^{n} g_i(x, r) \tag{10}$$

where

$$g_i(x, r) \cong \begin{cases} \delta(r - d_i) \exp j\left(-\frac{2}{c}\sqrt{r_0^2 + x^2}\right) \\ a_i \le x < a_{i+1} \\ 0 \\ \text{otherwise} \end{cases} \tag{11}$$

The distance of the ith line segment from the line corresponding to r_0 is denoted by d_i. The azimuth coordinate corresponding to the start of the ith line segment is denoted by a_i. Fig. 2 graphically illustrates this method of obtaining an approximate azimuth reference function. Note the direction of the parallel lines can be chosen along the azimuth (perpendicular to range delay) direction or along a tilted direction to reduce the number of segments.

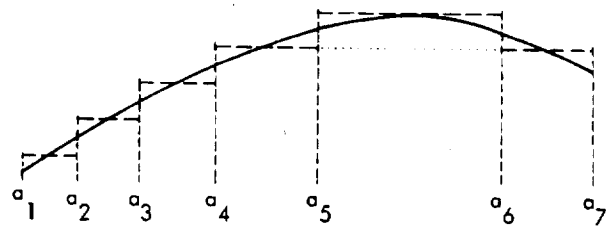

Figure 2. A Curved Range Delay History (Solid Curve) and its Piecewise Approximation (Dashed Lines)

Using Eq. 10, range correlated SAR data in sampled data domain can be represented as follows:

$$s(x, r) = \sigma(x, r) \otimes \sum_{i=1}^{n} g_i(x, r) \tag{12}$$

Assuming the approximated azimuth reference function in Eq. 11, the required azimuth processing can be accomplished with one-dimensional FFT processing. The theoretical background of this approach will be discussed in the following paragraphs.

For a constant r_0, the fourier transform of Eq. 12 gives

$$S(u, v) = \Omega(u, v) \cdot \left[\sum_{i=1}^{n} G_i(u, v) \right] \qquad (13)$$

The symbols S, Ω, and G_i represent the transformations of functions s, σ, and g_i, respectively, and u, v represent the variables in the transformed domain.

Eq. 13 implies that

$$\Omega(u, v) = S(u, v) \cdot \frac{\sum_{i=1}^{n} G_i^{*}(u, v)}{\left| \sum_{i=1}^{r} G_i(u, v) \right|^2} \qquad (14)$$

where "*" denotes complex conjugate. The Fourier transform of $g_i(x, r)$ according to Eq. 11 is

$$G_i(u, v) = h_i(u) \exp(jd_i v) \qquad (15)$$

where $h_i(u)$ is the Fourier transform of the exponential factor of g_i, which depends on variable x only. A close approximation of $h_i(u)$ can be derived by using the fact that the distance from target to sensor is normally much greater than the size of the synthetic aperture. This implies that distance r_1 of Eq. 3 can be approximated by:

$$r_1 \cong r_0 + \frac{(x - x_0)^2}{2r_0} \quad \text{if } r_0 \gg |x - x_0| \qquad (16)$$

An approximate expression for $h_i(u)$ can therefore be written as follows:

$$h_i(u) \cong \frac{1}{\sqrt{2\pi}} \int_{a_i}^{a_{i+1}} \exp j\left[-\frac{2\omega}{c} r_0 + \frac{x^2}{2r_0} \right] \exp(jux)\, dx$$

$$= \frac{\psi}{\sqrt{2\pi}} \exp j\left(\frac{cr_0}{4} u^2 \right) I_i(u) \qquad (17)$$

where

$\psi \left(= \exp j\left(-\frac{2\omega}{c} r_0 \right) \right)$ is a constant phase factor, and

$$I_i(u) = \int_{y_i}^{y_{i+1}} \exp\left(-j \frac{\pi}{2} y^2\right) dy$$

where

$$y_i = \sqrt{\frac{2\omega}{\pi c r_0}} \left(a_i - \frac{cr_0}{2\omega} u \right) \qquad (18)$$

The integral $I_i(u)$ shown above is a complex Fresnel integral. The magnitude of I_i can be approximated by the method of "Cornu's Spiral"[3]. According to Eq. 17, the magnitude of $h_i(u)$ is proportional to that of $I_i(u)$. Fig. 3 contains an approximate characterization of the magnitude of $h_i(u)$ with respect to u. Each $h_i(u)$ is shown to occupy a distinct frequency band in the transformed domain. This can also be explained by the fact that the phase of $h_1(x, r)$ with r_1 approximated by Eq. 16 resembles the phase of a linear FM chirp wave form; and there is a unique correspondence between each time interval in a linear frequency sweep and a frequency band in the sweep bandwidth.

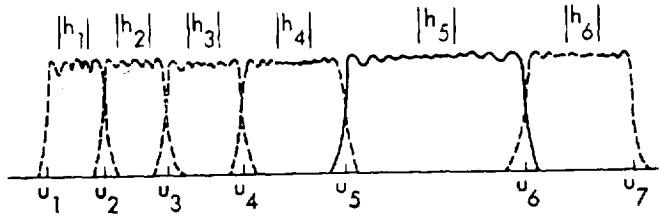

Figure 3. Amplitude Spectra of Segmented Azimuth Reference Function

When the above results are applied to Eq. 15, it is clear that $G_i(u, v)$ also exhibits bandpass characteristics. The amplitudes of $G_i(u, v)$ are approximately equal in the corresponding bands, thus the denominator of Eq. 14 is nearly constant throughout the total bandwidth of the azimuth response. We will use K to denote the value of the denominator in Eq. 14. Then, substituting Eq. 15, into Eq. 14, we have:

$$\Omega(u, v) = \frac{1}{K} \sum_{i=1}^{n} S(u, v)\, h_i^{*}(u) \exp(-j\, d_i v) \qquad (19)$$

Inverse Fourier transform of the above equation with respect to v yields:

$$\Omega'(u, r) = \frac{1}{K} \sum_{i=1}^{n} S'(u, r)\, h_i^{*}(u)\, \delta(r - d_i) \qquad (20)$$

The quantity $\Omega'(u, r)$ is the filtered azimuth spectrum. An SAR image will be formed by an inverse transform of $\Omega'(u, r)$ with respect to u.

For a fixed r in Eq. 20, the filtered line spectrum is a superposition of a number of filtered segments of line spectra. The range location of each segment relative to r_0 is specified by the value of d_i. In processing a line of image, the superposition of spectral bands can be efficiently implemented by a delay and registration operation. The method is described as follows: After range processing (if the radiated pulse is coded), each azimuth line is transformed into frequency domain. The line spectrum is subdivided into a number of bands each corresponds to the spectrum band of $g_i(x, r)$. The first several lines are transformed to enable a complete composite spectral line to be formed by superpositioning spectral bands from different lines according to the delay specified by the value d_i. The composite spectrum is then multiplied by the azimuth transfer function $h_i^{*}(u)$, inversely transformed, and filtered to form a line of the SAR image. Each additional azimuth line transformation enables formation and processing of the composite spectrum corresponding to the next line of the image. This process will continue until the whole block of data is processed into image. A diagram of this processing approach is shown in Fig. 4. The azimuth locus in Fig. 2 is used in this example. It is shown that the composite spectrum of an image line is obtained by assembling the appropriate segments from the spectra of several azimuth lines. To accommodate the

range dependent nature of the azimuth response function, the values of a_i and the azimuth reference function must be periodically updated when there is a significant change in range r_0.

If the input radar returns are contaminated by noise, various filtering functions, such as the least mean square error filter, minimum SNR filter, etc., can be used to optimize the quality of the processed image. It is also clear that image distortion associated with this particular approach can be measured by the amount of overlap in the spectra segments shown in Fig. 3. Increase the number of segments in azimuth reference function results in the increase of spectrum overlap. Therefore, it is very much desirable to choose a direction for azimuth processing (direction of the line segments) which minimizes the number of line segments in approximating azimuth reference functions.

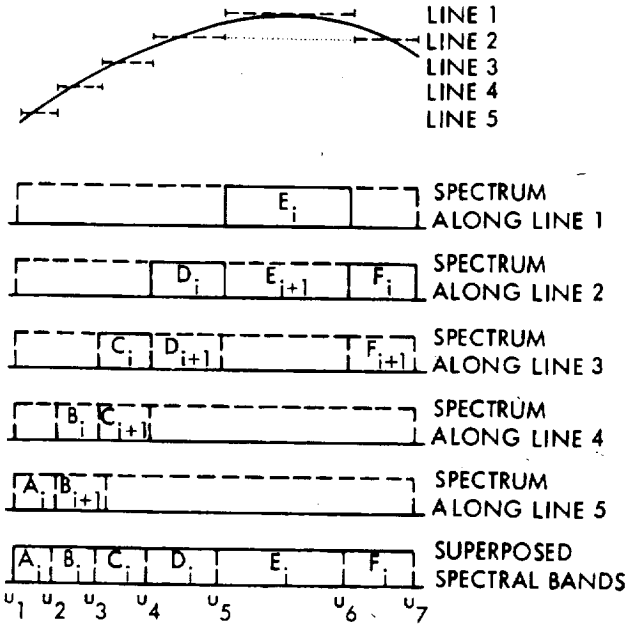

Figure 4. Delay and Coherent Superposition of SAR Azimuth Spectral Bands

Some experimental results are described in this paragraph. The inphase components of two simulated azimuth responses of a point target are shown in Fig. 5(a) and 5(b). The response in Fig. 5(a) lies along a straight horizontal line, whereas the curvature of the azimuth response in Fig. 5(b) spans four range resolution elements. Fig. 5(c) and 5(d) show the images of a point target which were reconstructed from the signals associated with Fig. 5(a) and 5(b), respectively, using the filtering method discussed in Section II; that is, using an azimuth reference function which lies along a single straight line. Because correction for range curvature is not applied, the degradation of resolution is clearly observed in the image of Fig. 5(d). Fig. 5(e) shows the reconstructed image produced from the signal in Fig. 5(b) using the method described in this section. By comparing the reconstructed point images, it is clear that the pulse width in Fig. 5(e) which is associated with the process with range curvature correction is much narrower than that of the image in Fig. 5(d). It is also noted that the image in Fig. 5(e) is nearly identical to the image in Fig. 5(c). This demonstrates the validity of the proposed SAR processing method using the FFT filtering approach for applications involving range curvature.

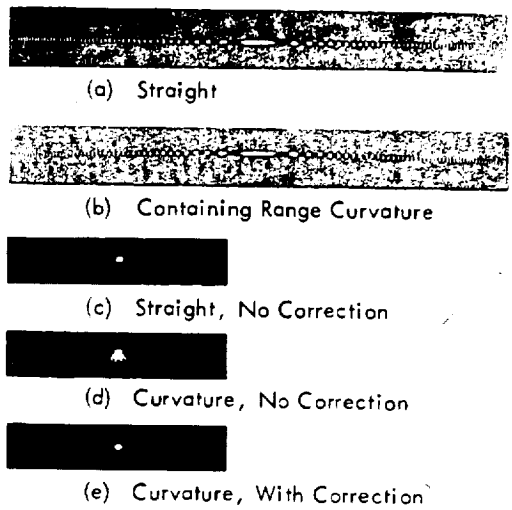

Figure 5. Simulated SAR Azimuth Responses and Reconstructed Images

IV. Conclusion

The method for digital processing of SAR signals into images discussed in this paper is shown to be a valid processing method both analytically and experimentally. Because the FFT processing approach is computationally efficient, this method can be very useful in applications where arithmetic computation speed is a significant factor in determining the cost of accomplishing timely processing of SAR data. Future electronic processing techniques are likely to be substantially influenced by advances in electronic device technology. In the near term, the proposed method provides an attractive approach for digital SAR processing using available digital electronic technology.

Acknowledgement

The author wishes to thank R.G. Piereson for his many thoughtful suggestions made in the course of this work. He also wishes to thank A.J. Spear for his encouragement.

Reference

1) E.N. Leith, "Quasi-Holographic Techniques in the Microwave Region," IEEE Proc., Vol. 59, No. 9, pp. 1305-1318, Sept. 1971.

2) R.O. Harger, Synthetic Aperture Radar Systems, Theory and Design. New York: Academic Press, 1970.

3) F.A. Jenkins and H.E. White, Fundamentals of Optics, Chapter 18, McGraw Hill, New York, 1957.

APPENDIX B

A Derivation of the Statistical Characteristics of SAR Imagery Data

C. Wu

A DERIVATION OF THE STATISTICAL CHARACTERISTICS OF SAR IMAGERY DATA*

C. Wu

Jet Propulsion Laboratory
4800 Oak Grove Drive
Pasadena, California 91109, U.S.A.

ABSTRACT

SAR imagery contains speckle noise as a result of coherent interference of radar echo and surface scatterers. This speckle effect must be properly treated in analyzing SAR image quality and image processing techniques. This paper, based on the Rayleigh scattering model, derives statistics of SAR sensed measurement and their relationships to the surface mean power reflectivity. These derived quantities are useful in areas such as SAR calibration and image processing.

1. INTRODUCTION

Synthetic Aperture Radar (SAR) is a coherent sensing device. Images gathered by a SAR exhibit extraneous granularity as a result of interference between the coherent electromagnetic wave transmitted by the radar and the scatterers on the target surface. Such granularity also exists in a laser illuminated scene and is commonly referred to as speckle [1].

The speckle variation effect presents several difficulties in utilizing SAR image data. The prominent difficulties are the large variance in the radiometric response of a SAR picture element (pixel), and the altered spatial correlation property relative to that of a scene obtained by an incoherent sensor. This paper addresses several basic statistical properties of the speckle effect and the associated spatial correlation of SAR image data. In the following sections, a review of the Rayleigh speckle model will be given. The Rayleigh statistics will then be used to derive the correlation and spectral measures for SAR image data. Application of those derived statistics to SAR radiometric measures and image processing will also be discussed.

2. RAYLEIGH SPECKLE STATISTICS

SAR processed echo measurements contain both the target amplitude and phase responses before the intensity detection procedure. To analyze the statistical property of the SAR measurement for a pixel, we begin with a derivation of the relationship between the SAR measurements and surface reflectivity.

Assuming unity radar illumination at target surface, the echo return from a point target with amplitude reflectance σ_0 can be expressed as:

$$e_c(x,r) = \sigma_0(x,r)e^{j\phi_0(x,r)} \qquad (1)$$

where (x,r) denote spatial coordinates in azimuth (along-track) and range (cross-track), respectively, for the location of the point. ϕ_0 is the phase delay which is a function of radar wavelength and path distance only and is independent of σ_0. The target surface under SAR interrogation can be considered as a continum of infinitesimally small point scatterers. The radar system response to a point at (x,r) extends a finite distance over (x,r) as a consequence of the limited transmitter and Doppler bandwidths. Let us denote the system response function as U(x,r). In many published articles [2], U(x,r) takes the sinx/x waveform in both range and azimuth direction as a result of compressing a signal with quadratic phase history. The SAR processed echo measurement is a linear superposition of responses from all the infinitesimally small scatterers. An expression for a SAR measurement can be written as:

$$A(x,r) = \iint \sigma_0(y,z)e^{j\phi_0(y,z)}u(y-x,z-r)\,dydz + n_t = \iint u(y,z)\sigma_0(y+x,z+r)\,e^{j\phi_0(y+x,z+r)}\,dydz + n_t \qquad (2)$$

where n_t denotes the random noise component introduced by the radar system.

The exact SAR response function is another topic. Indeed, one can combine U and $e^{j\Phi 0}$ as the real SAR response, and leave σ_0 as the only variable which relates to target surface. The 1/2 power value of U(x,r) which is commonly referred to as SAR resolution is generally much bigger than radar wavelength. For this reason, the phase factor ϕ_0 changes over many cycles in U(x,r), and hence the sign of the real and imaginary parts of this complex phase factor also alter many times in U(x,r). The expected value of the real and imaginary components of A(x,r) are, therefore, zero.

*This paper presents the results of one phase of research carried out at the Jet Propulsion Laboratory, California Institute of Technology, under Contract No. NAS7-100, sponsored by the National Aeronautics and Space Administration.

The central limit theorem which applies to the summation of large number of independent variables of the same distribution also suggests that the values of the real and imaginary components of A(x,r) are of Gaussian distribution. These two components share equal variance, σ_a^2, which is one-half of the mean power of A(x,r), i.e.

$$\sigma_a^2(x,r) = \frac{1}{2} E[|A(x,r)|^2]$$

$$= \frac{1}{2} [\iint U^2(y,z)\sigma_0^2(y+x, z+r) \, dydz + N_t] \quad (3)$$

where N_t denotes the mean noise power. Reduction of the quadriple integration to double integration is possible because of the independent phase factors which result in a Dirac δ-function during integration. The integral above represents the sum of power reflectivity σ_0^2 weighted by the square of SAR system response U(x,r). We denote P_0 to be the integral of power reflectivity, i.e.

$$P_0(x,r) = \iint U^2(y,z)\sigma_0^2(y+x, z+r)dydz \quad (4)$$

The mean and variance of the real and imaginary components of A(x,r), which are represented by a_1 and a_2 respectively, are explicity expressed as:

$$m_a = E[a_1] = E[a_2] = 0 \quad (5a)$$

$$\sigma_a^2 = V[a_1] = V[a_2] = \frac{1}{2}(P_0(x,r) + N_t) \quad (5b)$$

Note that a_1 and a_2 are statistically uncorrelated quantities because $\cos\phi_0$ and $\sin\phi_0$ are uncorrelated for a random ϕ_0 uniformly distributed over $(0,2\pi)$. The joint Gaussian density function for a_1 and a_2 is:

$$f(a_1,a_2) = \frac{1}{2\pi\sigma_a^2} e^{-(a_1^2+a_2^2)/2\sigma_a^2} \quad (6)$$

The probability densities of two derived quanties:

$$a = \sqrt{a_1^2 + a_2^2}$$

$$p = a_1^2 + a_2^2$$

which are the amplitude and intensity of A(x,r), respectively, are [3]:

$$f_A(a) = \frac{a}{\sigma_a^2} e^{-\frac{a^2}{2\sigma_a^2}} \quad \text{for } a \geq 0 \quad (7a)$$

$$f_p(p) = \frac{1}{2\sigma_a^2} e^{-\frac{p}{2\sigma_a^2}} \quad \text{for } p \geq 0 \quad (7b)$$

These two density functions are of Rayleigh and exponential distributions, respectively. Substituting Eq. 5b into above, the amplitude and intensity distributions of a SAR measurement in terms of the target power reflectivity P_0 of Eq. 4 are:

$$f_A(a) = \frac{2a}{P_0+N_t} e^{-\frac{a^2}{P_0+N_t}} \quad (8a)$$

$$f_p(p) = \frac{1}{P_0+N_t} e^{-\frac{p}{P_0+N_t}} \quad (8b)$$

The measurement A(x,r) or its power P(x,r) can also be written as:

$$A(x,r) = \alpha P_0^{1/2}(x,r)e^{j\phi_0} + n_t \quad (9)$$

$$P(x,r) = \gamma(P_0(x,r) + N_t) \quad (10)$$

where α, γ are two random variables of distributions similar to Eq. 7 with $\sigma_a^2 = 1/2$, i.e.

$$f(\alpha) = 2\alpha e^{-\alpha^2} \quad (11a)$$

$$f(\gamma) = e^{-\gamma} \quad (11b)$$

and the moments of α, γ are [3]:

$$E[\alpha^n] = \begin{cases} \sqrt{\frac{\pi}{2}} \, 1 \cdot 3 \cdot \ldots \cdot n(\frac{1}{2})^{n/2} & \text{for n odd} \\ k! & \text{for } n = 2K \end{cases} \quad (12)$$

and

$$E[\gamma^n] = n! \quad (13)$$

3. THE STATISTICS AND CORRELATION PROPERTIES OF SAR IMAGE DATA

Eq. 10 clearly indicates that the target power reflectivity can be estimated linearly from the SAR measurement P(x,r). The exponentially distributed random variable γ causes uncertainty in the estimate (where we assume the mean system noise power N_t is known). We provide a generalized expression for the expected value of the n-th power of P(x,r) using Eqs. 10 and 13:

$$E[P^n(x,r)] = n!(P_0(x,r) + N_t)^n \quad (14)$$

Based on this equation the mean and variance as well as higher order quantities of measurement P(x,r) are readily obtained. These quantities can be used to derive the estimation accuracy as a function of sample size, number of looks, and expected pixel power $P_0(x,r)$.

The auto-correlation of P(x,r) is expressed:

$$R_{P^n}(\Delta x,\Delta r) = E[P^n(x,r) \cdot P^n(x+\Delta x, r+\Delta r)] \quad (15)$$

The statistic at $\Delta x=0$ and $\Delta r=0$ reduces to the value given in Eq. 14. For Δx and Δr greater than the spatial resolution defined by $U(x,r)$, the factors are approximately independent, i.e.

$$R_{P^n}(\Delta x,\Delta r) = (n!)^2 E[(P_q(x,r) + N_t)^n (P_0(x+x,\Delta r+\Delta r) + N_t)^n] \quad (16)$$

The expected value for the quantity within the square bracket can be evaluated based on the correlation property of $P_0(x,r)$ which resembles the reflectivity scene obtained by an incoherent sensor. For n=1, the correlation reduces to:

$$R_P(\Delta x,\Delta r) = R_{P_0}(\Delta x,\Delta r) + 2\bar{P}_0 N_t + N_t^2 \quad (17)$$

where $\bar{P}_0$ is the mean scene reflectivity. The relationship between auto-correlation of the coherently sensed scene and the corresponding value of an incoherently sensed scene is given above. Estimation of R_{P_0} from R_P is possible since $\bar{P}_0$ and N_t are quantities that can be obtained by knowing the general signal to noise ratio of the SAR system.

The cross-correlation of two SAR image sets is also examined here. Let $P_1(x,r)$ and $P_2(x,r)$ denote two data sets. Since two independently measured data sets have independent speckle variation, the cross-correlation is simply:

$$R_{P_1^n P_2^n}(\Delta x,\Delta r) = (n!)^2 R_{P_{01}P_{02}}(\Delta x,\Delta r) \quad (18)$$

4. SPECTRAL CHARACTERISTICS OF SAR IMAGE

4.1 Spectral components of SAR imagery

The γ factor in Eq. 11b varies from pixel to pixel, hence the power measure can be written as:

$$P(x,r) = \gamma(x,r)(P_0(x,r) + N_t) \quad (19)$$

Fourier transform of (19) results in the following expression:

$$S(u,v) = \frac{1}{B^2} S_\gamma(u,v) \otimes [S_0(u,v) + N_t B^2 \delta(u,v)]$$
$$= \frac{1}{B^2} S_\gamma(u,v) \otimes S_0(u,v) + N_t S_\gamma(u,v) \quad (20)$$

where $\otimes$ stands for convolution and S, S_γ, S_0 represent the spectra of P, γ, and P_0, respectively, and B^2 is the size of the spectral domain. Define:

$$\gamma = 1 + t \quad (21)$$

Eq. 12 implies

$$E[t] = 1 \quad (22a)$$

$$V[t] = 1 \quad (22b)$$

The spectrum of $\gamma(x,r)$ therefore is:

$$S_\gamma(u,v) = B^2\delta(u,v) + S_t(u,v) \quad (23)$$

where S_t is the white spectrum of $t(x,r)$ of Eq. 21. Replacing Eq. 23 into Eq. 20, we obtain

$$S(u,v) = S_0(u,v) + \frac{1}{B^2} S_0(u,v) \otimes S_t(u,v) + B^2 N_t \delta(u,v) + N_t S_t(u,v) \quad (24)$$

Due to the fact that spectrum $S_t(u,v)$ is white Gaussian, the convolution in Eq. 24 also results in a white spectrum $N_\gamma(u,v)$. The four components of S(u,v) can be expressed as follows:

$$S(u,v) = S_0(u,v) + N_\gamma(u,v) + B^2 N_t \delta(u,v) + N_t S_t(u,v) \quad (25)$$

S_0 is the spectrum of the scene reflectivity. N_γ is the white noise spectrum due to speckle variation. $B^2N_t\delta(u,v)$ corresponds to the spectrum of the unity biased mean floor of the thermal noise power N_t. $N_tS_t(u,v)$ is the spectrum due to the variation of thermal noise. Based on the variance of t as given by Eq. 22, the following relationships are valid:

$$\iint |S_0(u,v)|^2 du\, dv = \iint |N_\gamma(u,v)|^2 du\, dv \quad (26)$$

and

$$B^2 N_t^2 = \iint N_t^2 |S_t(u,v)|^2 du\, dv \quad (27)$$

The above equations indicate that spectral energy is divided equally over the original spectra, S_0 and $B^2N_t\delta(u,v)$, and the parts due to speckle variation N_γ and N_tS_t. A graphic representation of the expected energy of those four components is given in Fig. 1. The level N_γ and the delta-function B^2N_t components are introduced due to the speckle effect to the scene $P_0(x,r)$ and the positive noise floor N_t in a detected image. Given the signal to thermal noise of the SAR system, the partitioning of these levels are readily obtained. The sum of N_γ and N_tS_t amounts to half of the total power in the SAR image data.

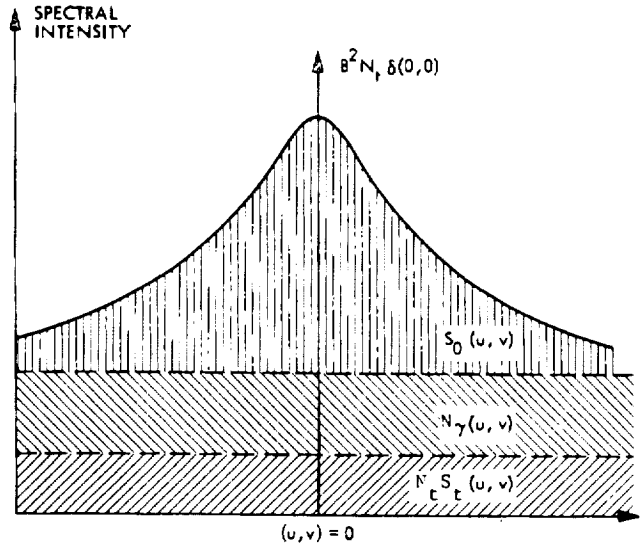

Figure 1. Four Major Components in a SAR Image Spectrum

4.2 Spectral filtering of SAR imagery

The partitioning of spectral components of a SAR image described above provides a quantatitive basis to formulate effective spectral filtering techniques for SAR image enhancement. Applying the well known least-mean-square filter:

$$H(u,v) = \frac{\bar{S}_0(u,v)}{\bar{S}(u,v)} = \frac{\bar{S}_0(u,v)}{\bar{S}_0(u,v) + \bar{N}(u,v)} \quad (28)$$

where a bar indicates the mean of the quantities it designates. The filtered spectrum is:

$$S(u,v) = H(u,v) \cdot S(u,v) \quad (29)$$

For SAR image, the composit noise spectrum consists of the last three terms of the right hand side of equation (25). These levels can be estimated by knowing the system signal-to-noise level as mentioned in the previous subsection.

4.3 Simulation results

Simulated SAR imagery of ocean wave scenes were used to study the scene spectra and image restoration. They are shown in Fig. 2. The top three images are simulated wave patterns of three different wave spectral characteristics. The coherency of the periodic wave structure decreases from left to right. Speckle effect was applied to these images with a multiplicative factor which corresponds to the mean of four independent exponentially distributed data samples. They are shown in the second row of the figure. This four sample averaging of the speckle factor described in Section II simulates four-look SAR image data. Pictures in Fig. 3 are the power spectra of the images shown in Fig. 2. Note that the speckle effect produces a uniform and noisy level over the entire two-dimensional wave spectra. The top three pictures of Fig. 4 are the filtered wave scene obtained by applying the least-mean-square filtering to the speckly images in Fig. 2. The intensity level is lower than that of the original images since the filters as specified by Eq. 2 will reduce the filtered image power by a factor of at least 2. Another filtering approach was experimented with a threshold to the scene spectrum. All spectral data with magnitude greater than a defined threshold will be retained and the rest will be set to zero. The purpose of this threshold is to keep only those dominant data which correspond to the scene spectral response as shown on Fig. 1. The threshold filtered wave data are shown in the lower part of Fig. 4. Results of threshold filtering appear inferior to that obtained by the least-square-filtering approach.

5. CONCLUSION

The statistics of SAR image data derived in this paper provide the needed mathematical basis to estimate SAR target reflectivity and scene spectral responses. A number of SAR multiple-looks is necessary to reduce the variation due to speckle effect. The formulas described herein enable the estimation of size of sample or number of looks required to estimate those quantities of interest within certain specified accuracy.

6. REFERENCES

[1] J.C. Dainty, "An Introduction to Speckle," Proceedings of the Society of Photo-Optical Instrumentation Engineers, Vol. 243, Paper 243-01, July 1980.

[2] E. N. Leith, "Quasi-Holographic Techniques in the Microwave Region," IEEE Proceedings, Vol. 59, No. 9, pp 1305-1318, Sept. 1971.

[3] A. Papoulis, Probability, Random Variables, and Stochastic Process, pp 194-195. McGraw-Hill, 1965.

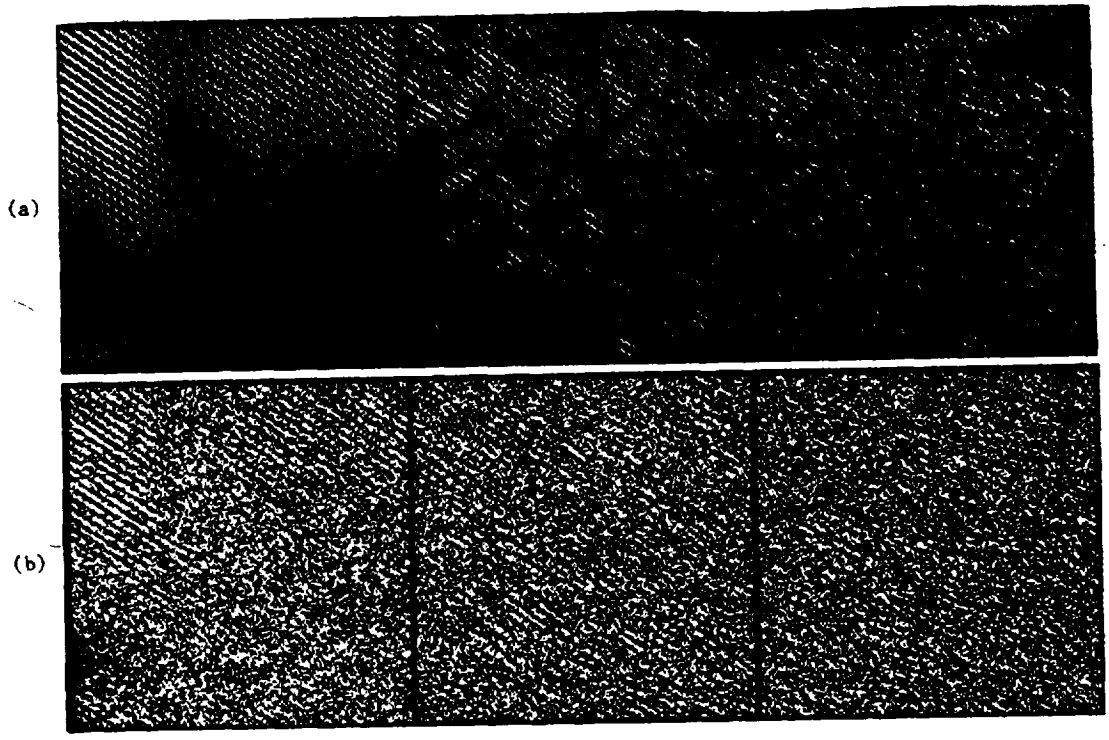

Figure 2. (a) Simulated Oceanwave Reflectivity Patterns
(b) Simulated Four-Look SAR Imagery

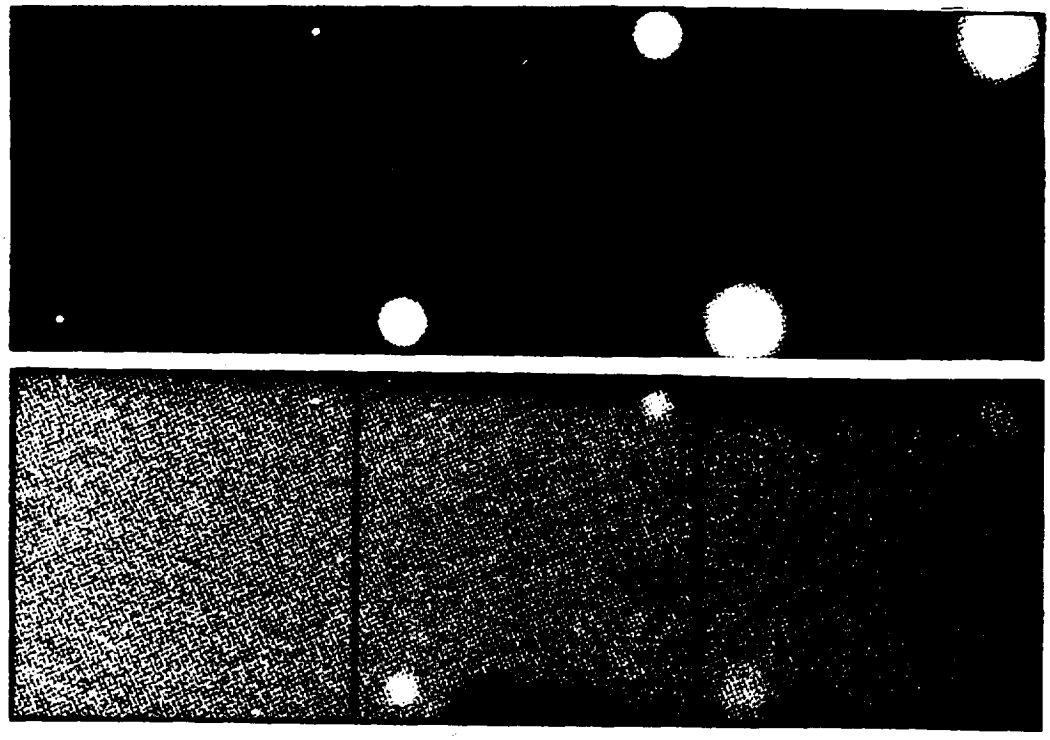

Figure 3. (a) Spectra of the Ocean Reflectivity Patterns
(b) Spectra of the Simulated Four-Look SAR Imagery

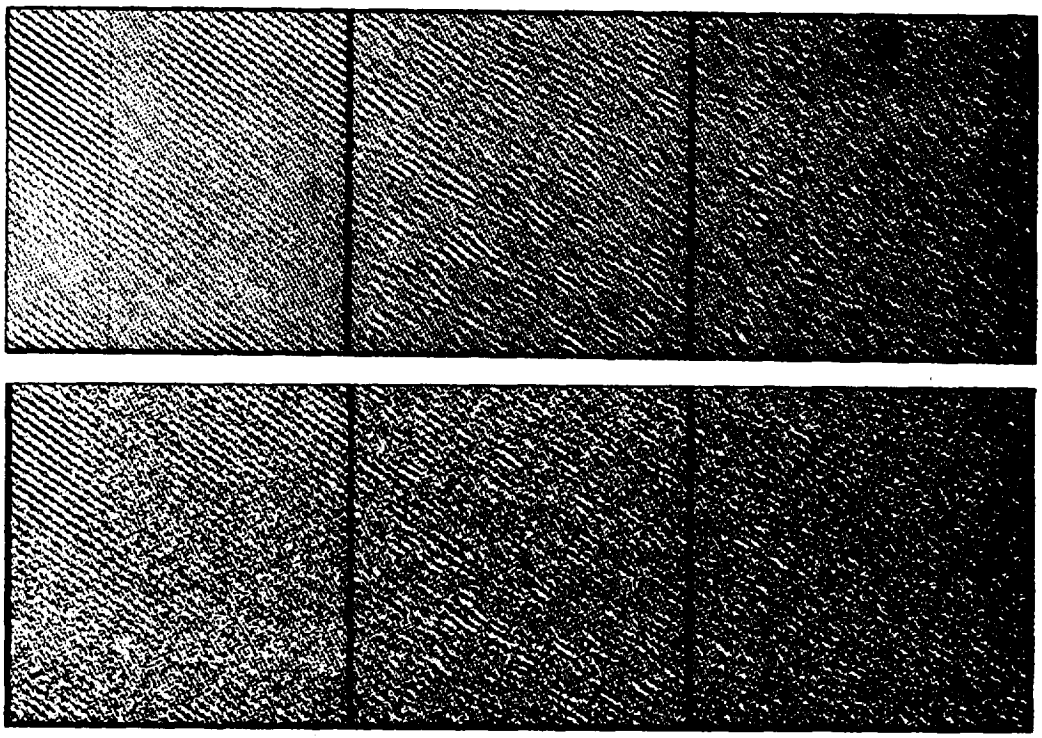

Figure 4. (a) Least-Mean-Square Filtered Four-Look SAR Imagery
(b) Threshold Filtered Four-Look SAR Imagery

APPENDIX C

SEASAT SAR Radiometric Calibration Considerations

B. Huneycutt

C.1 INTRODUCTION

There are many system gain variations and non-linearities which introduce significant uncertainties into the amplitude calibration of the SEASAT SAR system. Those calibration error sources which are not controllable by the SAR system, such as atmospheric and ionospheric effects and Faraday rotation effects, will not be addressed herein. Those calibration error sources which are controllable by the SAR system are best described by considering the various elements in the SAR system as shown in Figure C1. Only those elements in the SAR system up to the recording of the SAR data upon the high density data record (HDDR) are considered in this report. These calibration considerations are common to both digital and optical processing of the SAR data, both of which access the HDDR data.

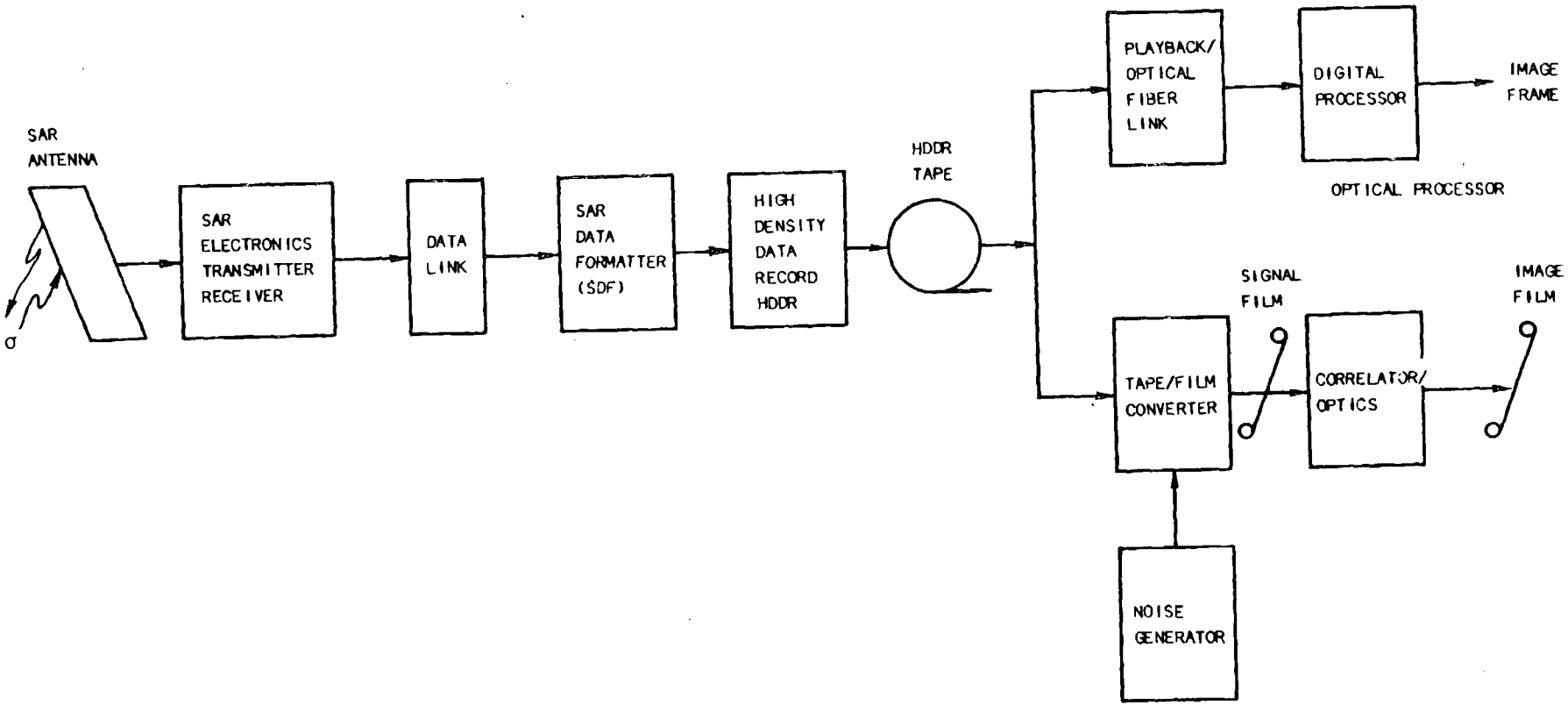

Figure C1. Radiometric Calibration System Elements

C.2 CALIBRATION CONSIDERATIONS OF THE SAR TRANSMITTER AND ANTENNA POINTING

To obtain amplitude calibration of the SEASAT SAR system, the system gain variations caused by the SAR transmitter and the SAR antenna pointing must be considered. For instance, the peak output power of the SAR transmitter FM pulse decreases typically by 0.6 dB with increasing transmitter temperature over the nominal 10 minute SEASAT SAR pass.

The L-band signal is radiated by the SAR planar array antenna; for a uniform, extended target, the return echo is amplitude modulated in the range direction by the antenna gain pattern, the slant range differential across the antenna beamwidth, and the surface scattering properties at the varying incident angle. Although the record window was intended to be centered about the boresight return, the 300 sec record window was actually systematically mispositioned slightly off-center by 40 to 60 μsec. Since the gain pattern falls sharply beyond the 3 dB beamwidth, small attitude or boresight pointing error may cause the more pronounced gain variations in that portion of the record window to deviate pronouncedly from the expected values. Figure C2 shows the two-way antenna gain variation caused by a location uncertainty of 5 μsec within the record window, assuming the record window is centered about the boresight return. The uncertainties due to the variation in the antenna gain pattern, variations in amplitude over the 20 MHz frequency band, variations of antenna gain with temperature and flatness, and variations due to roll angle are expected to be about $\pm$ 1.5 dB.

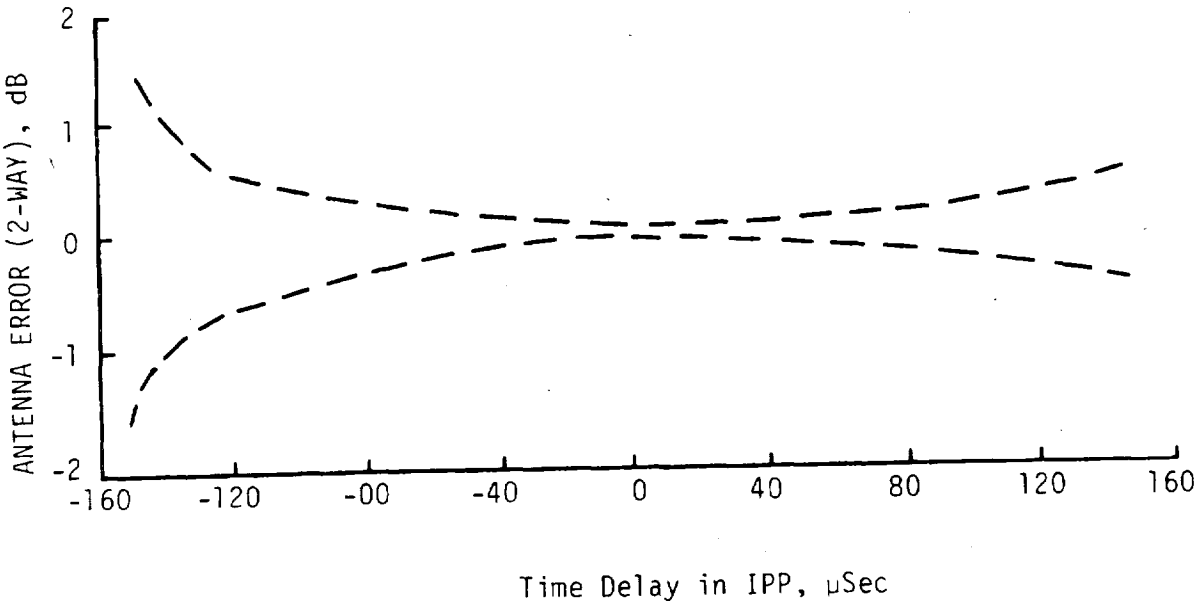

Figure C2. Two-Way Antenna Gain Variation

C.3 CALIBRATION CONSIDERATIONS OF THE SAR RECEIVER

Amplitude calibration requires knowledge of gain variation of the SAR receiver and also the level of the receiver thermal noise.

C.3.1 Effect of Mispositioning of the Record Window Upon Dynamic Range

The return signal is amplified in the SAR electronics receiver and amplitude modulated, using sensitivity time control (STC) circuitry, to coarsely compensate for the antenna gain pattern in range. However, the combination of the mispositioning of the record window and the STC greatly reduces the dynamic range of the input signal to the data link, as illustrated in Figure C3. For a uniform, extended target, the resulting envelope of the return power output from the receiver is expected to vary 3 dB to 4 dB over the swath for a centered record window (Figure C3a); and as much as 15 dB for a mispositioned record window (Figure C3b). Therefore, if the data link dynamic range is specified to be 20 dB, for example, then the backscatter coefficient of the extended target can vary 16 dB to 17 dB and still be within the data link dynamic range, if the record window is centered. If the record window is not centered, as shown in Figure C3b, the backscatter coefficient can vary only 5 dB and still fall within the data link dynamic range. Hence, the range of backscatter coefficient which the data link can accommodate is lowered by as much as 11 dB to 12 dB if the record window is mispositioned as in this example.

Even with maximum calibration efforts, the uncertainty of the combination of the receiver gain and the STC gain (allowing for some timing offset error in the STC waveform) is expected to be about $\pm$ 0.5 dB.

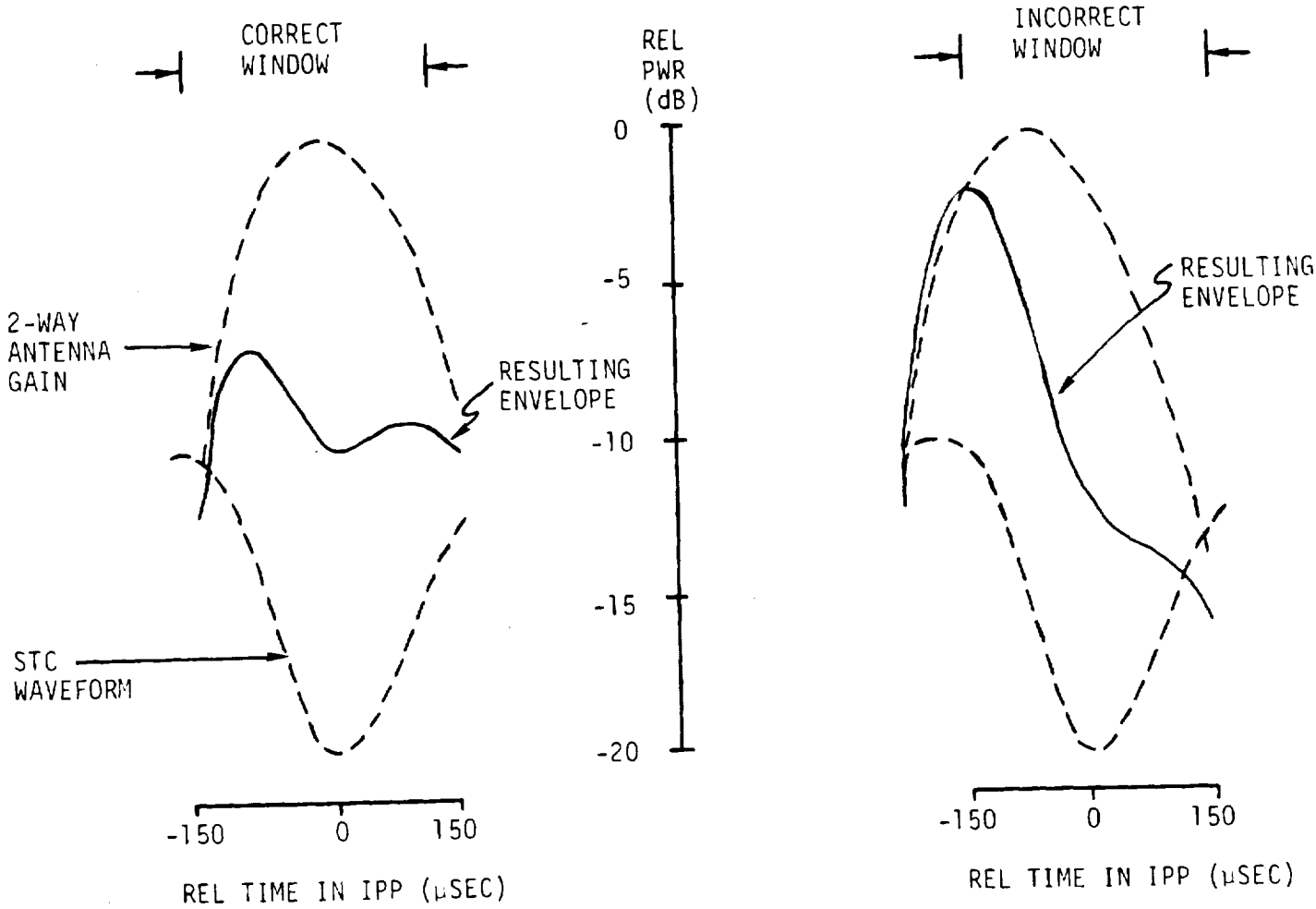

(a) Centered Record Window

(b) Off-Centered Record Window

Figure C3. Reduction of Dynamic Range Caused by Mispositioning of Record Window

C.3.2 Use of Receive-Only Noise in Calibration

Because of a pre-launch failure, the retriggered chirp calibration pulse was not able to be used for amplitude calibration. In the absence of this calibration pulse, the receiver thermal noise level may be used to perform a coarse amplitude calibration. Typically at the beginning of every SEASAT SAR pass before the SAR transmitter was enabled, a few seconds of data were recorded upon the high density data record (HDDR) while the SAR electronics receiver was enabled. This recorded, receiver noise is called the "receive-only" noise. This receive-only noise also contains noise contributions from the antenna, the data link, the SAR data formatter (SDF), and the HDDR recorder. The receiver thermal noise level was measured prior to launch, so that for the case of thermal noise dominating the receive-only noise, the use of this noise source may permit calibration of the SAR receive gain. Since the receiver noise is modulated by the "V-notched" STC waveform (Reference C1), as shown in Figure C3, the less attenuated portion (by the STC), at the beginning of the record window contains less of other system noises, and therefore is more reliable for receiver gain calibration.

There are several disadvntages in using the receive-only noise in calibration:

(1) To relate power of the received signal to power of the receive-only noise, the different spectral characteristics (as illustrated in Figure C4) must be taken into account,

(2) Many of the system noise contributors are not as well characterized as the receiver thermal noise,

(3) It is possible that returns from ground based radars may have interfered with the SAR receive-only noise to the point of complete saturation of the data link (Reference C3).

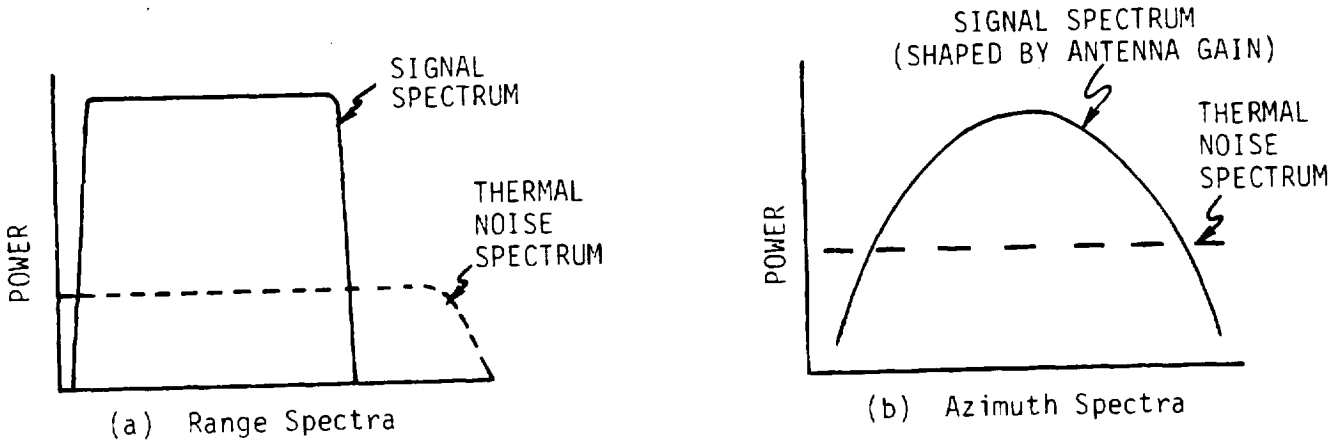

Figure C4. Spectral Characteristics of Signal and Receiver Thermal Noise

C.4 CALIBRATION CONSIDERATIONS OF THE SPACECRAFT PORTION OF THE DATA LINK

The spacecraft portion of the data link includes a modulator, an L-band to S-band translator, an S-band transmitter, and the data link Helix antenna as shown in Figure C5. The data link was designed to preserve the SAR return echo, the proper phasing information, and timing signals to present to the ground A/D converter, formatter, and recorder. The L-band return echo from the SAR receiver is RF summed to a pseudorandom noise (PN) sequence and to a pilot tone, translated to S-band, amplified, and radiated by the data link (D/L) antenna. The ground station portion of the data link includes the receiving antenna, an S-band preamplifier, multicoupler, down-converter, multi-function receiver (MFR), and SAR demodulator. The S-band signal transmitted from the spacecraft is received by the satellite tracking and data acquisition network (STDN) antenna, pre-amplified at S-band, down-converted to offset video in the SAR demodulator.

The gain of the data link was designed to be approximately unity. Actually, the data link gain depends upon the following (Reference C2):

(1) The transmitted pilot tone level variations as referenced to the input to the modulator/translator/transmitter,

(2) The S-band transmitter dependence upon temperature and average input signal level, and

(3) The attenuator setting in the 110 MHz line from the MFR to the demodulator.

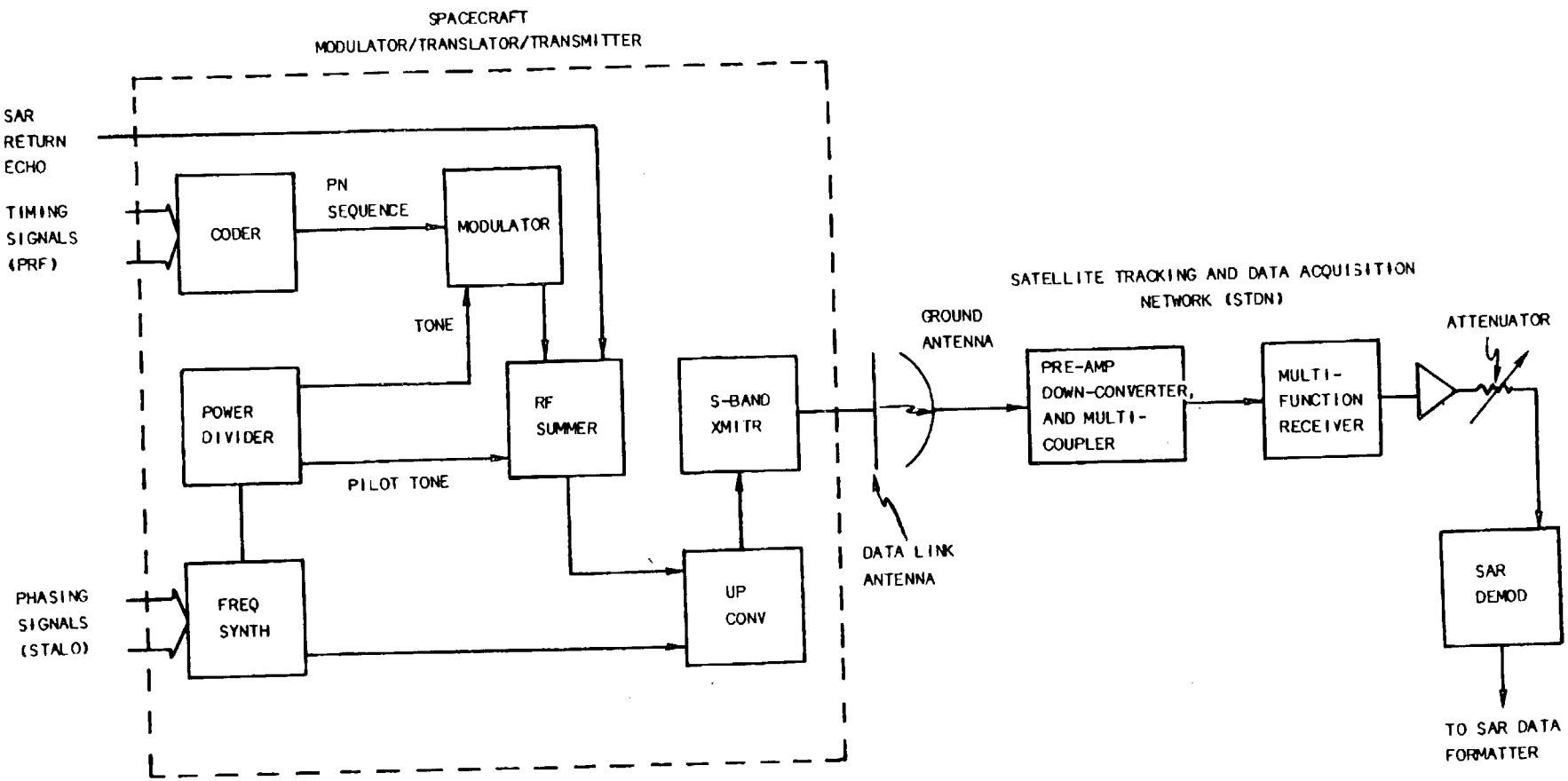

Figure C5. Data Link Path

The pilot tone level varies with temperature and the SAR receiver gain state because an inadvertent coherent L-band leakage tone from the SAR electronics combines with the data link pilot tone to produce a resultant pilot tone at a different level. The automatic gain control (AGC) circuitry in the station MFR then changes its gain correspondingly, which changes the data link gain from unity. For the typical operational range of S/C temperatures and the range of receiver gain settings actually used in flight, the data link gain is expected to vary -0.5 dB to +2.5 dB from unity gain. An additional effect is the small signal suppression of the pilot tone in the data link as the strength of the return echo increases and causes saturation in the data link. Also, the transmitter gain is temperature dependent, causing the pilot tone level to change with the varying temperature of the S-band transmitter. For a reasonable range of return echo strengths and observed S/C temperatures, the gain variation is expected to be from 0.1 dB to 1.8 dB. Soft saturation of the return echo may occur in the data link, for even if the receiver gain is correctly set, the record window misposition (shown in Figure C3) may cause returns of sufficient strength to be compressed considerably. The effect upon gain of the attenuator setting in the 110 MHz line is discussed in the next subsection.

C.5 CALIBRATION CONSIDERATIONS OF THE GROUND PORTION OF THE DATA LINK

The gain variations in the ground portion of the data link must also be taken into consideration for amplitude calibration. Figure C5 shows the ground portion of the data link as well as the spacecraft portion. The received signal at the ground station is known to contain aliased engineering telemetry data which is transmitted at a higher S-band frequency, but because of the filter characteristics of the data link and the sampling rate of the A/D converter, the engineering telemetry spectrum is folded onto the SAR echo spectrum. The strength of the aliased signals are much lower than the return echo; however, for certain configurations of the spacecraft and the ground station, the strength of the aliased signals may be on the order of, or even higher than, the other receive-only noises over portions of the record window. This could significantly affect calibration since the receive-only noise level is key in amplitude calibration; any variation in the noise level propagates as amplitude calibration uncertainty. The spectrum of the aliased engineering telemetry signal changes significantly with the telemetry mode (real-time telemetry, ranging, and playback). The various components of the composite engineering telemetry spectrum are represented in Figure C6a. Only a subset of these components are ever present in any particular operational mode. The spectrum of the data link reference signals and the receiver thermal noise, upon which the aliased engineering telemetry spectrum is folded, is represented in Figure C6b.

The 9m STDN antenna is intended to receive the data link signal when the data link transmitter is in the high power mode; the 26m STDN antenna, for the data link low power mode. The S/C was nominally configured in the data link high power mode; in the low power mode, the S-band transmitter gain was attenuated

6 dB, allowing a greater dynamic range for the data link for transmitting SAR echo data. However, in several cases, the 26m antenna was allocated to receive the high power mode signal. For sufficiently strong returns, the signals could approach the non-linear portion of the preamplifier-to-down-converter transfer.

The level of the pilot tone in the 110 MHz line from the MFR was intended to be constant at the demodulator input. However, because of the difference in the gain of individual MFR's at the stations, variations from the nominal setting were observed during several SEASAT passes to be as much as -3 dB to +1 dB. Also, an amplifier/attenuator combination in the 110 MHz line to compensate for the cabling loss between the MFR and the demodulator was observed on several occasions not to have been set correctly; this resulted in as much as 3 dB variation in the system gain.

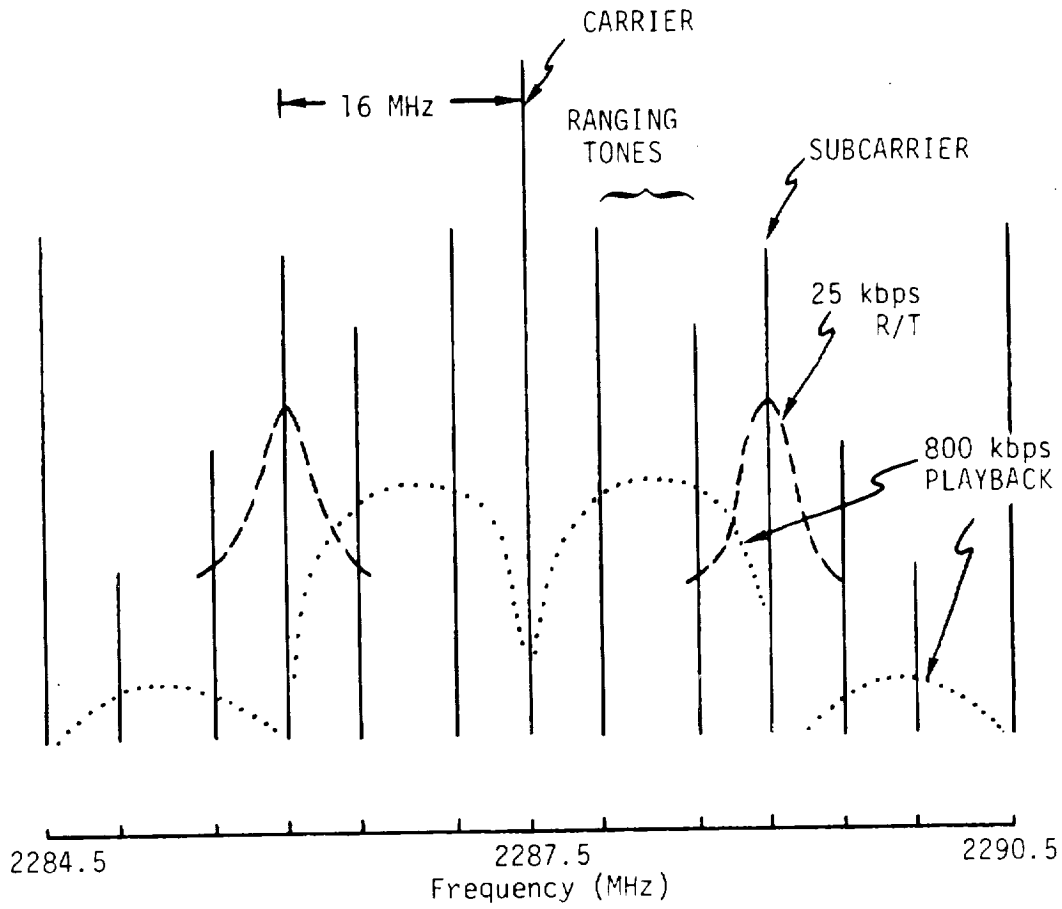

(a) Engineering Telemetry Spectra

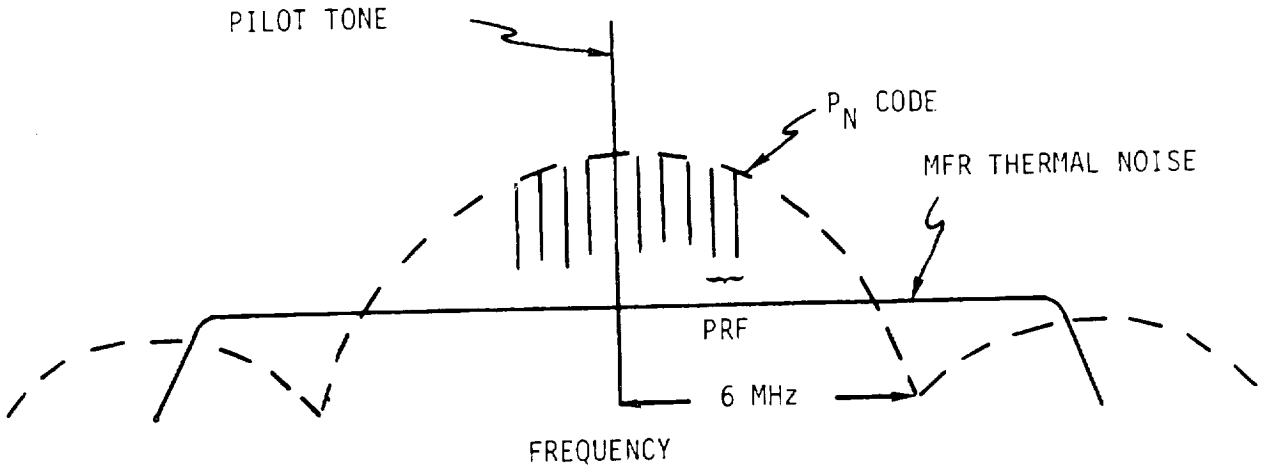

(b) Data Link Reference and Thermal Noise Spectra

Figure C6. Engineering Telemetry and Data Link Spectra

C.6 CALIBRATION CONSIDERATIONS OF THE GROUND STATION A/D CONVERTER, DATA FORMATTER, AND DATA RECORDER

Gain variations and non-linearities are introduced at the ground station as the data is A/D converted, formatted, and recorded. Figure C7 shows the data flow from the output of the demodulator to the HDDR tape. The offset video signal from the demodulator is presented to the SAR data formatter (SDF) to be amplified, A/D converted, formatted, and recorded onto the HDDR. The SDF front end gain state is selected to be high or low, depending upon whether the data link power mode is high or low, respectively. It is known that the ULA station had the incorrect SDF gain setting for the earlier passes, causing a 6 dB gain reduction, therefore, the actual SDF gain setting (hi/lo) should be verified for every pass. Also, measurements at the ground stations showed that the actual SDF front end gain varied from station to station by as much as 3 dB (Reference C3).

After the offset video signal is amplified in the front end of the SDF, it is sampled and converted from analog to digital, using 5-bit quantization. Quantization and saturation noise in the A/D converter is a function of the relative strength of the input signal to the saturation level of the A/D converter. Because of the gain variations in the system prior to the AD converter, there are uncertainties in determining the signal power for which saturation occurs. The A/D converted and formatted data is then recorded upon the HDDR, along with other housekeeping information.

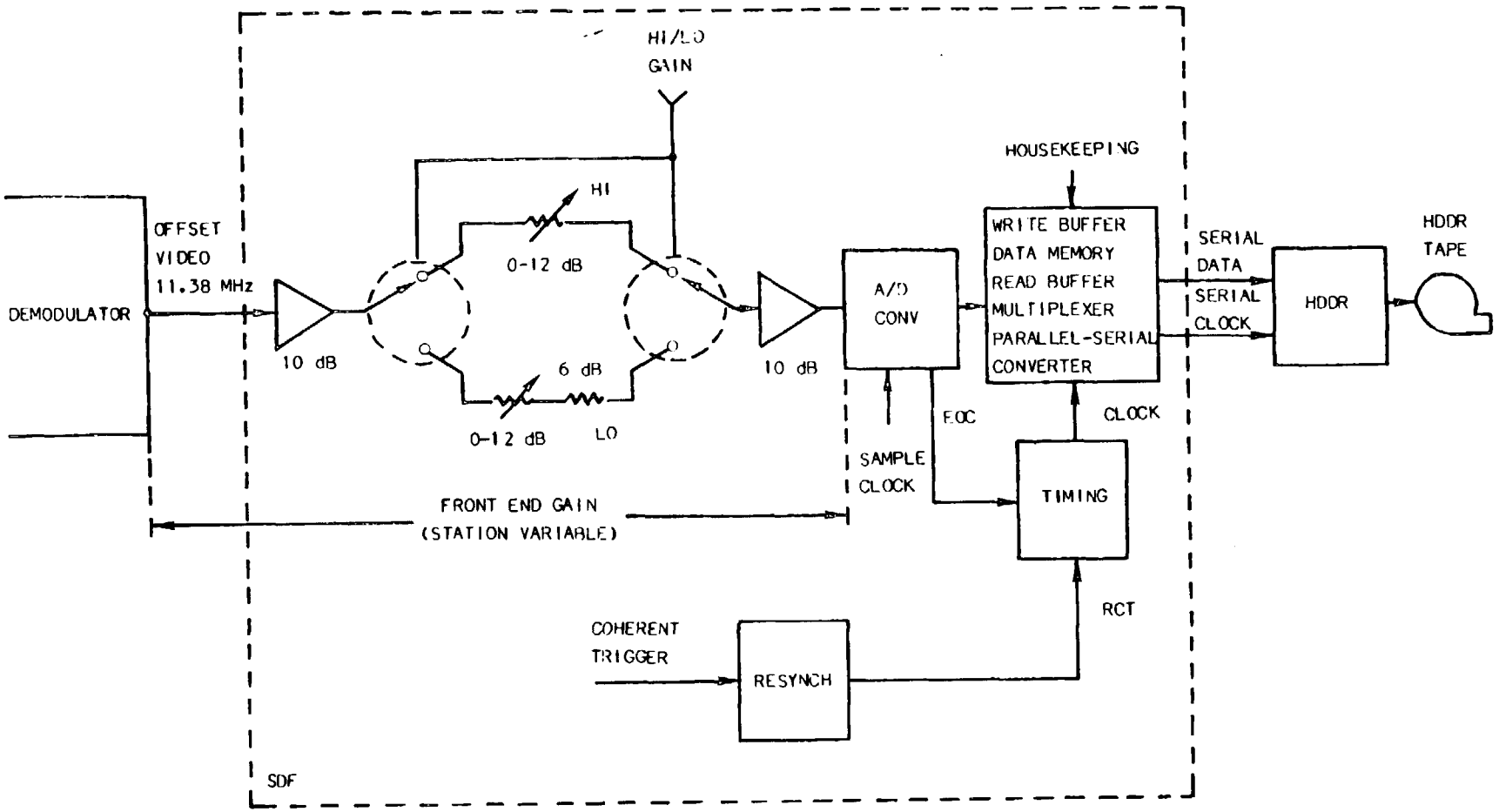

Figure C7. SAR Data Formatter (SDF)/High Density Data Recorder (HDDR)

C.7 CALIBRATION CONSIDERATIONS OF THE DATA PROCESSING SUBSYSTEM

Considerations of the radiometric calibration of the SEASAT SAR system have been confined to those elements of the system prior to, and including, the recording of the SAR data upon the HDDR tapes. As shown in Figure C1, portions of the data upon the HDDR tape are played back over an optical fiber link to the digital processor. Further study is to be given to the effect upon amplitude calibration caused by digital processing, such as would occur in range and azimuth correlation.

C.8 SUMMARY OF RADIOMETRIC CALILBRATION CONSIDERATIONS

In this section, consideration has been given to those elements in the SEASAT SAR system, up to the HDDR recording, which affect the amplitude calibration of the SAR data. The amplitude calibration is affected by (1) System gain variations, and (2) system non-linearities, such as gain compression and saturation. Use of the "receive-only" noise (in the absence of any other calibration signal), as recorded at the beginning of the pass, allows one to compensate for gain variations which occur after the SAR electronics receiver. For example, if a system gain variation is caused by an incorrect setting at the ground station receiver, the receive-only noise level will reflect that same gain variation, the degree to which the gain variation may be corrected corresponds to the degree to which the receive-only noise level can be characterized (Reference C4). This need to characterize the receive-only noise requires one to pay special attention to all system noise contributions which are sufficiently strong to appreciably alter the receive-only noise level.

It is expected that the amplitude of the uncalibrated data will be known to within no better than $\pm$ 9 dB; however, with proper calibration procedures, using available temperture data, S/C attitude data, pre-launch measurements, the engineering data recorded upon the sensor data records, and configuration data recorded in various logs, it is expected that the amplitude of the data can be calibrated to within $\pm$ 1.5 dB, up to the HDDR. This assumes that no signficant non-linearities are introduced and that the signal-to-noise ratio of the return signal is sufficiently high. Also, only SAR system controllable error sources have been considered; sources such as atmospheric, ionospheric, and Faraday rotation effects, and speckle have not been considered in this report.

REFERENCES

C1. "Cochannel Intereference Analysis Between Spaceborne and Terrestial Radars," John Nicholas, Jr., IEEE Transactions on Aerospace and Electronics, Vol. AES-14, No. 5, September 1978.

C2. "Effect of SEASAT-A SAR Data Link Noise at Low Elevation Angles," B. Huneycutt, JPL IOM 3395-79-034, 16 February 1979. (JPL internal document.)

C3. "Results of SEASAT-A SAR Station Observation at STDN Sites GDS, ULA, and MIL," B. Huneycutt, JPL IOM 3394-78-114, 25 September 1978. (JPL internal document.)

C4. "SEASAT-A SAR Receive-Only Noise Temperature," B. Huneycutt, JPL IOM 334.5-70, 13 April 1979. (JPL internal document.)